Long-wavelength radio observation of S5 0836+710 with the Low-Frequency Array (LOFAR)

Master Thesis
Julius-Maximilians-Universität Würzburg

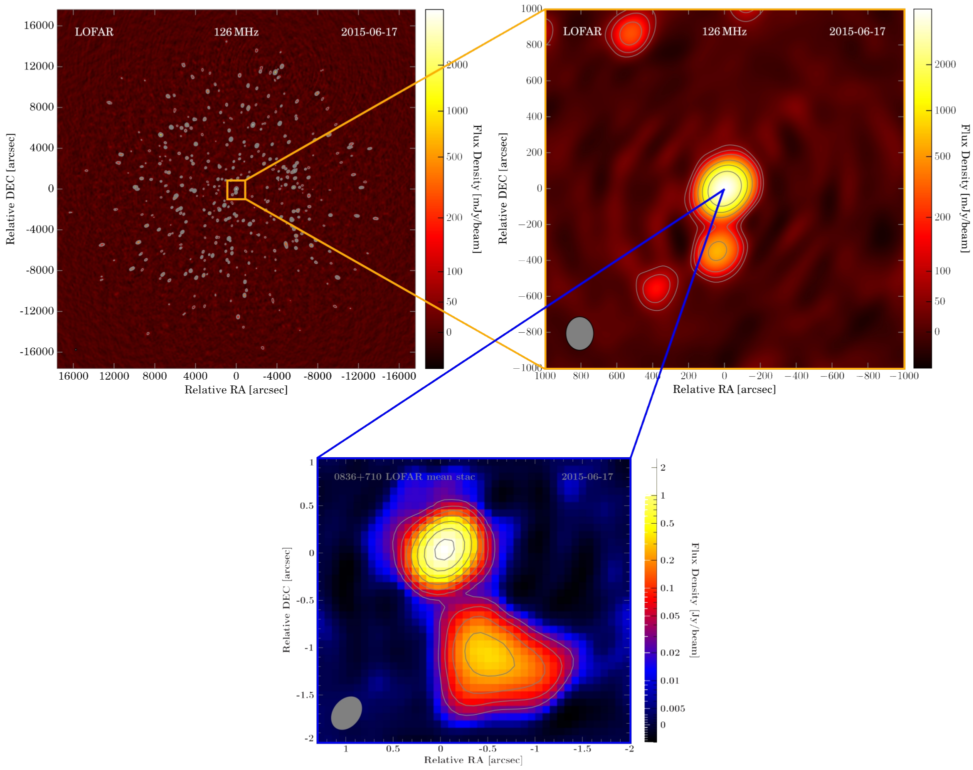

A thesis submitted in fulfilment of the requirements for the degree of Master of Science by
Alexander Kappes

Würzburg 2017

Zusammenfassung

Bis heute betrifft eine grundlegende Fragestellung in der Astronomie die hellsten Objekte im Universum, die **A**ctive **G**alactic **N**uclei (AGN). Viele Indikatoren weisen darauf hin, dass sich die verschiedenen Klassen von AGN in einem Modell vereinen ließen. Darin entsprechen die radio-lauten FR I und FR II Objekte den rotierten Gegenstücken den **BL Lac**erta (BL Lac) und respektiv **F**lat **S**pectrum **R**adio **Q**uasar (FSRQ) Objekten. Um dieses Modell zu durch Beobachtungen zu bestätigen, benötigt man eine große Gesamtheit an Testobjekten, welche man auf diverse Parameter untersuchen kann, wie der Helligkeit, dem Abstand, der Größe, dem Inklinationswinkel, sowie der räumlich aufgelösten Helligkeitsverteilung in verschiedenen Wellenlängen. Mit zunehmender Entfernung zum Objekt wird dies jedoch schwieriger, da auch das Auflösungsvermögen mit zunehmender Wellenlänge abnimmt. In dieser Hinsicht bietet das **LO**w-**F**requency **AR**ray (LOFAR) Teleskop durch die Kombination von einer hohen Auflösung (etwa $0.5''$), einer hohen Empfindlichkeit (bis etwa $0.2\,\mathrm{mJy}$) und die Beobachtung bei Radio Nieder-Frequenzen ($90-240\,\mathrm{MHz}$)zuvor nie dagewesene Möglichkeiten. Dies ermöglicht Studien auch über weit entfernte AGN in einem weiten Wellenlängenbereich, wodurch ein weiterer Evolutionsabschnitt abgedeckt werden kann. Dies eröffnet eine neue Option, um die einleitende Fragestellung zu untersuchen.
Die technische Umsetzung dessen erweist sich allerdings als sehr herausfordernd. Die Kalibration solcher **V**ery **L**ong **B**aseline **I**nterferometry (VLBI) Daten ist deutlich komplizierter als jene im GHz Bereich. Aus diesem Grund kostete es bisher viel Zeit und einen großen Aufwand, um Beobachtungen des LOFAR Teleskops auszuwerten. Diese Arbeit zeigt, dass eine Pipeline entwickelt werden konnte, welche alle notwendigen Korrekturen und Kalibrationen in einer parallelisierten Form durchführt. In Teilen ist diese ähnlich zur einer bereits veröffentlichten **L**ow **B**and **A**ntenna (LBA) Pipeline. Dies erlaubt die Daten bis zum Schritt der Bilderzeugung vorzubereiten, wonach man mit einer bevorzugten Prozedur fortfahren kann. Dies erfolgt standardisiert und in kürzerer Zeit.
Die Leistungsfähigkeit der Pipeline ist in dieser Arbeit anhand des FSRQ Objektes *S5 0836+710*, mit einer Rotverschiebung von $z = 2.218$ demonstriert. Die Daten sind aus einer LOFAR **H**igh **B**and **A**ntenna (HBA) Beobachtung aus dem vierten Beobachtungs-Zyklus entnommen. Insbesondere verschafft dies wertvolle komplementäre Ergebnisse zu anderen Beobachtungen dieser Quelle. Der gemessene Fluss der unaufgelösten Kernregion beträgt (1.998 ± 0.090) Jy und zeigt bezüglich Daten aus dem C-Band des Karl G. Jansky **V**ery **L**arge **A**rray (VLA) Teleskops ein flaches Spektrum. Dies entspricht

einer relativistisch verstärkten Emissionsregion im Gegensatz zum steilen Spektrum der umschließenden weitläufig ausgedehnten Emissionsregion welche entsprechend isotrope Emission aufweist. Dies stützt nicht nur die Erwartung sondern bestätigt auch, dass LOFAR die Fähigkeit besitzt die Emissionsregionen von weit entfernten Blazaren zu differenzieren. Eine Komponente im Südwesten konnte in den Daten detektiert werden, welche auch von anderen Teleskopen wie dem **E**uropean **V**LBI **N**etwork (EVN)+**M**ulti-**E**lement **R**adio **L**inked **I**nterferometer **N**etwork (MERLIN) Teleskop Netzwerk gefunden wurde. Diese konnte im Rahmen dieser Arbeit ebenfalls analysiert werden. Sie besitzt einen Spektralindex von -0.97 ± 0.28 zwischen 126 MHz und 160 MHz. Dies deutet auf eine isotrope Emissionsregion hin. Die favorisierte Erklärung für die Entstehung dieser Region ist eine Schock-Front mit dem **I**nter **G**alactic **M**edium (IGM). Diese würde durch eine anwachsende **K**elvin-**H**elmholtz (KH) Instabilität im extragalaktischen Jet zu dessen Zerstörung der Kollimation führen.
Zu diesem Zeitpunkt können Beobachtung mit bestehenden oder zukünftig bestehenden HBA Stationen zu hochwertigen, hoch aufgelösten Aufnahmen verarbeitet werden. In Zukunft kann diese Prozedur auf eine größere Anzahl an Objekten angewendet werden, so dass aus diesem systematischen Ansatz und der resultierenden Statistik die einleitend geschilderte Fragestellung beantwortet werden kann.

Abstract

A major puzzle about **A**ctive **G**alactic **N**uclei (AGN), being amongst the brightest objects in the universe, still remains in astronomy to this date. There are a number of indications in favor of a unification of the different classes of AGN in the unification model. In this model, the radio loud FR I and FR II are rotated counterparts of the **BL Lac**erta (BL Lac) and **F**lat **S**pectrum **R**adio **Q**uasar (FSRQ) objects. Confirming this model observationally, a vast statistical sample of those objects is needed with different measured parameters, like luminosity, distance, size, inclination angle, as well as spatial resolved brightness distributions in different wavelengths. With an increasing distance to the object this becomes harder since the resolution capabilities decrease with the observed increasing wavelength. In this respect the **LO**w-**F**requency **AR**ray (LOFAR) telescope offers unprecedented possibilities with the combination of high-resolution (about $0.5''$), sensitivity (down to about $0.2\,\mathrm{mJy}$) and operating at low radio frequencies ($90 - 240\,\mathrm{MHz}$). This enables the study of more distant AGN and therefore covers their evolution over a wider range. This helps significantly in studying the introduced topic.
Admittedly, the technical realization is very challenging. The calibration of these kind of **V**ery **L**ong **B**aseline **I**nterferometry (VLBI) data is also much more complicated than those in the GHz regime. This is why it took a lot of time and effort to analyze observations with the full station network up until now. This thesis shows that a pipeline could be elaborated, that performs all necessary correction and calibration steps in a fully parallelized fashion. It is partially familiar to a pipeline for **L**ow **B**and **A**ntenna (LBA) data. This allows for preparing the data, up to the point of creating images in a favored standardized way and in less time.
The performance of the pipeline is shown in this thesis on the FSRQ *S5 0836+710* with a redshift of $z = 2.218$ taken from the LOFAR **H**igh **B**and **A**ntenna (HBA) observation cycle 4. This especially provides important complementary results of other observations. The measured flux of the unresolved core region with $(1.998 \pm 0.090)\,\mathrm{Jy}$ shows a flat-spectrum with respect to Karl G. Jansky **V**ery **L**arge **A**rray (VLA) data in the C-band as expected for a beamed emission region. The extended emission around it in contrast appears with a steep-spectrum representing unbeamed emission. This not only confirms the expectation, but also proves the capability of separating core flux from the extended emission regions for distant blazars. In the south west a component could be detected which shows unusual properties and was also detected by other telescopes like the **E**uropean **V**LBI **N**etwork (EVN)+**M**ulti-**E**lement **R**adio **L**inked **I**nterferometer

Network (MERLIN). A spectral index of -0.97 ± 0.28 could be measured between 126 MHz and 160 MHz showing an unbeamed emission region. The favored scenario for this component is a resulting shock structure with the **I**nter **G**alactic **M**edium (IGM) due to a growing **K**elvin-**H**elmholtz (KH) instability leading to the jet's destruction.
At this stage, the pipeline can be used to process more data of a bigger sample to achieve high-quality high-resolution data within LOFAR HBA observations, including all current and future stations. This will address the initial topic and helps in answering it with a systematic and significant statistic basis.

Contents

Zusammenfassung i

Abstract iii

1. Introduction 1

2. Active Galactic Nuclei (AGN) 3
- 2.1. The AGN zoo . . . 3
- 2.2. Unification model . . . 6
- 2.3. Blazar and radio galaxy connection . . . 7
- 2.4. *S5 0836+710* . . . 9

3. Radio observations 13
- 3.1. Radio single dish telescopes . . . 13
- 3.2. Radio interferometry . . . 17
- 3.3. The Low-Frequency Array (LOFAR) . . . 21
- 3.4. Interferometry with LOFAR . . . 26
- 3.5. Hybrid Imaging . . . 28

4. Observation and data processing (processing pipeline) 29
- 4.1. Radio observatory processing . . . 29
- 4.2. Data calibration . . . 30
- 4.3. Absolute flux calibration on high resolution images . . . 33

5. Results of the pipeline's application on *S5 0836+710* 35
- 5.1. Images . . . 36
- 5.2. Flux measurements . . . 40
- 5.3. Spectral properties . . . 49
- 5.4. Parameter analysis . . . 50
- 5.5. Discussion . . . 52

6. Summary and Outlook 55

Appendices 57

A. Final high resolution images of *S5 0836+710* 59

B. Spectral maps of *S5 0836+710* 63

C. Pipeline scripts 67

Bibliography 83

List of Figures 87

List of Tables 95

Danksagung 101

1. Introduction

Observational astronomy, follows the overall strategy in increasing resolution, sensitivity and cover more frequency bands since ever. Especially in the last decades, radio astronomy could improve sensitivity and resolution by many orders. This happened especially in the GHz regime like the **V**ery **L**ong **B**aseline **A**rray; Kellermann & Thompson 1985 (VLBA), Karl G. Jansky **V**ery **L**arge **A**rray; Thompson et al. 1980 (VLA), **T**racking **A**ctive Galactic **N**uclei with **A**ustral **M**illiarcsecond **I**nterferometry (TANAMI). Lower frequencies in the radio band show significantly stronger interaction with the ionosphere and are more likely to be affected by **R**adio **F**requency **I**nterference (RFI). This means a complex calibration procedure combined with high computational demands. **LO**w-**F**requency **AR**ray; van Haarlem et al. 2013 (LOFAR) is the first telescope in this respect, managing to provide these needs. Up to date the calibration for observations, where all stations are participating is still very challenging and no dedicated pipeline is officially offered by the radio observatory to fully obtain high resolution images. The technical properties allow to cover a very wide field of key science topics, like the study of epoch of re-ionization, transients and pulsars, high energy cosmic rays, surveys and the distant universe, cosmic magnetism, solar physics and space weather. **A**ctive **G**alactic **N**uclei (AGN) as observation targets are especially interesting for LOFAR because they show high intrinsic luminosities over very wide regimes of the **E**lectro **M**agnetic (EM) spectrum. In this context notably blazars that appear as the brightest class of AGN due to their boosted particles along the line of sight towards us resulting in a beamed emission. Regarding Urry & Padovani (1995), the unification model predicts blazars to be the rotated radio galaxies FR I and FR II to as BL Lacertae and **F**lat **S**pectrum **R**adio **Q**uasar (FSRQ) respectively. To investigate this, it is necessary to observe different stages of AGN evolution, which also means very distant ones with high redshifts. The steep spectrum of extended emission regions favor observations in low radio frequencies. With a sufficient resolution capability, LOFAR is an excellent instrument to separate the emission originating from the core region, dominated by the extra galactic jet, from the extended region. This is adressed in multiple proposals (PI: Trüstedt) in the 3*rd*, 4*th* and 5*th* observation cycle for LOFAR **H**igh **B**and **A**ntenna (HBA) observations on a large sample also monitored by **M**onitoring **O**f **J**ets in **A**ctive galactic nuclei with **V**LBA **E**xperiments; Lister & Homan 2005 (MOJAVE) in the GHz regime. This thesis studies *S5 0836+710* which is one target of those in detail. Also spotlighting the processing pipeline to obtain high resolution data from LOFAR HBA observations.

2. Active Galactic Nuclei (AGN)

AGN are among the most energetic particle accelerators in the universe. Active galaxies feature a region in the center, in the size of our solar system, radiating a power that dominates the host galaxy. They emit a flat spectrum radiation in the entire EM spectrum. Contrary to non-active galaxies which in a first order approximation feature a black body spectrum around the optical regime due to the superposition of the black body radiation from individual stars. AGN are also the most probable candidates for neutrino and especially high energy neutrino emission, see Kadler et al. (2016). The engine of these processes is a **S**uper **M**assive **B**lack **H**ole (SMBH) in the inner center of active galaxies. These are surrounded by an accretion disk with hot material circulating with up to 86,000 $^{\mathrm{km}}/_{\mathrm{s}}$. Around the accretion disk there is also colder gas and a surrounding torus shielding a wide range of radiation. The luminosity of AGN typically ranges between $10^{42} \leq \mathrm{L}\,/\mathrm{erg\,s^{-1}} \leq 10^{47}$ which can be reached by accreting mass on the SMBH (Shakura & Sunyaev 1973). Since the mass of the SMBH correlates to the luminosity due to the accretion process, this indicates black hole masses from $10^7 \leq {}^{\mathrm{M}}/_{\mathrm{M}_\odot} \leq 10^{10}$ (Vestergaard & Peterson 2006 and Peterson et al. 2004). The following information is based on the textbooks of Schneider (2008) and Krolik (1999)

2.1. The AGN zoo

Different criteria to categorize AGN were introduced in the past while some could suffice new observations and analysis. The simplest is to differentiate between radio loud and radio quiet AGN (introduced by Kellermann & Pauliny-Toth 1969). These are defined by the radio loudness, which can be computed as the ratio between the flux in the radio and optical regime:

$$R = \frac{F_R}{F_O} = \begin{cases} \gtrsim 10 & \rightarrow \text{radio loud} \\ 0.1 < R < 1 & \rightarrow \text{radio quiet} \end{cases} . \tag{2.1.1}$$

Furthermore, radiation is differentiated between thermal and non-thermal, like synchrotron radiation, processes. The defined radio loudness can also indicate which processes are mainly contributing to the total flux, as synchrotron emission can be detected in the radio regime.

Radio galaxies

Eventually the processes in radio loud AGN lead to a formation of an extended structure, a so called jet. Two favored mechanisms potentially explaining the formation are the extraction of electromagnetic energy from rotation energy of the SMBH, resulting in collimated jets after Blandford & Znajek (1977) or present particle winds from the accretion disc resulting in broad jets, after Blandford & Payne (1982). The formed jet is accelerated in either scenario from the SMBH in both sides perpendicular to the accretion disk. Depending on the jet power the beam of plasma carried out of the host galaxy interacts with the inter galactic medium while losing energy. Here another two classes can be introduced when looking edge-on to the accretion disc. Fanaroff & Riley (1974) introduce the less luminous FR-I and higher luminous FR-II AGN (see Figure 2.1) also known as the Fanaroff-Riley morphology sub-classes of radio galaxies.

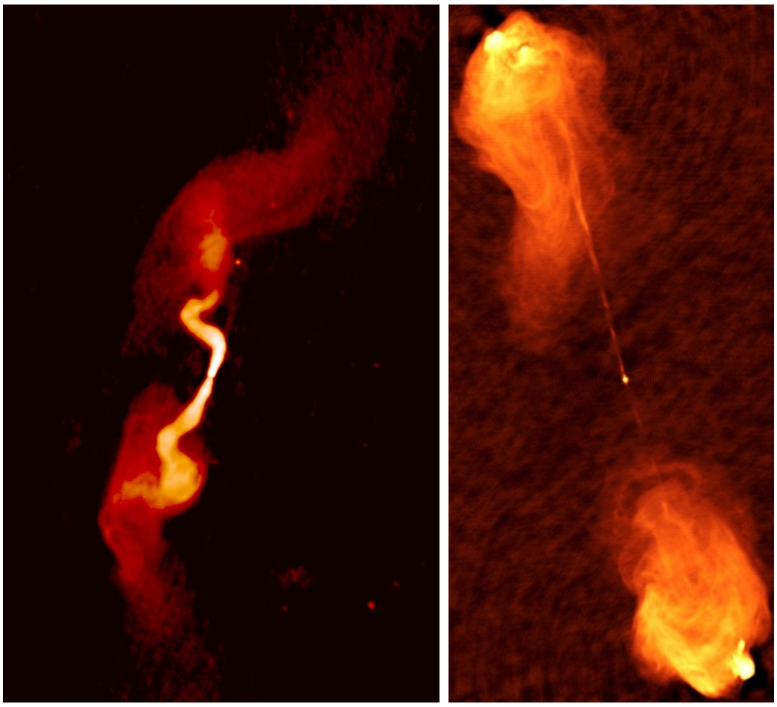

(a) (b)

Figure 2.1.: VLA observations of the FR-I radio galaxy 3C31 (a) at 1.4 GHz and the FR-II radio galaxy CygnusA (b) at 6 GHz. While 3C31 shows the typical bright jet terminating into plumes, CygnusA powers the highly collimated jet by the bright core in the center terminating into bright hot spots. These are feeding the surrounding lobes. Image from Lara et al. (1997) and Perley et al. (1984) with image courtesy of NRAO/AUI.

The FR-I AGN show a broad and bright jet terminating into diffusive plumes. The jets are considered to interact with their surrounding quite early after forming and therefore losing continuously significant amounts of their initial energy while streaming into the plumes. The common FR-I luminosities are typically constrained to have emission in the extended regions below $\log(L^{ext}_{178MHz}[\mathrm{W\ Hz}^{-1}]) \lesssim 24.5$.
In contrast the FR-II AGN have rather narrow jets that don't dominate the total luminosity of the object as FR-I do. They seem to barely interact for a very long time with the surrounding medium until they eventually terminate in a reverse jet-shock, called hot spot and feed the surrounding lobe with energetic plasma. In general these are constrained by their extended emission to be above $\log(L^{ext}_{178MHz}[\mathrm{W\ Hz}^{-1}]) \gtrsim 26$ (Kharb et al. 2010; Cooper et al. 2007). However it is to be said that there is no clear transition in morphology and there also exist intermediate AGN.
Radio loud AGN with low inclination only are referred to as blazars. They typically feature a compact radio morphology and feature a flat radio spectrum which origins from beamed synchrotron emission. If they are rather luminous and show broad and narrow spectral lines, they are called FSRQ. When the object has lower luminosities and no spectral lines while featuring a compact morphology it is categorized as a **BL Lac**erta (BL Lac) object. Measuring the distance of those via the redshift is not possible due to the lack of spectral lines, therefore that information is often not available.
Looking at the spectra of radio galaxies one can establish further classifications. Some objects feature only narrow spectral lines in the spectra. These can have morphologies of FR-I or FR-II and are referred as **N**arrow **L**ine **R**adio **G**alaxies (NLRG). When they also emit broad spectral lines and don't have a compact but FR-I or FR-II morphology, they are called **B**road **L**ine **R**adio **G**alaxies (BLRG).
Apart from the radio galaxies there are also sub-classes for radio quiet AGN. These are not introduced in detail, since the theses focuses on radio galaxies.
Radio quiet AGN show no radio morphology or jet and are therefore categorized by the luminosity and spectrum. If they show high luminosities they are called **Q**uasi **S**tellar **O**bject (QSO), regardless of the line-widths in the spectrum.
While having low luminosities objects are referred as Seyfert 2 when only showing a narrow line spectrum and Seyfert 1 when narrow and broad lines can be found in the spectrum.
The following table is summarizing all the information given above:

Table 2.1.: AGN classes with classification properties; Credit: Matthias Kadler with minor modifications.

Type	Radio Loudness	Emission Lines	Luminosity	Jet	Radio Morphology
Seyfert 1	quiet	broad+narrow	low	none	none
Seyfert 2	quiet	narrow	low	none	none
QSO	quiet	broad+narrow	high	none	none
QSO	quiet	narrow	high	none	none
BLRG	loud	broad+narrow	low	yes	FR-I
BLRG	loud	broad+narrow	high	yes	FR-II
NLRG	loud	narrow	low	yes	FR-I
NLRG	loud	narrow	high	yes	FR-II
BL Lac	loud	none	low	yes	compact or rotated FR-I
FSRQ	loud	broad+narrow	high	yes	compact or rotated FR-II

According to the unification scheme which is discussed in the following the blazars are considered to be rotated radio galaxies with FR-I or FR-II morphology respectively.

2.2. Unification model

AGN as shown before, have various properties with respect to the morphology, energy and spectrum. According to the unification scheme, all their phenomena can be explained by the same type of object containing a SMBH with an accretion disc surrounded by a dusty torus potentially forming a radio jet. The only parameters are the inclination angle and the luminosity. This theory is explained in the following paragraph based on Antonucci & Barvainis (1990), Antonucci (1993) and Urry & Padovani (1995).

As described above, the engine powering the emission processes is a SMBH in the center of the galaxy forming an accretion disc with infalling matter that is reaching very high speeds and therefore forming substantial thermal emission (see figure 2.2). The high speeds create broad line widths in the emission spectrum. This region is therefore called **B**road **L**ine **R**egion (BLR) and can only be seen for inclination angles where the opaque torus does not obscure the accretion disk due to free-free absorption (Kameno et al. 2003). Further outside colder gas can be found, still emitting thermal radiation with

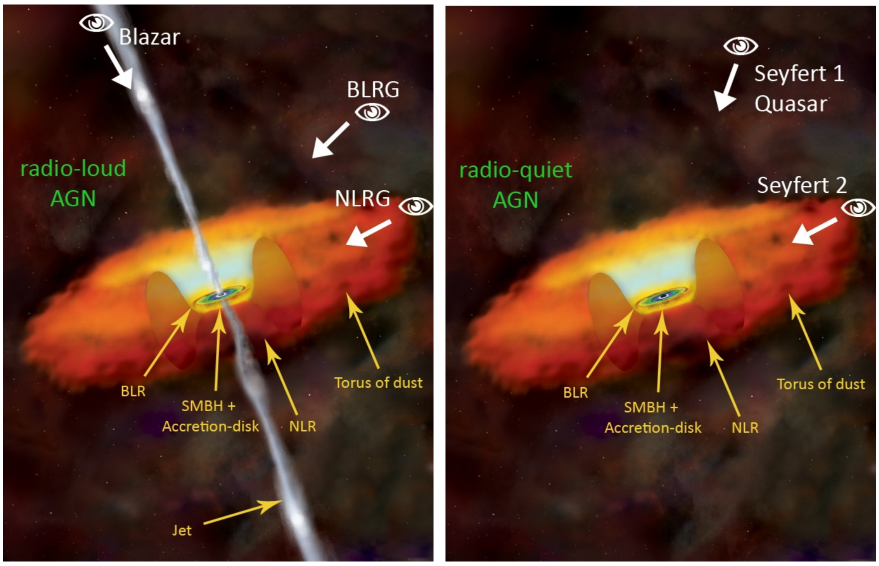

Figure 2.2.: Schematic summary of the unification model based on Urry & Padovani (1995). The SMBH in the center is surrounded by the accretion disc and the dust torus. On the left the radio loud AGN are illustrated, likewise on the right the radio quiet AGN are illustrated. Different angles for the line of sight result in their respective object class as indicated with the arrows. Credit: NASA/CXC/M.Weiss; edited by Jonas Trüstedt.

lower velocities. This region contributes narrow emission lines in the spectrum and is therefore called **N**arrow **L**ine **R**egion (NLR). Assuming a radio loud galaxy, eventually a radio jet perpendicular to the accretion disc is formed, transporting plasma in a highly collimated beam with relativistic velocities out of the host galaxy. For a very small inclination angle, in the case of a radio loud galaxy, we would look into the jet while depending on the luminosity it would be a BL Lac or FSRQ. Rotating this very same galaxy a bit with clear vision into the BLR and NLRR we can observe a BLRG. In the case of a radio quiet AGN this would translate to a Seyfert 1 or QSO. Further increasing the inclination angle, the torus covers the BLR and only the contribution of the further out positioned NLR can be detected. Accordingly this is the NLRG for a radio loud AGN and a Seyfert 2 or QSO when talking about radio quiet AGN.

2.3. Blazar and radio galaxy connection

As previously discussed, the luminosity of the extended emission and the morphology subdivide radio galaxies into two classes, and according to the unification scheme of AGN, BL Lac objects are associated with the beamed and rotated counterparts of FR I galaxies. FSRQ should be the beamed and rotated counterpart of FR II galaxies. At low radio frequencies the emission of BL Lac and FSRQ objects are dominated by the unbeamed steep-spectrum synchrotron emission from the regions of their extended jets and lobes, which are optically thin. In the high radio frequencies the dominating emission originates from the flat-spectrum core as seen in many **V**ery **L**ong **B**aseline **I**nterferometry; Readhead & Wilkinson 1978 (VLBI) observations in the GHz regime. MOJAVE is the largest long-term monitoring program for a selected sample of 181 radio-selected AGN sample with a lower flux limit of at least 1.5 Jy (Lister et al. 2011,Lister et al. 2013). For the first time LOFAR offers a sufficient angular resolution and sensitivity in the low frequency regime to measure the unbeamed emission component of blazars. An observation proposal to test this prediction (PI:Trüstedt) in the $5th$ observation cycle of LOFAR, as a continuation of previous proposals in the $3rd$ and $4th$ cycle, aims to test the large MOJAVE sample. This challenges the prediction that any steep-spectrum lobe emission dominates over the flat-spectrum component for blazars. This has previously already been done by Massaro et al. (2013) between 74 MHz and 1.4 GHz with the VLA but did not produce significant results, most likely due to the resolution, which is not sufficient enough.

In order to perform these studies the intrinsic luminosity is important to know. Measuring the flux, the following equation according to Condon (1988) has to be applied to calculate the luminosity:

$$L_{\mathrm{c,ext}} = \frac{F_{\mathrm{c,ext}\ 4\pi(c\ z)^2}}{H_0^2(1+z)^{1-\alpha}} \ . \tag{2.3.1}$$

It can be used either for the core luminosity (c) or the extended luminosity (ext) which is the source luminosity subtracted with the core luminosity. z is the redshift, $F_{\mathrm{c,ext}}$ is the radio flux density of the core or the extended structure respectively, measured in $\mathrm{W/Hz\ m^2}$. α is the spectral index - for flat spectrum radio sources it is 0. The Hubble constant is given as $H_0 = 67.8\,\mathrm{km/s\cdot Mpc}$, $\Omega_\mathrm{m} = 0.308$ and $\Omega_\Lambda = 0.692$; consistent with Ade et al. (2016). Hence the luminosity is given in $\mathrm{W/Hz}$.

2.4. *S5 0836+710*

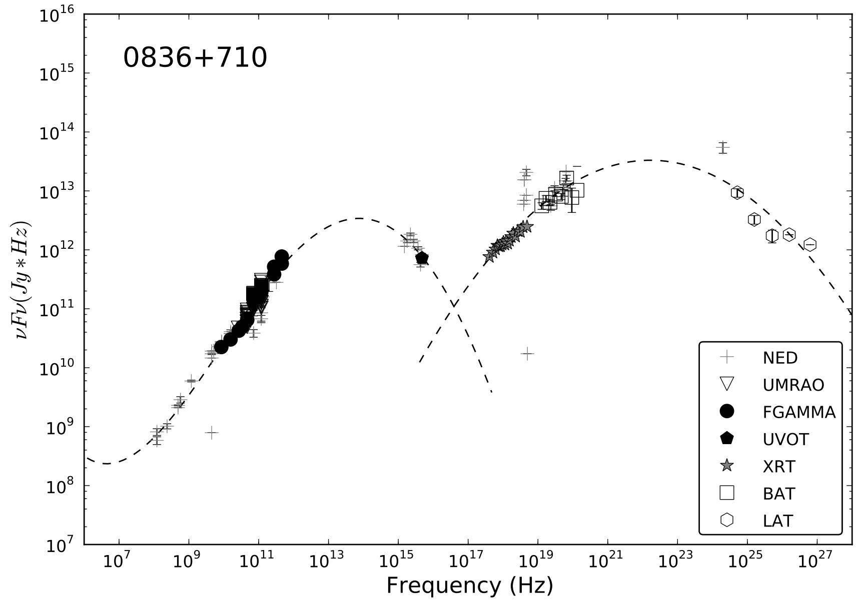

Figure 2.3.: The broad band SED of *S5 0836+710*. Credit: Chang (2010).

In this thesis, I present the analysis of a first target source observed as part of the LOFAR-MOJAVE program described in the previous section. It is the AGN *S5 0836+710* (Kuehr et al. 1981; also known as *4C 71.07*; Caswell & Crowther 1969 or *3FGL J0841.4+7053*; Acero et al. 2015). Within the project it is the target with the highest redshift ($z = 2.218$; Stickel & Kuehr 1993) out of 16 others. It is part of a proposal with a sample of BL Lac objects and FSRQs (PI: Trüstedt). With a moderately high expected flat-spectrum core luminosity of about 2.2 Jy (Cara & Lister 2008) it also offers a high SNR (**S**ignal-to-**N**oise **R**atio).
S5 0836+710, is classified as a low spectral peaked ($< 10^{14}$ Hz) quasar with fractional linear optical polarization consistently below 3% Lister et al. (2009). Which means a peaked spectrum in low frequencies, providing a higher flux compared to other spectral bands. This offers an optimal target for LOFAR that is operating in this regime. The broadband **S**pectral **E**nergy **D**istribution (SED) shown in Figure 2.3 elaborated from Chang (2010) shows two humps with peak frequencies of $\nu_{\mathrm{peak}}^{\mathrm{sync}} \sim 10^{14}$ Hz for the synchrotron emission and $\nu_{\mathrm{peak}}^{\mathrm{IC}} \sim 10^{22}$ Hz for the **I**nverse **C**ompton (IC) emission. Previous studies by Sambruna et al. (2007) show a IC hump peaked at $\nu_{\mathrm{peak}}^{\mathrm{IC}} \sim 10^{20}$ Hz whereas the synchrotron hump is not clearly shown. Otterbein et al. (1998) showed broad-band (gamma to radio) variability between 1992 and 1993 in that source. Further space VLBI

observations from Lobanov (1998) modeling the observation with relativistic outflows (Lorentz factor $\gamma_j \approx 11$), a Mach number of $M_j \approx 6$ and an opening half-angle of $\Phi_j \approx 1°$.

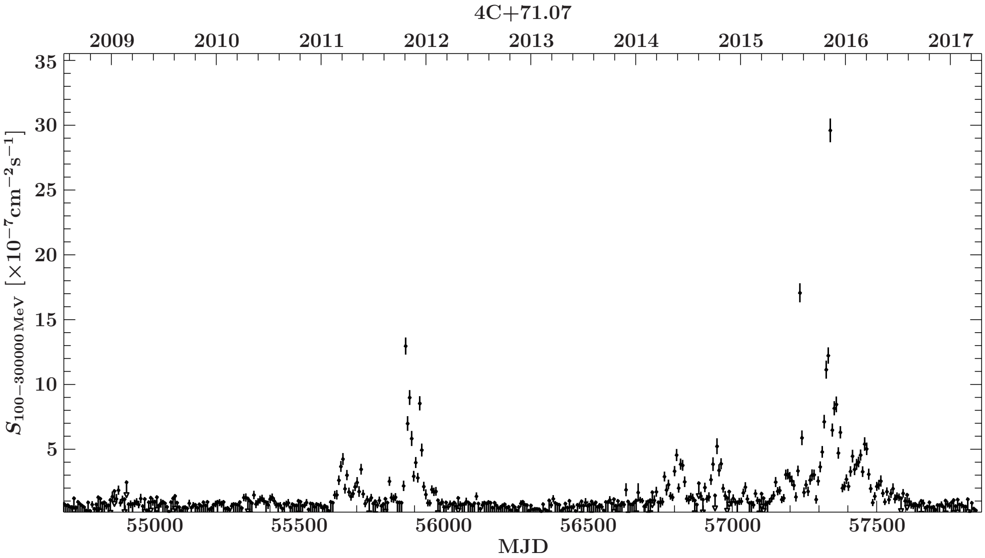

Figure 2.4.: *Fermi*/LAT γ-ray light curve of *S5 0836+710* in the energy range between 100 MeV to 300 GeV with a weekly binning between August 2008 and April 2017. Multiple outburst periods on the order of weeks to months can be seen. Credit: M. Kreter.

This source showed even repeated states of activity in multiple wavelengths as the long term multi-wavelength study by Akyuz et al. (2013) has shown. Inspecting the long-term γ-ray light curve observed by *Fermi*/LAT (Team et al. 1999) in Figure 2.4, one can see states of very high activity, also called *flares*. The spectrum in the γ-regime shows by far the highest relative flux increase. This very fact is the reason for very good multi-wavelength studies on this source (Akyuz et al. 2012).
In radio VLBI measurements it is monitored by the VLBA in the MOJAVE sample[1]. With a measured apparent jet speed of $21.10 \pm 0.77\,\mathrm{c}$ based on seven moving features (Lister et al. 2013) it shows high apparent superluminal motion. The high resolution images show a helical structure of the jet studied in detail by Perucho et al. (2012a) (e.g. Figure 2.6). After about $0.2''$ the jet seemingly disappears. After further about $0.8''$ another diffuse region appears (e.g. Figure 2.5). Perucho et al. (2012b) proposed a disrupted jet due to a growth in **K**elvin-**H**elmholtz (KH) instabilities that interacts further out with the **I**nter **G**alactic **M**edium (IGM), resulting in shocks that allow one to explain the radiation further out.
Generally FR II jets eventually interact with the ambient medium, typically the IGM,

[1] http://www.physics.purdue.edu/astro/MOJAVE/sourcepages/0836+710.shtml

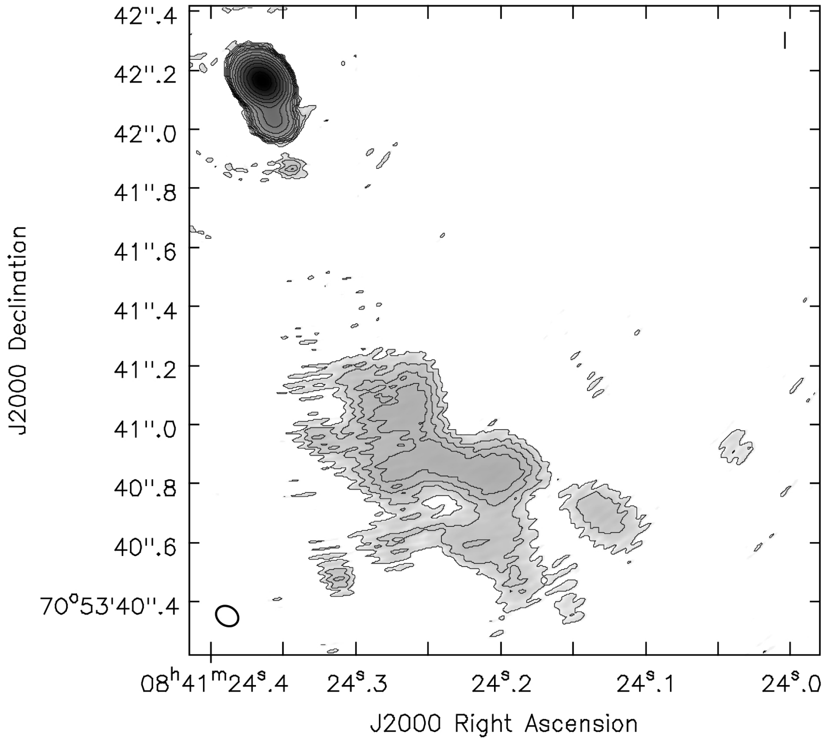

Figure 2.5.: EVN+MERLIN image of *0836+710* at 1.6 GHz. The contours are at 0.12, 0.15, 0.25, 0.33, 0.65, 1.2, 2.5, 5, 10, 20, 40, 80, and 99% of the image peak intensity (2.48 Jy/beam). The convolving beam is shown at the bottom-left corner (from Perucho et al. 2012b).

forming a hot spot. In this region the particles provided by the jet are decelerated and deflected into the lobes. Regarding this target though the component far out does not show any clear bow structure or a hot spot. The loss of jet collimation can lead to a lack of a reverse jet-shock as typically observed in FR I (e.g. Perucho & Martí 2007). Further the loss of collimation leads to a deceleration of the jet stream to a sub-relativistic or mildly relativistic broad flow (Perucho et al. 2005) that continues propagating until its interaction with the ambient region as observed.

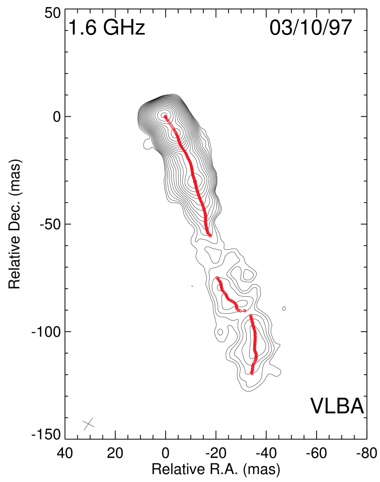

(a)

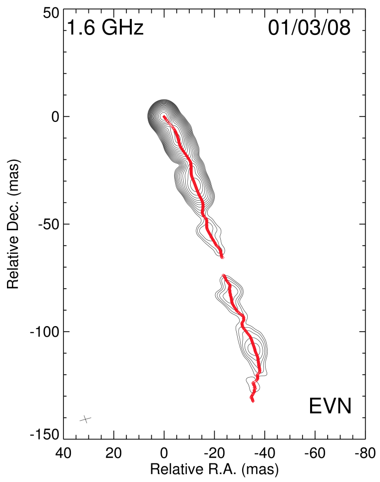

(b)

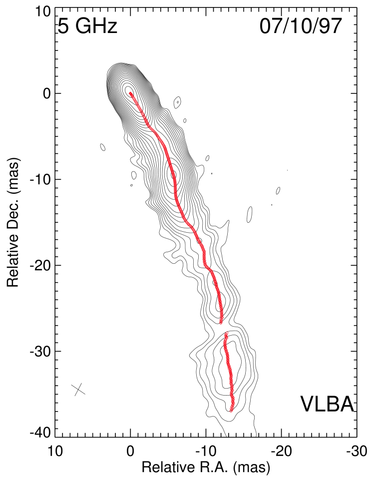

(c)

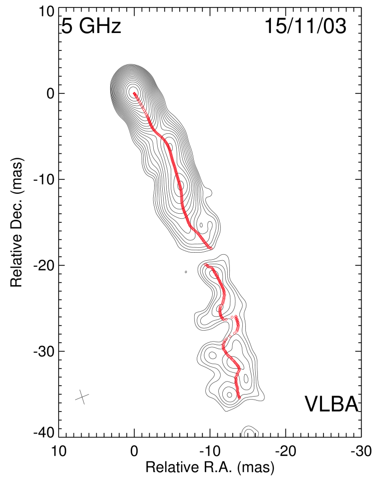

(d)

Figure 2.6.: Radio map of the VLBA and EVN of the jet in *S5 0836+710* at 1.6 GHz (top) in 1997 (a) and 2008 (b) and 5 GHz (bottom) in 1997 (c) and 2003 (d). Isocontours range from $2\,{}^{\mathrm{mJy}}/_{\mathrm{beam}}$ to $1.45\,{}^{\mathrm{Jy}}/_{\mathrm{beam}}$ in the 1.6 GHz images and from $1.5\,{}^{\mathrm{mJy}}/_{\mathrm{beam}}$ to $1.08\,{}^{\mathrm{Jy}}/_{\mathrm{beam}}$ in the 5 GHz ones. The beam property is indicated by the cross in the bottom left of each image with major and minor axes as well as the position angle. The red diamonds indicate the position of the ridge line (from Perucho et al. 2012a).

3. Radio observations

Multi-frequncy and multi-messenger detections are crucial to understand the underlying physics, especially, but not exclusively, for AGN observations. Hence radio telescopes cover only a part of the wide field of the observational astronomy, But to many processes this spectral window provides important insights that other frequencies or messengers cannot. Also radio astronomy offers well developed tools and techniques to achieve unmatched possibilities. Those will be covered in the following sections, that are based on Burke & Graham-Smith (2010), Taylor et al. (1999) and Thompson et al. (2001). Beginning with LOFAR, which is introduced in this chapter, we enter a new class of radio telescopes giving possibilities and challenges that we never faced before.

3.1. Radio single dish telescopes

Radio telescopes in most cases are single dish telescopes or consist of an array of those operated as a phased array or a VLBI network. Therefore it is important to understand how single dish telescopes work before presenting LOFAR and value more complex arrays and appreciate the major improvements provided by such telescopes.

Consider a coherent EM wave in the radio regime emitted by a source and collected by a dish (see Figure 3.1). Although this signal is in the radio, one can easily apply the physics of optics. The dish works as a mirror and reflects the incoming wave into the focal point. The geometry is perfectly engineered to compensate the different pathways for each different coherent wave to constructively interfere in the focal point. Here, an antenna can be placed to detect the signal. Some telescopes use a second reflective area and keep the antenna in the center of the dish. This is necessary to reduce the stress on the structure if the antenna is very heavy. Receivers in the focal point of the dish are replaced easier though, which is why this position is favored for test modules. In most cases an antenna is attached to this position which translates to a single pixel in an image.

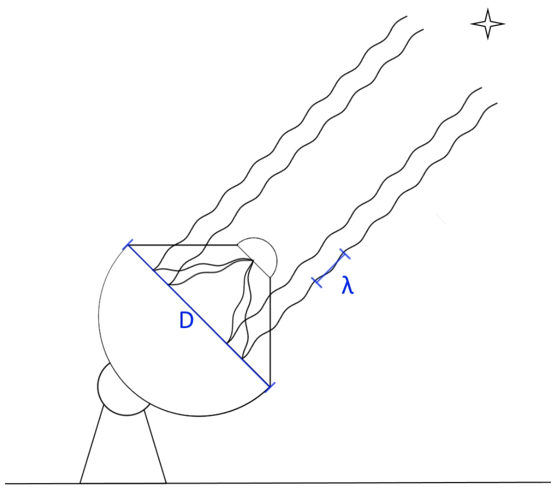

Figure 3.1.: Scheme of a dish-like radio telescope with a diameter of D observing a target, indicated with the star that emits a coherent monochromatic EM wave with the wavelength λ. The collected signal interferes constructively in the focal point of the telescope, where the antenna would be placed.

The dish size also dictates the best theoretical resolution that can be obtained. According to the Rayleigh criterion (e.g., Bass et al. 2001) the angular resolution can approximately be described by the following:

$$\sin(\alpha) \approx 1.22\frac{\lambda}{D} , \tag{3.1.1}$$

where α is the angle between the two closest points that can be distinguished (angular resolution), λ is the observation wavelength and D is the dish diameter of the telescope. Equation 3.1.1 can be used to calculate the resolution of the biggest radio single-dish telescopes in the world. Using the highest observable frequency of each telescope, the attainable resolutions are listed in Table 3.1.
Although it is to be noted, that the effective area is smaller therefore the true resolution is a bit, yet the order of magnitude is sufficiently described. These telescopes represent the largest telescopes with respect to their diameter that can be build and have hence the best resolutions that can be achieved with single dished radio telescopes up to now.

One can also place a module for so-called beam forming in the focal point. This allows to change the pathways of the different EM waves as desired and move the observation beam, which is the response function of the antenna, to another close location, improve

Table 3.1.: Short list of the worlds largest steerable and non-steerable dished radio radio telescopes. Respectively their highest observation frequency and their diameter are given with an resulting approximate resolution after Equation 3.1.1.

	Telescope	Diameter [m]	Frequency [GHz]	Resolution [arcsec]
steerable				
	Greenbank	≈ 100	≈ 100	≈ 7.55
	Effelsberg	≈ 100	≈ 86	≈ 8.78
non-steerable				
	Arecibo	≈ 305	≈ 10	≈ 24.8
	Guizhou FAST[a]	≈ 500	≈ 3	≈ 50.3

[a] **F**ive-hundred-meter **A**perture **S**pherical radio **T**elescope

the beam pattern and even reduce the beam width. This offers new observation techniques like using so-called multi beams. Here the module is a grid of small antennas. A subsequent correlator simulates the previous explained constructive interference of the EM wave signals. The timing in such a device can be adjusted before the signal is correlated and therefore a beam can be "formed" that can be repositioned and reshaped with different timings. Since this is done with computers, very small chunks of time intervals can be created and one can "jump" between different beams and therefore observe multiple targets at the same time. One project performed at **ASTR**onomisch **O**nderzoek in **N**ederland (ASTRON) is **APER**ture **T**ile **I**n **F**ocus (APERTIF) where Vivaldi antennas are used in a 11 x 11 matrix. These are used at the **W**esterbork **S**ynthesis **R**adio**T**elescope; Kronberg (1970) (WSRT) as a phased array. Figure 3.2 shows the APERTIF receiver on the test bench on the left side. On the right side an observation of the WSRT equipped with the new receiver shows a significant improvement in the **F**ield **O**f **V**iew (FOV). For comparison the old receivers had a FOV of the white circle what is about the size of the full moon.

Flux density

The measured flux density in radio astronomy is often given in the unit Jansky (Jy; e.g. Osterbrock & Ferland 2006) in honor of the radio astronomy pioneer Karl Guthe

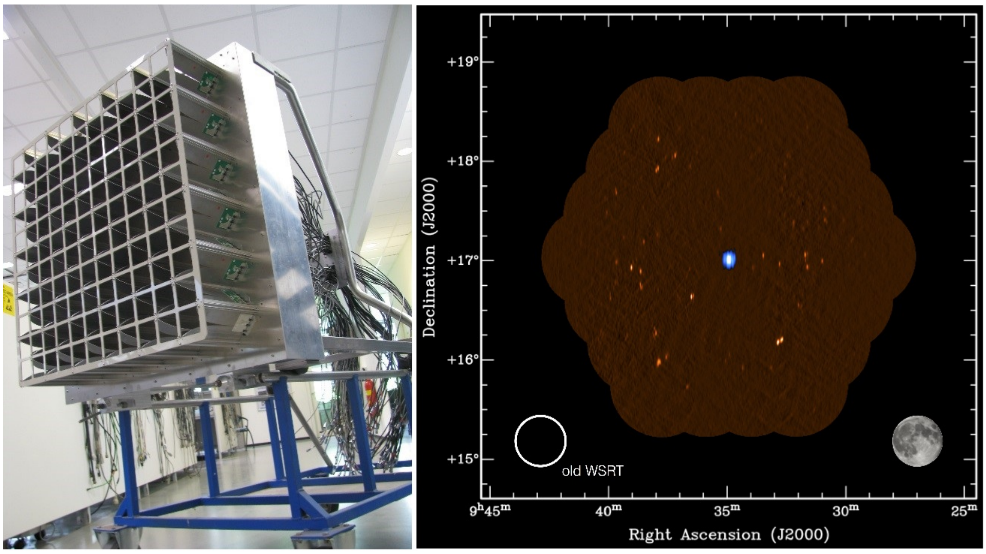

Figure 3.2.: The experimental APERTIF receiver on a mount for testing (left image). It consists of an 11×11-matrix of Vivaldi antennas. On the right image an observational result of the WSRT equipped with the APERTIF unit is shown. With the use of beam forming a much wider FOV can be achieved in comparison to a conventional antenna. Credit: NRAO/ASTRON.

Jansky (* 22.October 1905; † 14.February 1950). It is given as:

$$1\ \mathrm{Jy} = 10^{-26} \frac{\mathrm{J}}{\mathrm{s\ Hz\ m}^2} (\mathrm{SI}) = 10^{-23} \frac{\mathrm{erg}}{\mathrm{s\ Hz\ cm}^2} (\mathrm{cgs}) \ , \tag{3.1.2}$$

while the flux density for monochromatic radiation is generally computed as:

$$S = \iint_{target} \mathrm{B}(\theta, \varphi) \sin(\theta) \mathrm{d}\theta \mathrm{d}\varphi \ , \tag{3.1.3}$$

with B as the brightness distribution, θ and φ as the colatitude and the longitude. The integration is calculated over the whole target of interest. Other variations are also used where the beam of the telescope is used as the integration volume. The beam is the response function or point-spread function of the telescope. The full width half maximum also translates to the resolution. Since all rules of optics apply in radio as well, a radio telescope can be used as a transmitter as well as a receiver due to the time symmetry of the Maxwell equations (Jackson 1975). The characteristic emission of an antenna is therefore the same as the response function. An exemplary beam is shown in Figure 3.3. Adjacent to the main lobe there are side-lobes that can add radio interference to the collected signal. These can also detect other sources when pointing

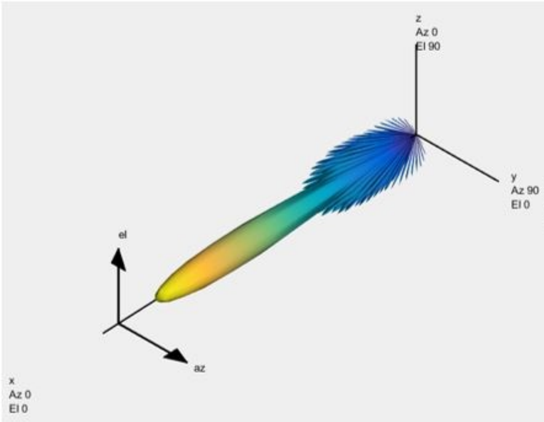

Figure 3.3.: Exemplary simulated directional radio response pattern, also called beam from Chen & Gentile (2016). The beam shows the highest sensitivity in the pointing direction, while still significantly smaller side lobes are visible.

to a target of interest and adding their flux to the feed. Reducing the side-lobes plays a very important role in improving the data quality.
Taking the telescopes attributes into account, the detected power can be described using equation 3.1.3 as:

$$\mathrm{P}(\theta,\varphi,\nu) = \int\limits_{\text{band}} \iint\limits_{\text{target}} A_{\text{eff}}(\nu)\, B(\nu,\theta,\varphi)\, \Pi_{\text{Ant}}(\nu,\theta,\varphi)\, \sin(\theta)\ \mathrm{d}\theta\mathrm{d}\phi\mathrm{d}\nu\ , \tag{3.1.4}$$

where the outer integral is applied to the bandwidth, A_{eff} is the effective collection area and Π_{Ant} is the response function.

3.2. Radio interferometry

Many fields of science rely on observations with resolutions of tenth of arc seconds or even milliarcseconds like studying the structure of AGN on kpc-scales or even down to sub-pc-scales (e.g., Müller et al. 2011). Since much bigger telescopes as stated above cannot be built and the frequency of interest is fixed, another technique is needed to achieve this. Radio interferometry is providing exactly that, realizing much better resolutions without the need of enormously sized single dishes but rather multiple smaller dishes. This concept will be explained with a two-element interferometer, i.e., two telescopes seperated by a distance d. As both telescopes are observing the same source, the telescope placed further away receives the same signal with a time delay of τ. This delay can be calculated by the angle θ.

$$\tau = \frac{d}{c}\ \sin(\theta)\ , \tag{3.2.1}$$

where c is the speed of light in the respective medium. The distance d is also referred to as the baseline b (in units of wavelengths b_λ). As already mentioned above, a correlator is used to add an instrumental time delay τ_i for the antenna with the shorter path in order to compensate for the geometric delay. The correlator also integrates the signal for a given interval and combines those. This creates a time-averaged product also known as cross power product. Following this technique with multiple telescopes in an array and therefore multiple baselines the telescope network can be treated as one big dish with the diameter of the longest baseline. Therefore the resolution can be significantly increased as it follows equation 3.1.1.

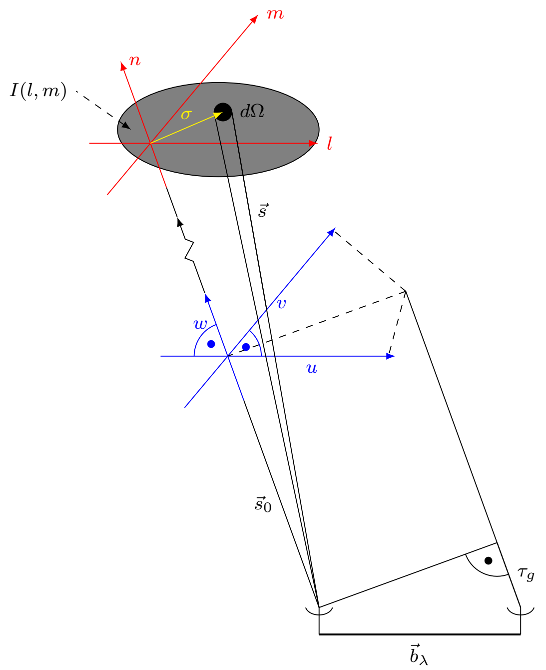

Figure 3.4.: Concept of common coordinate systems: Two antennas are connected by a baseline $\vec{b}_\lambda$. Monochromatic EM wave emitted by a source (grey), from which the brightness distribution is described with respect to the $(l, m.n)$-system (red) at the left reference antenna and with a geometric delay τ_g at the right antenna. The baselines of the array are described in the (u, v, w)-system (blue). Credit: Burd (2017).

Fourier **T**ransformation (FT) is crucial to understand how interferometry works. Further a (u, v, w) space is defined as shown in Figure 3.4. A baseline between two telescopes transformed in this space represents a vector starting at the origin with an orientation respective to the target. The units are generally given in λ. So i.e., a multiple of the observation frequency. The w coordinate therefore corresponds to the height above or below the (u, v)-plane. If all participating telescopes would be placed in one plane, there would be no w contribution at all. Adopting this approximation, the (u, v, w) space can be reduced to a (u, v)-plane. While the observation is taking place, the earth rotates. Likewise, this causes the angle of the baselines with respect to the target to rotate, resulting in a scan in the (u, v)-plane which is called (u, v)-coverage. An exemplary coverage of 0836+710 observed by LOFAR is shown in Figure 3.5. Each point represents a visibility of a baseline. Note that the point symmetry is induced by the FT symmetry. Describing all visibilities in the (u, v, w) space it can be written according to Cornwell & Perley (1992):

$$V(u, v, w) = \int \mathrm{d}l \int \mathrm{d}m \, \frac{I(l, m)}{\sqrt{1 - l^2 - m^2}} \, \mathrm{e}^{-2\pi i (ul + vm + w(\sqrt{1 - l^2 - m^2} - 1))} \, . \tag{3.2.2}$$

Assuming a small FOV, the w-term can be approximated $\sqrt{1 - l^2 - m^2} \approx 1$. In such cases the w-contribution vanishes. While working with a big FOV, effects of non-coplanar baselines can be seen in the data e.g., smearing out structures the further the structure that is located away from the phase center. One possibility to deal with it is changing the phase center to another position and re-image the field, also referred as "Mosaicking" in the literature (e.g., (Intema et al. 2016)). Another method is calculating the effect of the w-projection into the imaging algorithm which is currently tested only in **C**ommon **A**stronomy **S**oftware **A**pplication; Jaeger 2008 (CASA). Performing a FT on the visibilities in the (u, v)-space a brightness distribution is obtained in the (n, l, m) space. It would represent the true brightness distribution, if the (u, v)-plane is infinitely wide and dense populated. Since there are gaps in the (u, v)-coverage, reconstruction methods of the true brightness distribution have to be applied.

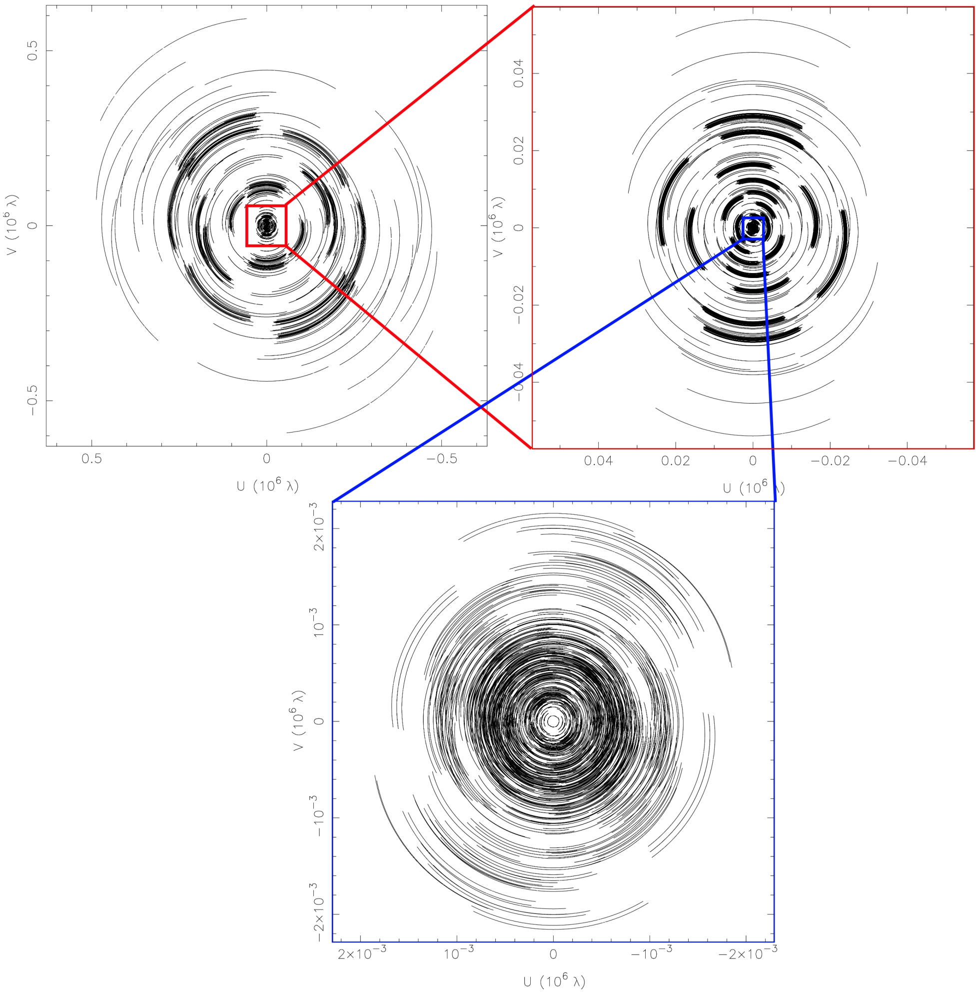

Figure 3.5.: Full (u, v)-coverage of the observation of *S5 0836+710* performed with the ILT. The wide range of baselines that the ILT offers can be seen here significantly.

3.3. The Low-Frequency Array (LOFAR)

Figure 3.6.: Image of the superterp. It is part of the core of LOFAR located near Exloo, Netherlands. It is build up of six stations (six LBA and twelve HBA fields) that can be seen in the image. Credit: ASTRON/LOFAR

The phased array LOFAR operates in the northern hemisphere in the radio regime, more specifically at long wavelengths between 90 - 240 MHz. It has been operated by ASTRON since 2012 and consists of 38 stations in the Netherlands. 24 of those form the so-called core stations and can be identified in the station list with a leading 'CS' string. The other 14 are remote stations that are further away distributed throughout the Netherlands and can be identified by the leading string 'RS'. The core stations are located near Exloo. These form the core of LOFAR and are distributed within a two kilometer radius. The most inner part is the so-called superterp and consists of six core stations (CS002, CS003, CS004,CS005, CS006, CS007). They are located closest together than any other LOFAR stations as seen in Figure 3.6.
Each station has two types of antennas, the **L**ow **B**and **A**ntenna (LBA) and HBA.

The ILT

There are also twelve stations operational outside the Netherlands, the international stations. Six in Germany, one in France, one in the United Kingdom, one in Sweden and three in Poland. The polish stations were not yet operational during the observations that are analyzed in this work. Also another station in Ireland is being built currently. The locations of the stations are shown in Figure 3.8 while the international station design shows one HBA and one LBA field and is shown in Figure 3.7. Together with the LOFAR stations, that are only the core and remote stations in the Netherlands and the international stations the array creates the **I**nternational **L**OFAR **T**elescope (ILT). The data processed in this work is the result of an ILT observation.

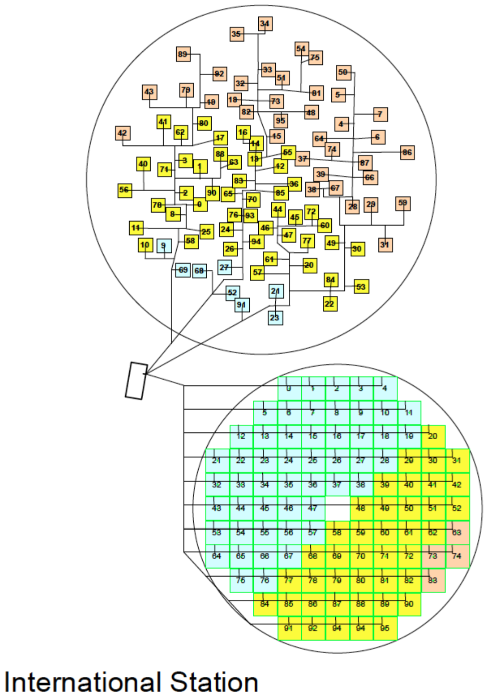

Figure 3.7.: International stations consist of a 70 m wide LBA array with 96 elements, a 56.5 m wide HBA array consisting of 96 antenna tiles and a total of 96 digital Receiver Units. Credit: ASTRON/LOFAR.

Low band antenna (LBA)

The LBA (see Figure 3.9) operates between 10-90 MHz. It has a **P**oly**V**inyl**C**hlorid (PVC) tube carrying the signal cable to the top where the low noise amplifier is positioned. The four cables attached to the ground in a 45° angle are the receiving elements and detect either an X,Y polarized signal or a total flux for which both signals are combined. One core station or remote station contains 96 antennas in the field within a diameter of 87 m attached to 48 receivers. An international station also has 96 antennas, here with a diameter of 70 m and 96 receivers. When observing with these antennas, the user can choose between the following modes[1]:

- *LBAOUTER*: Select the 48 outermost antennas in the field. This is a mode intended for observations below 40 MHz. Array width: 87 m.

[1] https://www.astron.nl/radio-observatory/astronomers/users/technical-information/lofar-stations/lofar-stations-description-

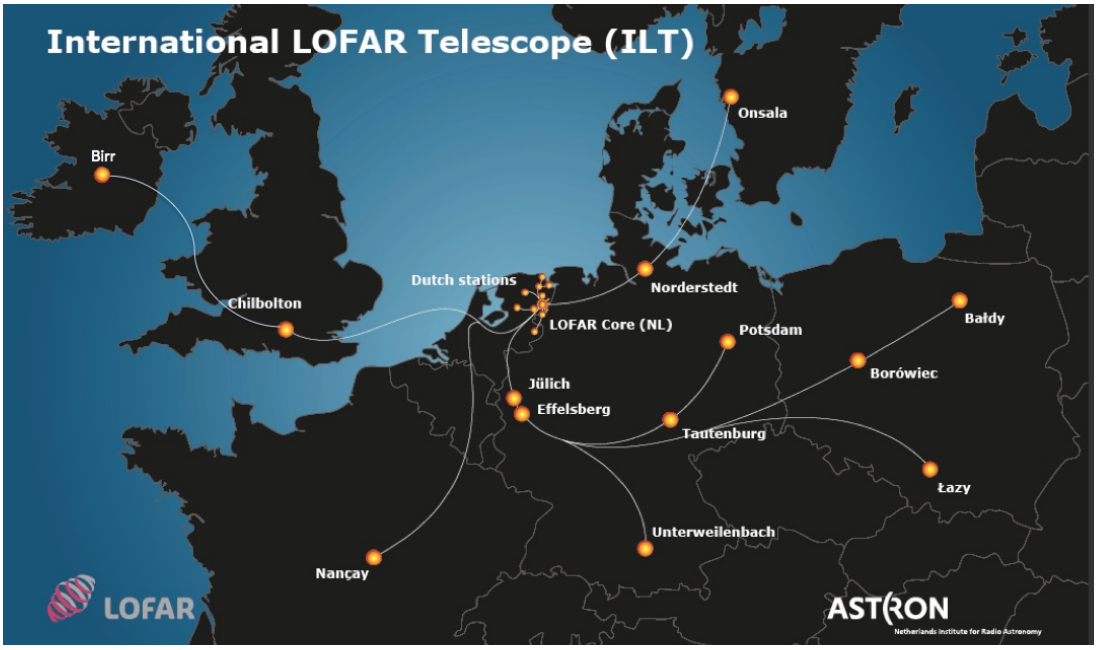

Figure 3.8.: This map of Europe shows the location of all stations of the ILT. The Irish station in Birr is not yet constructed. The three polish stations are operational, but were not at the time of observation for the data handled in this thesis. Credit: ASTRON/LOFAR.

- *LBAINNER*: Select the 46 innermost antennas plus 2 outer ones as calibration antennas. These are used to resolve out the Milky Way. This is a mode intended for observations above 40 MHz. Array width: 30 m.
- *LBASPARSE*: Selects half of the innermost and half of the outermost antennas (48 in total). Sparsely filled array width of 87 m. This mode is intended for intra-station baseline or low resolution all-sky observations.
- *LBAX*: All 96 antennas with X polarization (NE to SW).
- *LBAY*: All 96 antennas with Y polarization (NW to SE).

A mode where all antennas observe in both polarizations is not possible, because there are not enough receivers for that. In an observation with international stations only, there is however no such limitation.

Observations with the LBA are still very challenging, since there is no sufficient sky model present at the moment for calibration. Also a lot of interference due to bright sources like CygA or PerA or even ground based interference due to radio transmissions, devices and machines cannot be removed that easily from the data and therefore increase the noise level.

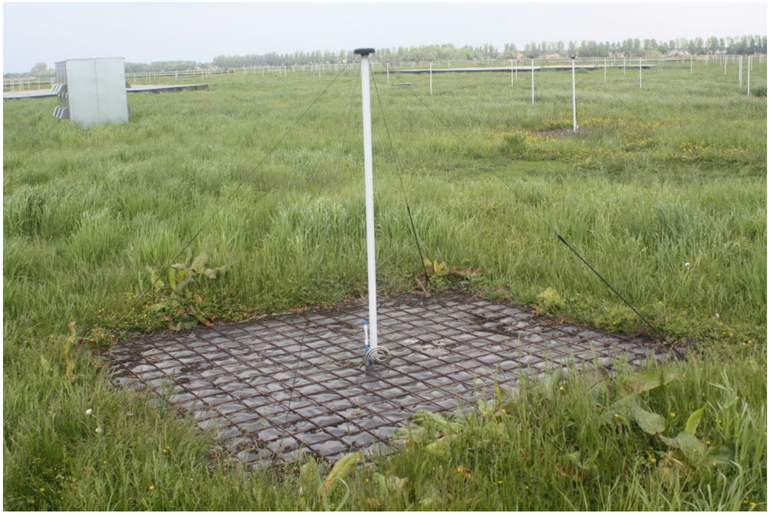

Figure 3.9.: An Image of a LBA unit. The tube is holding on top the receiver unit attached to the four dipoles aligned that way to realist linear polarization measurements. Credit: ASTRON/LOFAR.

High band antenna (HBA)

The HBA performance is optimized for a frequency range between 120-240 MHz. One antenna is build into a Styrofoam-cube (see Figure 3.10 left) where four metal triangles are placed, these are the dipoles that detect linear polarized signal. Antenna cubes are arranged into a 4 x 4 configuration and a protective black cover that forms a tile (Figure 3.10 right). Core stations have two HBA fields each with 28 tiles and 30.8 m diameter. Remote stations use one field with 48 tiles and a diameter of 41 m. International stations consist of 96 tiles with a diameter of 56.5 m. The Effelsberg station in Germany is the only exception here because the surrounding area forced the design to be slightly elliptical rather than circular. The observer can choose between the following observation modes when core stations are in use[2]:

- *HBAzero/HBAone*: Uses only one of the core station tile fields (field zero or field one).
- *HBAdual*: Each tile field is treated as an individual station in the correlator. This yields to many more short baselines.
- *HBAjoined*: Each core stations' tile fields are firstly correlated together before transmitted to further processing. This yields to a non-uniform shape of the

[2] https://www.astron.nl/radio-observatory/astronomers/users/technical-information/lofar-stations/lofar-stations-description-

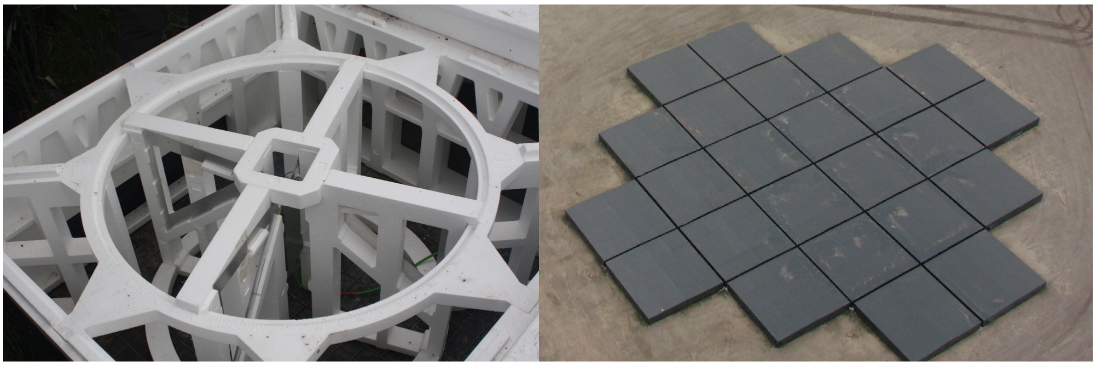

Figure 3.10.: On the left the uncovered box of the HBA unit is shown. The triangular metals are the dipoles, measuring therefore in linear polarization. On the right the black casings in which the HBA of LOFAR are housed are shown as tile field. Credit: ASTRON/LOFAR.

beam.

- *HBAzero_inner*: Only the inner 24 tiles in the remote stations are used to match the design of the core station.

The processed data are this thesis is observed with the HBA in the *HBAdual* mode. The station design for core and remote stations is displayed in Figure 3.11. Here you can see the separated HBA fields in the core stations.

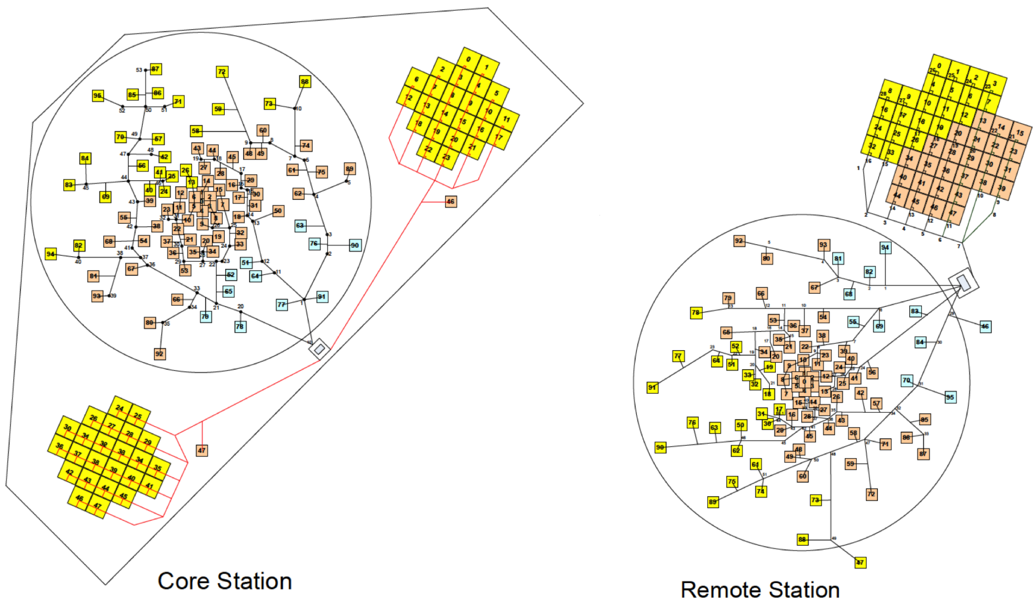

Figure 3.11.: Core stations consist of 48 HBAs and 96 LBAs and a total of 48 digital Receiver Units. The HBAs are arranged in two 24-element fields with a diameter of 30.8 m each, straddling an 87 m diameter LBA field. Remote stations consist of 48 HBAs arranged in a single 41 m diameter field and 96 LBAs arranged in a single 87 m diameter field and a total of 48 digital Receiver Units. Credit: ASTRON/LOFAR.

3.4. Interferometry with LOFAR

As discussed before in section 3.3, LOFAR does not utilize a dish-like design for the telescopes in the array. The reason for that is a major point why LOFAR is such a special telescope. It was described how baselines can be used to create large virtual telescopes in order to increase the resolution of a telescope(-array). LOFAR is using the very same principle to create very small baselines. A dish can be seen like an analogue interferometer. The signal is correlated in the focal point through the geometric properties of a dish. The same is done with the long baselines, meaning the signal is correlated in a virtual focal point. Hence any radio dish can be "decomposed" in smaller telescopes - or even simpler into dipoles. With that, arrays of dipoles can be built up that together form a virtual telescope. Distributing fields spatially builds up an even larger virtual telescope. The simulated beam pattern for an HBA field achieved with this technique is shown in Figure 3.12.

As one can see, there are still dominant side lobes that can pick up emission in the observation but combining it with multiple stations those side lobes can be reduced drastically. The benefits are clearly that large telescope constructions that have im-

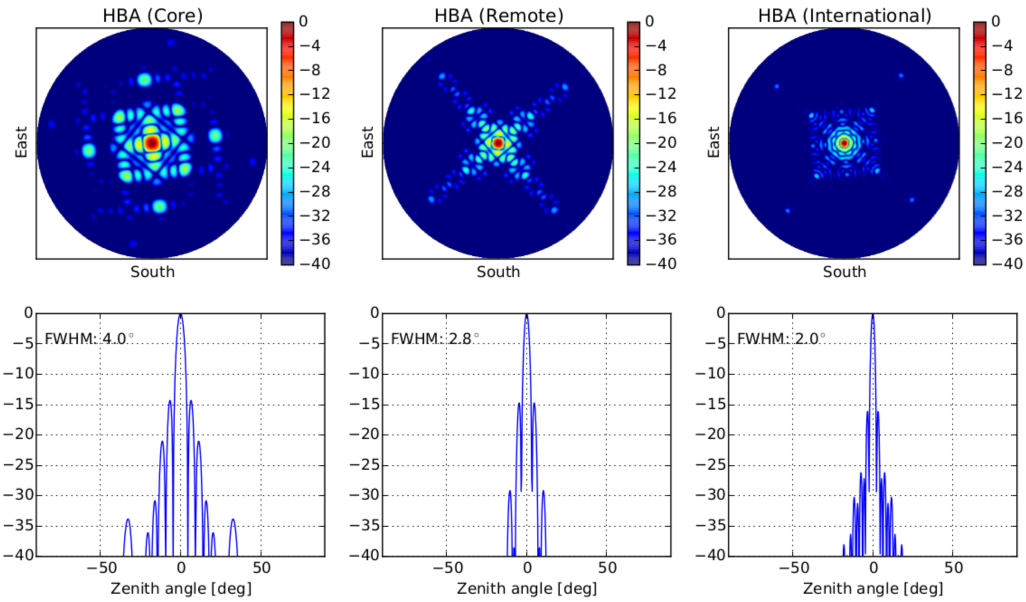

Figure 3.12.: The modeled beam pattern for the HBA stations (top images) and respectively a cut in east direction (bottom images) presented by Brentjens (2016). The applied beam modeling shows tighter beams for stations that are further out due to the increasing size of the antenna fields.

mense costs in terms of engineering do not need to be built. There are also no moving parts at all, so the maintenance is very cheap. Less people have to stay at the telescope sites to keep everything running, since the antennas and correlator are all fully electronically. Moving the beam between targets also happens basically immediately because no dish has to slew to a new position. Instead, multiple targets can be observed at the same time. LOFAR can point to up to six omni directional targets simultaneously. These types of telescopes are therefore also referred as software telescopes, since the real challenge and expensive part of a software telescope is computers and software. LOFAR creates about 6 TB of calibrated data per hour. The intermediate data size is many times larger but is not stored for long term archiving. Also, not all raw data is stored, most of it is further reduced due to flagging and amplitude and phase averaging in order to reduce file sizes. Still this creates archive data per year in the order of tenths of Peta Bytes (Begeman et al. 2011). With a maximum of 74 stations (HBAdual + int: 24 x 2 (CS) + 14(RS) + 12(INT)) 2701 individual baselines can be obtained. These are spread in a very wide range, creating dense (u, v)-coverages that realize high sensitivities combined with high resolution at low frequencies. These properties are sufficient to detect and measure diffuse un-beamed structures at low frequencies around AGN as performed in this work. Currently only LOFAR provides these unique capabilities.

3.5. Hybrid Imaging

Because of the fact that the image capturing, as introduced above, takes place in the Fourier space with the dimensions in baselines, the image reproduction is more complicated than in direct imaging. One possible way is the so called hybrid imaging (also called hybrid mapping), although correlation and many calibration steps have to be taken place at this point already, like flux calibration, bandwidth calibration, beam calibration for individual stations and a first phase calibration called fringe fitting. One starts with creating a so called dirty beam (which is the Fourier transformed (u, v)-plane). This is used to convolve a first model, that is simply a point source matching the best results to represent the observation. Calibration in amplitude and phase (in more detail see Thompson et al. 2001) is being applied on the data to increase the match to the model, while trying to conserve the total flux, though it is possible to violate this if needed. Multiple iteration steps start from there, adding more point sources if needed to further improve the match of the model to the observation. These components are called clean components derived from the process called *CLEAN* algorithm Högbom (1974). When the iterative process is not increasing the model to match the observation further on, there should only be a difference in these describing a reasonable noise. In the case this is not achieved, either the calibration before the hybrid imaging is not sufficient or the objected target has a too complex structure to be described with point like model components. Following these steps, the use of computational methods is unavoidable due to the amount of data. The implemented software called Caltech **DIF**ference **MAP**ping; Shepherd 1997 (DIFMAP)[3]. For a more detailed introduction see Kappes (2013).

[3] ftp://ftp.astro.caltech.edu/pub/difmap/difmap.html (2017 February 21) official homepage for more details and downloading DIFMAP

4. Observation and data processing (processing pipeline)

As part of project LC4_026, *S5 0836+710* was observed on 2015 June 17 for 4 hours with the flux density calibrator *3C 196* for one hour in the continuous frequency coverage between 117.5 - 162.6 MHz split into 231 subbands. The observation mode was chosen to be *HBAdual* together with international stations. At the given time this included 6 stations in Germany (DE601-DE605,DE609) and one each in Sweden (SE607), France (FR606) and the United Kingdom (UK608). 23 core stations and 13 remote stations were observing (CS013 did not participate, RS305 had a broken hard disc). In the following paragraphs, the different aspects of data reduction will be discussed in detail with the observational specific values without the loss of generality. Hence this pipeline can be applied to any LOFAR HBA observation that finished the radio observatory pre-processing described in the next section. The subsequent sections will describe the elaborated pipeline in this project which is partially familiar to the LBA pipeline presented by Morabito et al. (2016a) and Morabito et al. (2016b).

4.1. Radio observatory processing

The data were recorded in 8-bit mode and were correlated with the **CO**rrelator and **B**eamforming **A**pplication platform for the **L**ofar **T**elescope; ASTRON 2017 (COBALT) correlator producing all linear correlation products (XX,XY,YX,YY). Afterwards the data were pre-processed at the radio observatory in multiple steps. The RFI was extracted by the AOFlagger (Offringa et al. 2010) with the default HBA flagging strategy. 16 channels were averaged per subband. A time average also was applied over 4 time steps of initial 4 seconds of integration time resulting in timesteps of 16 seconds. The flux calibration was applied on the core stations while also applying the so-called demixing (Van Der Tol et al. 2007), which is removing the influence of strong sources like CasA or TauA. The FOV of the remote and international stations is not wide enough to allow for flux calibration. Finally the data were uploaded to the LOFAR **L**ong **T**erm **A**rchive (LTA)[1] in the **M**easurment **S**et (MS) format[2]. These steps were performed by the radio observatory and are therefore not explained in more detail in the following

[1] http://lofar.target.rug.nl/Lofar; 2017 April 21

[2] http://www.lofar.org/wiki/lib/exe/fetch.php?media=public:documents:ms2_description_for_lofar_v05.pdf; 2017 April 21

paragraphs. In this thesis context, the data at can be seen as raw data this point, knowing that calibration steps have already been performed on it.

4.2. Data calibration

The first part of the subsequent calibration is performed at the LOFAR calibration server at the University of Wuerzburg. This server is solely designed to perform calibration on LOFAR data. Therefore two INTEL XEON E5-2687W V4 processors with each twelve physical cores and enabled hyper-threading providing each 24 threads (virtual cores) at 3.00 GHz with 512 GB of **R**andom-**A**ccess **M**emory (RAM). The hard drives are separated into two modules each set up with **R**edundant **A**rray of **I**ndependent **D**isks-Level 5 (RAID5) and have a usable volume of 58 TB each. The final calibration steps and the imaging procedure is handled on two similar dedicated computers with an INTEL CORE I7-6700K processor with four cores and enabled hyper-threading providing 8 threads, over-clocked to 4.50 GHz with 32 GB of RAM. The hard drives are set up in RAID5 and have a usable volume of 11 TB. The server's and computers' hardware properties meet the demanding needs of LOFAR data in order to calibrate data and produce the images. The block diagram in Figure 4.1 shows the calibration procedure which was performed with the **N**ew **D**efault **P**re-**P**rocessing **P**ipeline (NDPPP)[3], **A**stronomical **I**mage **P**rocessing **S**ystem; Greisen 2003 (AIPS) and python scripts. The hybrid-imaging process was performed using the DIFMAP program. The written pipeline scripts are attached in appendix C.

Forming the superterp or superstation

After retrieving the data from the LTA the superterp station is formed with the innermost twelve core stations (six in general but twelve due to *HBAdual* mode) using the *stationadder* procedure in NDPPP. Afterwards the stations forming the superterp are filtered out with the *filter* procedure in NDPPP. This can generally be done with all core stations where the phased up station is referred to as superstation, reducing the amount of baselines and therefore visibilities drastically. Depending on the dataset and the computation possibilities it is recommended to use the one or the other. If computing time and disk space is limited and the target is fairly bright ($\gtrsim$ 1 Jy) it is sufficient to work with a superstation. Creating any phased up station with any subsample of stations is called a tied station. Keeping in mind that the phased-up station could have an intrinsic phase delay that cannot be corrected anymore. This means that the stations might have a phase delay due to different ionospheric conditions, depending on the telescopes position on earth (e.g., Intema 2007; Intema et al.

[3] See Sect. 4 of "The LOFAR Imaging Cookbook", ed. A. Shulevski et al. 2016, Astron Technical document.

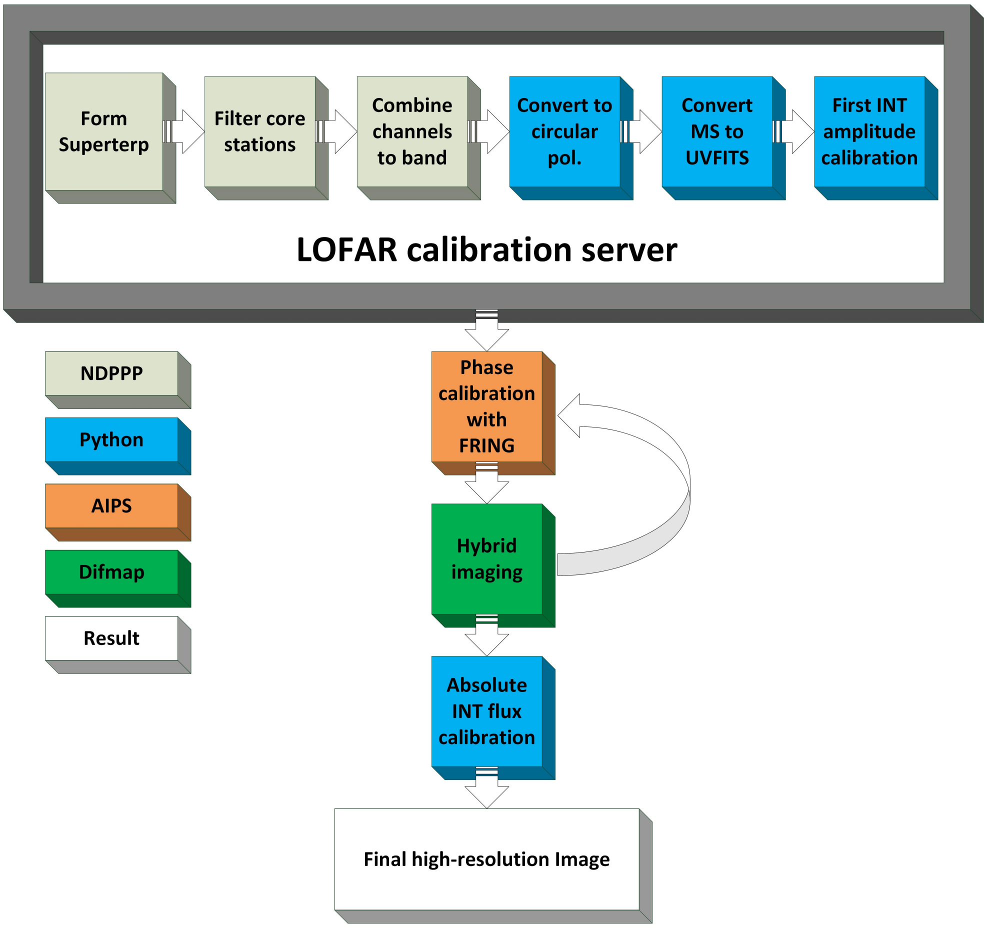

Figure 4.1.: Flowchart of the elaborated calibration routine that can be handled as a pipeline up to the hybrid imaging. The first steps are run on a dedicated calibration server located at the University of Wuerzburg. These steps are enclosed with a gray box. The following steps can be performed on any computer. The steps are color coded, indicating what software package is used at this point.

2009). When phasing them up, there is no way to modify the phases of each station respectively anymore. The correction of phase delays is performed much later in the process when fringe fitting is performed. Note that ionospheric phase delays become very significant below $\sim 200\,\mathrm{Mhz}$ and are dispersive. These can be either calculated by **G**lobal **P**ositioning **S**ystem (GPS) data or by modeling procedures, like *FRING* in AIPS. Due to the phased-up collective area, this station will have a much higher weighting in contrast to the others. This is generally depending directly proportional on the collective area, which is in the case of the superterp a factor of ~ 100 with

respect to one core station. If the data from that station happens to have bad data, this will impact the following procedures significantly, reducing the overall **S**ignal to **N**oise **R**atio (SNR). On the other hand the phased-up station yields higher sensitivity due to the larger size.
If computing resources are not an issue it is recommended to work without phased-up stations or at the most with the phased-up superterp. In that case barely any intrinsic phase delays occur due to the close geographic location of the stations forming the superterp. These are spread out on a field with the diameter of about 300 m. The most distant core stations are separated by about 5 km. With a smaller virtual collective area this station is also not extremely overweighted, allowing bad visibilities not to affect the whole dataset. Although this leads to less sensitivity as with the superstation, the overall SNR improves generally due to better calibration. Also further time and frequency averaging together with self calibration which is happening in the later stages will improve this further. This procedure takes the weighted average of all visibilities on baselines between the phased-up station and the other stations. The new (u, v, w)-coordinates are calculated as the weighted geometric center of the (u, v, w)-coordinates of the combined visibilities.

Average sub-bands to bands

After creating the tied station (this can be either the superterp or superstation - in this thesis it is the superterp) all visibilities are averaged starting from 231 subbands with a bandwidth of 192 kHz each between 118 - 163 MHz to 14 bands with a resulting bandwidth of 3.12 MHz. Generally the few first bands and last few bands show deviations compared to the rest of the data especially due to the band pass shape. Therefore the first three and last four subbands are not used, resulting in 14 bands. Each band averaged over 16 subbands. This averaging step is performed in NDPPP.

Conversion to circular polarization

LOFAR, as stated before, is observing in linear polarization mode. At low frequencies differential Faraday rotation from propagation of the EM wave through the ionosphere has to be taken into account. The flux density can shift from the XX and YY polarization to the cross hand polarizations. The impact to the data can be reduced to an offset of a L-R phase when converting it to circular polarization. This step is performed with Table **Q**uery **L**anguage; van Diepen 2015 (TaQL) which is a tool in the CASACORE[4] package, accessed through a python script.

[4] https://github.com/casacore/casacore; 2017 April 21

Convert to UVFITS format and time independent visibility scaling

Many astronomical software packages cannot handle MS files for the time being but rather use the **F**lexible **I**mage **T**ransport **S**ystem; Wells et al. 1981 (FITS) file format. Therefore the datasets are converted with *ms2uvfits*, which is a CASACORE package accessed through a python script.
At this point only the visibilities amongst core stations are flux density calibrated therefore all others stations need to be at least time independently rescaled to continue with fringe fitting. This is realized with a python script, that calculates the median of the visibilities amongst core stations and one median value for all other visibilities. The ratio of those two values is the correction value applied to the visibilities of international and remote stations. After this step the data is moved to the imaging computers to perform fringe fitting, which still is only reliably performable in AIPS. This software requires single core power, which is best provided by the dedicated computers with much higher core frequencies then the servers'.

Phase calibration

The phase calibration is performed in two steps. In both the data is phase calibrated with the *FRING* function in AIPS for only core stations and afterwards for only remote and international stations. In the first step a point source in the phase center is assumed for the phase calibration. The calibrated dataset is used to create a high resolution image with international and remote stations and a low resolution image with only core stations. These images are created by hybrid imaging in DIFMAP. The results are used as a model to re-do the phase calibration in a second run on the initial data improving the overall phase calibration.

Final hybrid imaging

The phase calibrated data are eventually imaged by hybrid imaging in DIFMAP. This results in two images per band, where one is obtained by only core stations and the other with only international stations and the superterp.

4.3. Absolute flux calibration on high resolution images

Since the lower resolution image using only the core stations is amplitude calibrated, the higher resolution image can be scaled by a correction value while assuring it picks up all flux that the core stations show for the target. Using only international and remote stations, the FOV is large enough to exceed the beam size of a core station only image. Such images do not show other structure within the beam size of the core station only image than picked up by the images gathered from international stations with the superterp. Therefore visibilities contributed by remote stations are not considered at this point anymore. The total flux picked up in the high resolution images is calculated and used to compute the correction factor. This is applied to the clean components while afterwards calibrating the visibilities to this model with the *gscale* command in DIFMAP allowing to violate the conservation of flux. This process leads to fully calibrated high resolution images with the ILT.

5. Results of the pipeline's application on *S5 0836+710*

Following the described steps for calibration and hybrid imaging in chapter 4 we obtain 11 images of *S5 0836+710*. Four frequency bands had to be discarded due to insufficient data quality, presumably due to the bandpass shape and RFI. For all calculations a Hubble constant, given in **S**ystème **I**nternational (SI) units is assumed to be $H_0 = 67.8\,\mathrm{km/s\cdot Mpc}$, $\Omega_\mathrm{m} = 0.308$ and $\Omega_\Lambda = 0.692$; consistent with Ade et al. (2016). The resulting images are listed in the following table with their measured properties each with a bandwidth of 3.12 MHz:

Table 5.1.: Calibrated images of *S5 0836+710* with their measured properties

Central Frequency in MHz	Figure	F_core in Jy	F_ext in Jy	F_comp in Jy	$F_\mathrm{low\text{-}res}$ in Jy
126	A.1a	1.88 ± 0.30	1.31 ± 0.20	1.62 ± 0.10	4.72 ± 0.034
129	A.1b	1.85 ± 0.30	1.32 ± 0.20	1.59 ± 0.10	4.70 ± 0.034
132	A.2a	1.53 ± 0.30	1.50 ± 0.20	1.60 ± 0.10	4.75 ± 0.034
135	A.2b	1.90 ± 0.30	1.36 ± 0.20	1.26 ± 0.10	4.68 ± 0.034
138	A.3a	2.10 ± 0.30	1.08 ± 0.20	1.43 ± 0.10	4.62 ± 0.034
141	A.3b	1.99 ± 0.30	1.20 ± 0.20	1.51 ± 0.10	4.63 ± 0.034
144	A.4a	1.56 ± 0.30	1.69 ± 0.20	1.46 ± 0.10	4.62 ± 0.034
151	A.4b	2.29 ± 0.30	0.98 ± 0.20	1.32 ± 0.10	4.58 ± 0.034
154	A.5a	2.10 ± 0.30	1.10 ± 0.20	1.43 ± 0.10	4.64 ± 0.034
157	A.5b	2.53 ± 0.30	1.02 ± 0.20	1.20 ± 0.10	4.62 ± 0.034
160	A.6	2.23 ± 0.30	1.13 ± 0.20	1.25 ± 0.10	4.57 ± 0.034

5.1. Images

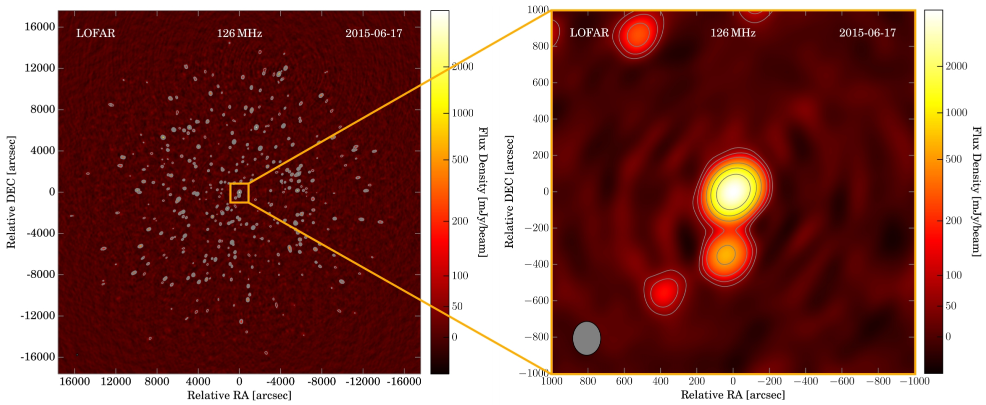

Figure 5.1.: Image observed by the core stations only. On the left the whole FOV is shown with a diameter of about 8°. On the right a zoomed-in field of the central part is shown with the observation target *S5 0836+710* in the phase center. For both images the beam size is (186 × 155) arcsec with a position angle of −36.0° and the contour levels are chosen to be at -50, 50, 100, 200, 500, 1000, 2000 Jy/beam with a noise RMS of 0.555 mJy/beam.

The aforementioned step to improve the fringe fitting via working with core stations only first results in a wide field image shown in Figure 5.1. Many bright sources are visible that must be considered in the sky model to correctly apply calibration to the phases. The observation target is only a point source for the core stations due to the lack of long baselines, as seen above.

The whole source morphology is only visible for the high resolution images obtained through the international stations. When inspecting the images we can find high consistency in morphology and flux distribution throughout the frequency bands. When averaging all images with their brightness distribution, obtaining a so called stacked image we obtain Figure 5.2a. We can test for the consistency within the bands by creating a median image (Figure 5.2b). A supposedly band that deviates significantly from the others would impact the mean image, but not the median image. To inspect the differences in a more quantitative way, a map showing the differences for each pixel, here also called residual image (Figure 5.3), helps to investigate. We show the same contour levels as for the other two maps. It can be seen that the first contour level is reached only very occasionally which indicates the mentioned consistency amongst the bands.

The overall morphology shows a bright central region with the unresolved core and additional extended emission containing about 70% of the total flux. In the south west direction a triangular shaped region with the remaining flux can be identified in all frequency bands showing a lobe like structure containing a presumable hot-spot. Extended emission at the central region reaching in the north east direction is seen in the model components but does not reach the first contours. Further investigation in this data with increasing the SNR can lead to a reliable statement that can not be provided with the current dataset.

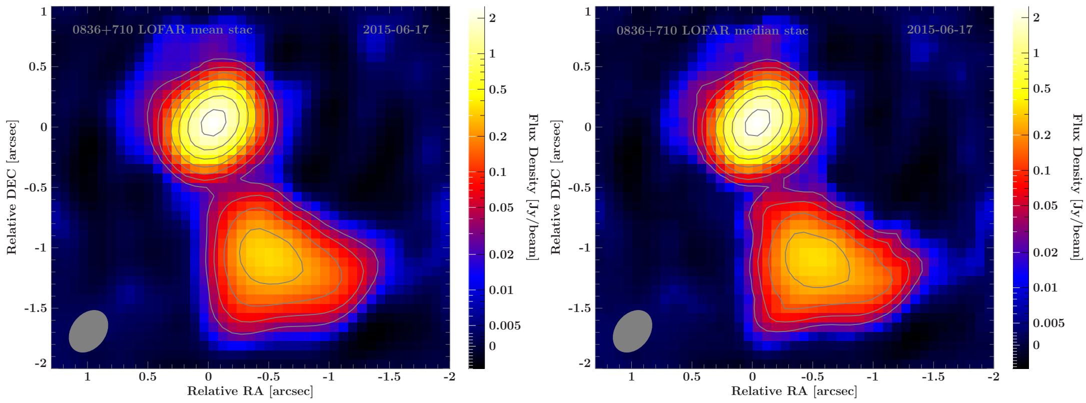

(a) **(b)**

Figure 5.2.: Stacked LOFAR image over the full calibrated frequency range (126 - 160 MHz) where the average (a) or median (b) values are calculated per pixel position and displayed in color scale. Both images show very a similar morphology and intensity distribution. Consequential there is a high consistency amongst the individual images. The lowest contour level marks with a 3σ threshold. The contour levels are -0.031, 0.031, 0.061, 0.12, 0.24, 0.49, 0.98, 2.0, 3.9, $7.8\,{}^{\mathrm{Jy}}/_{\mathrm{beam}}$. The **R**oot **M**ean **S**quare (RMS) is $0.0102\,{}^{\mathrm{Jy}}/_{\mathrm{beam}}$. The beam size is $0.459'' \times 0.308''$ with a position angle of $-39.1°$.

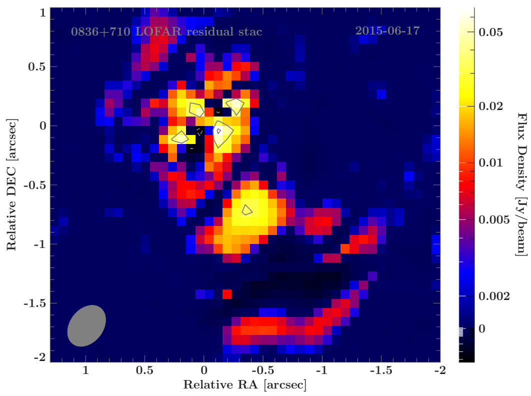

Figure 5.3.: Difference map between the mean and median stack image in Figure 5.2. The contour levels are chosen to be as presented in Figure 5.2 to allow easy comparability.

Other telescope observations

VLA data and **E**uropean **V**LBI **N**etwork; Schilizzi 1980 (EVN) combined with **M**ulti-**E**lement **R**adio **L**inked **I**nterferometer **N**etwork; Thomasson 1986 (MERLIN) data of *S5 0836+710* show a comparable FOV and resolutions allowing further consistency checks.

VLA

The VLA data for the given target at 4.8 GHz in A configuration has similar beam parameters as the LOFAR observation, listed in Table 5.2. Also the structure as seen in Figure 5.4 describes the same morphology as seen in the LOFAR images. This further confirms the validity of the obtained LOFAR images.

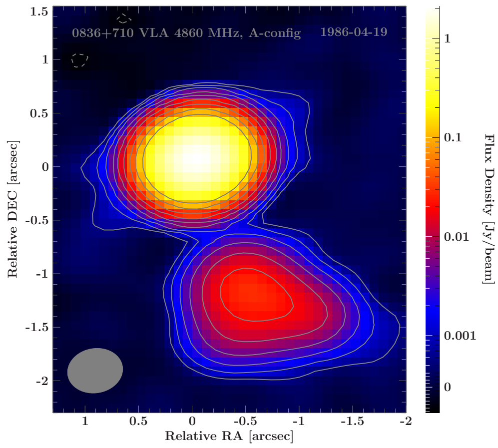

Figure 5.4.: VLA observation of *S5 0836+710* in A configuration at 4.86 GHz central observation frequency. The lowest contour level marks with a 3σ threshold. The contour levels are -0.52, 0.52, 1.0, 2.1, 4.2, 8.3, 17, 33, 66, 133 mJy/beam. The RMS is 0.173 mJy/beam. The beam size is $0.517'' \times 0.415''$ with a position angle of $-80.5°$.

EVN+MERLN

With the higher resolution the EVN+MERLIN data shows an extension going south of the bright core region shown in Figure 5.5. Considering VLBA data (Perucho et al. 2012a) this extension shows a jet. After about 1 arcsec where no flux is detected the previously mentioned region appears. In this data no bright hot spot is visible but still contains the triangular like structure with significant flux up to three contours.

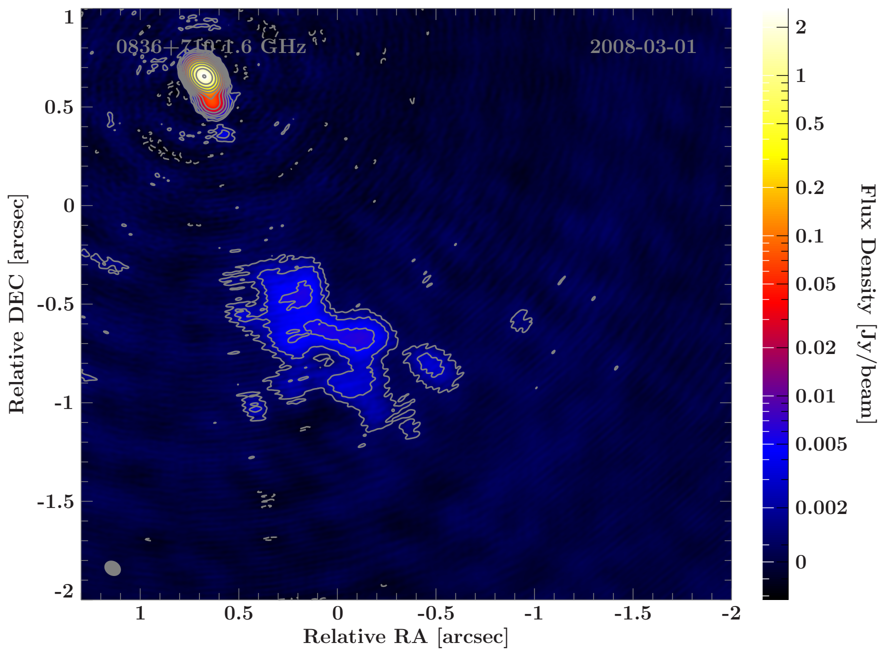

Figure 5.5.: EVN+MERLIN observation of *S5 0836+710* at 1.6 GHz central observtaion frequency. The lowest contour level marks with a 3σ threshold. The contour levels are -1.2, 1.2, 2.4, 4.9, 9.8, 20, 39, 78, 156, 313, 625, 1251, 2501 $^{\mathrm{mJy}}/_{\mathrm{beam}}$. The RMS is 0.407 $^{\mathrm{mJy}}/_{\mathrm{beam}}$. The beam size is $0.084'' \times 0.068''$ with a position angle of $57°$. Credit: Perucho et al. (2012a) availible at cdsarc.u-strasbg.fr (130.79.128.5) or via http://cdsarc.u-strasbg.fr/viz-bin/qcat?J/A+A/545/A65

Table 5.2.: Beam parameters for final images of *S5 0836+710* observed by LOFAR,VLA and EVN+MERLIN.

Central Frequency in GHz	Figure	Beam Size in arcsec	Position Angle in degree	Telescope
0.126	A.1a	0.493×0.343	-38.6	LOFAR
0.129	A.1b	0.485×0.337	-41.6	LOFAR
0.132	A.2a	0.459×0.321	-38.7	LOFAR
0.135	A.2b	0.495×0.313	-34.2	LOFAR
0.138	A.3a	0.526×0.312	-35.7	LOFAR
0.141	A.3b	0.494×0.298	-39.0	LOFAR
0.144	A.4a	0.468×0.287	-40.3	LOFAR
0.151	A.4b	0.408×0.286	-37.4	LOFAR
0.154	A.5a	0.428×0.307	-47.8	LOFAR
0.157	A.5b	0.414×0.308	-38.2	LOFAR
0.160	A.6	0.381×0.278	-38.2	LOFAR
8.4	A.6	0.517×0.415	-80.5	VLA
1.6	5.5	0.084×0.068	57	EVN+MERLIN

5.2. Flux measurements

S5 0836+710 was imaged with the international stations after the total flux was calculated by the core stations, using this information to adjust the visibilities of the international stations to match those. The hybrid imaging process can lead to slight flux changes. Also emission outside the FOV of the international stations but within the resolution limit of the core stations must be considered if present. With the remote stations we could ensure that there is none present, therefore the total flux received by the core stations is visible in total to the international stations. Figure 5.6 shows the mentioned small deviations between the total source flux for international stations (in Figure 5.6: VLBI source) and the core stations. Furthermore, the flux of the unresolved core component is shown (in Figure 5.6: VLBI core) which is scattering significantly more since these values highly depend on the model. This is obtained by the hybrid imaging process and is therefore expected to deviate stronger because each image was produced solely, meaning no transfer of information between images like windows for clean components.

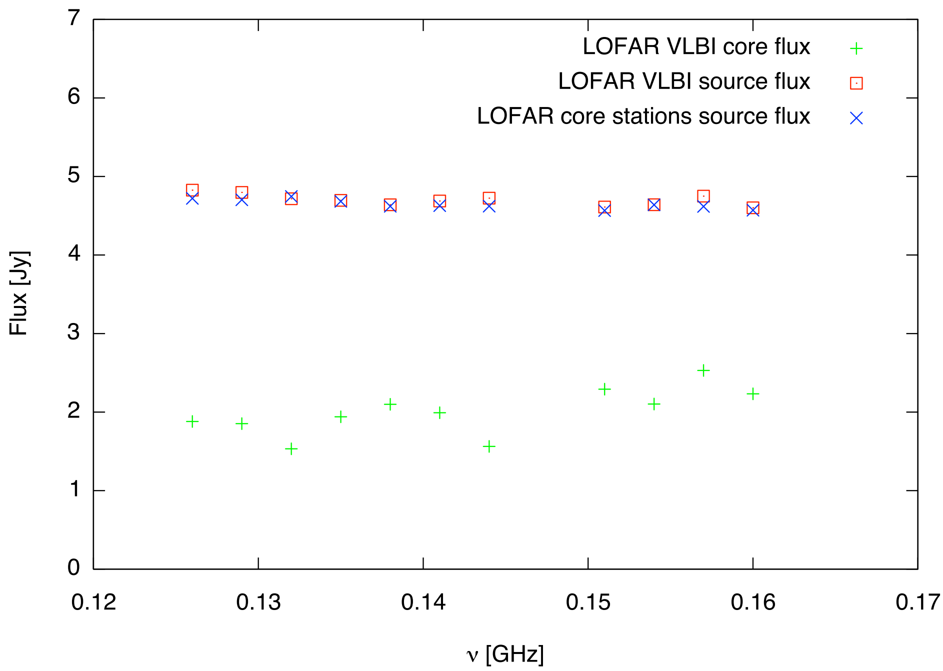

Figure 5.6.: Measured flux values in eleven bands of about 3 MHz bandwidth for the sources total flux observed by only LOFAR HBA core stations (blue cross), the calibrated total flux observed by the LOFAR HBA international stations (red box) and the flux of the unresolved core component seen by the LOFAR HBA international stations (green plus). Three bands in total were not evaluated due to insufficient data quality. One at the top end and low end of the frequencies each and one in between.

Confinement of uncertainties

While carrying on many calibration steps in different stages it is hard to end up with uncertainties given by the telescope on observation. The flux calibration is assumed to give sufficient flux values due to the radio observatory calibration, which is transfered to the international stations. Considering the rather small overall bandwidth (126 - 160 MHz) a linear spectrum can be assumed. The standard deviation to the linear fit provides a good estimate of the uncertainty of the total source flux measured by the international stations. The described linear fit is shown in Figure 5.7 with the fit-function:

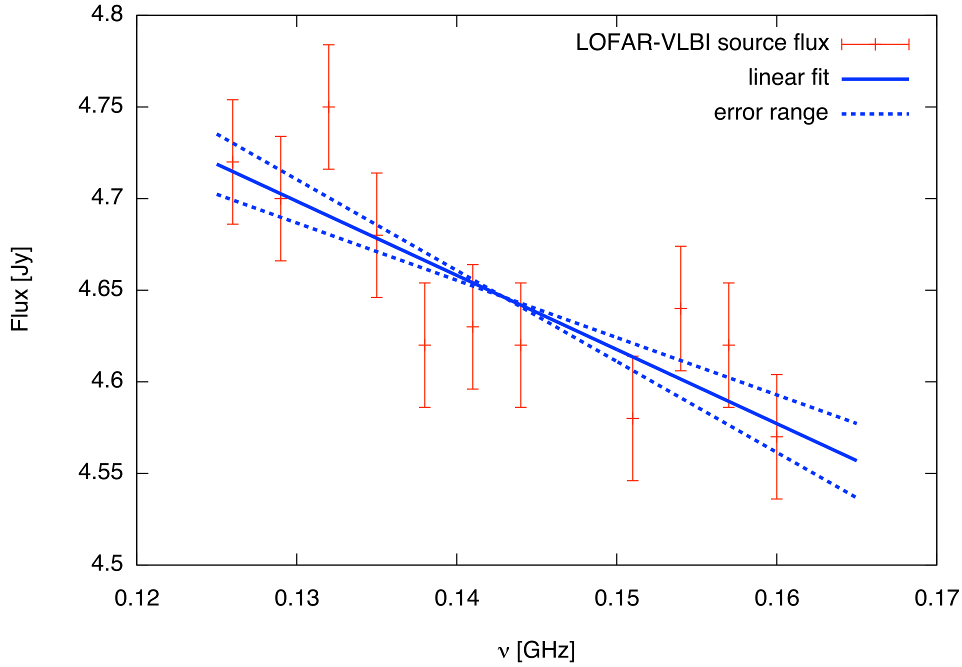

Figure 5.7.: The total source flux measured by the LOFAR HBA international stations for each final frequency band with a bandwidth of about 3 MHz. The values are modeled with a linear fit function (blue line) assuming to describe it sufficiently in the frequency range of about 50 MHz. The error bars are derived by the statistical scattering with respect to the fit, allowing to estimate the respective minimum and maximum slope (blue dashed lines). The model function is given in Equation 5.2.1.

$$F_{source}^{\mathrm{VLBI}} = -(3.8 \pm 0.9)\nu \, \frac{\mathrm{Jy}}{GHz} + (5.20 \pm 0.13)\mathrm{Jy} \; . \tag{5.2.1}$$

$F^{\mathrm{VLBI}}_{source}$ is the source flux in Jy and ν is the central frequency in GHz. The standard deviation is given as 0.0339624 Jy and therefore used as the uncertainty. The negative slope translating to a spectral index of -0.125 ± 0.028 is consistent assuming a steep spectrum for the extended emission though dominated by the flat spectrum core. The same argumentation is used to determine the other flux values uncertainties. Though the unresolved core flux is expected to have a flat spectrum and therefore a fit to a constant is used for this flux. The performed fit is shown in Figure 5.8 with the constant:

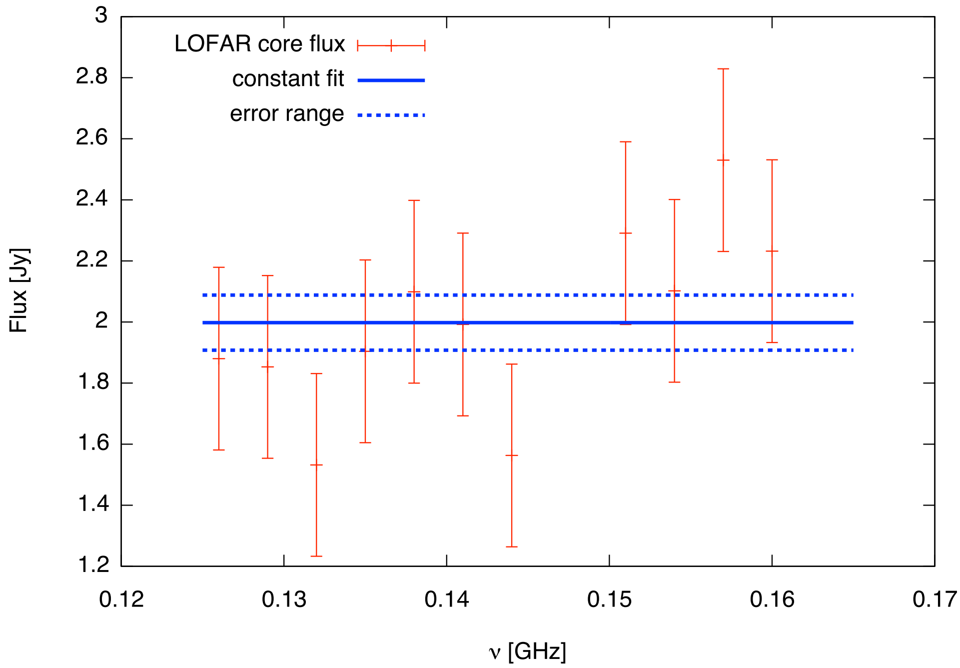

Figure 5.8.: The unresolved core component flux measured by the LOFAR HBA international stations for each final frequency band with a bandwidth of about 3 MHz. The values are modeled with a linear fit function (blue line) assuming to describe it sufficiently in the frequency range of about 50 MHz. The functions slope is set to the value 0, making the a priori assumption that the core flux has a flat spectrum. The error bars are derived by the statistical scattering with respect to the fit, allowing to estimate the respective minimum and maximum fitted flux (blue dashed lines). The model function is given in Equation 5.2.2.

$$F^{VLBI}_{\mathrm{core}} = (1.998 \pm 0.090)\ \mathrm{Jy}. \tag{5.2.2}$$

F^{VLBI}_{core} is the unresolved core component flux. The standard deviation for these values

is calculated as 0.29914 Jy and therefore used as uncertainty for these flux values. It has to be noted that the flux seems to increase with frequency which actually should not happen. A possible explanation is a random influence introduced through the modeling. Or an unlikely spectrum inversion due to absorption. Although regarding the scattering of the data values this can not be confirmed.
The extended emission around the unresolved core component is described with the linear fit function as depicted in Figure 5.9:

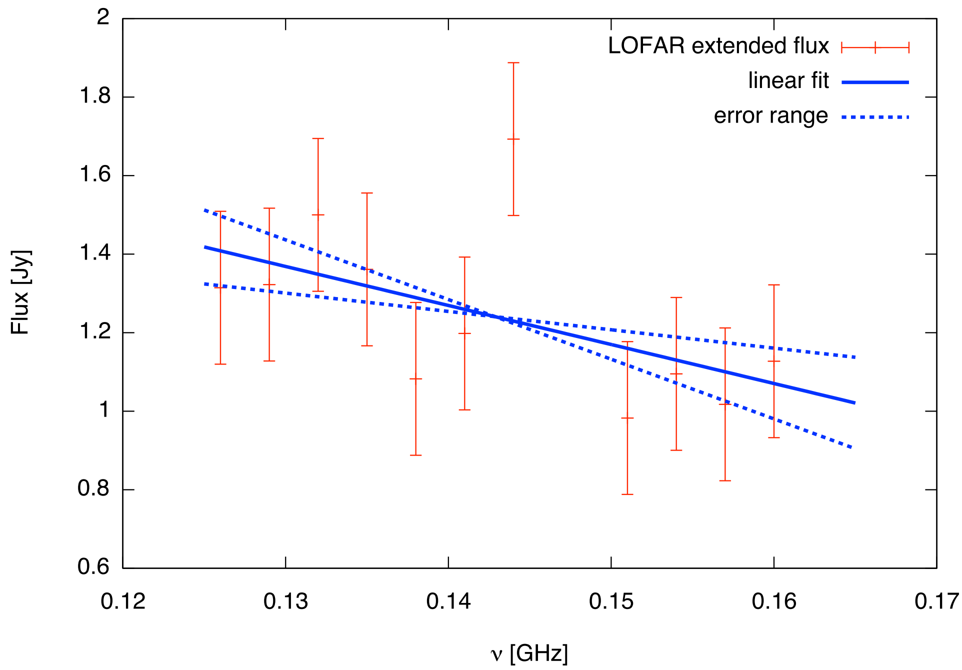

Figure 5.9.: The total extended flux around the unresolved core without the component in the south west, measured by the LOFAR HBA international stations for each final frequency band with a bandwidth of about 3 MHz. The values are modeled with a linear fit function (blue line) assuming to describe it sufficiently in the frequency range of about 50 MHz. The error bars are derived by the statistical scattering with respect to the fit, allowing to estimate the respective minimum and maximum slope (blue dashed lines). The model function is given in Equation 5.2.3.

$$F_{ext}^{VLBI} = -(9.9 \pm 5.3)\ \nu\ \frac{\mathrm{Jy}}{\mathrm{GHz}} + (2.66 \pm 0.75)\ Jy. \tag{5.2.3}$$

F_{ext}^{VLBI} describes the extended flux around the unresolved core component in Jy and ν the central frequency in GHz. The resulting standard deviation of 0.19459 Jy is used as the uncertainty as described above. The shown flux follows an expected decrease in frequency translating to a spectral index of -1.07 ± 0.62.

The flux of the component in the south west is described with the following linear function and shown in Figure 5.10:

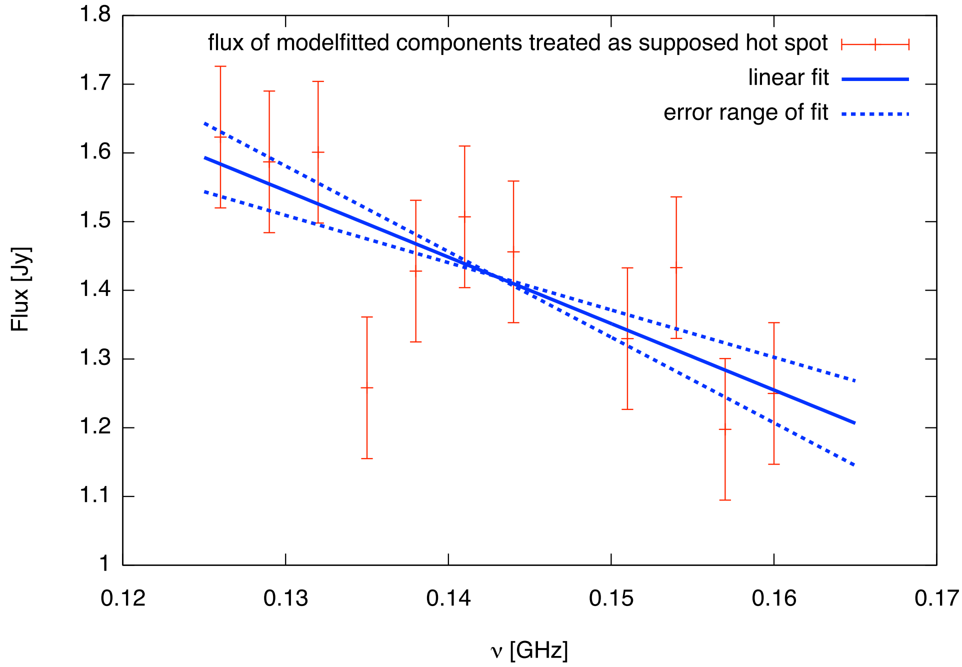

Figure 5.10.: The total flux of the component in the south west measured by the LOFAR HBA international stations for each final frequency band with a bandwidth of about 3 MHz. The values are modeled with a linear fit function (blue line) assuming to describe it sufficiently in the frequency range of about 50 MHz. The error bars are derived by the statistical scattering with respect to the fit, allowing to estimate the respective minimum and maximum slope (blue dashed lines). The model function is given in Equation 5.2.4.

$$F_{comp}^{VLBI} = -(9.7 \pm 2.8)\ \nu\ \frac{\mathrm{Jy}}{\mathrm{GHz}} + (2.80 \pm 0.40)\ Jy. \tag{5.2.4}$$

F_{comp}^{VLBI} describes the total flux of the component in the south west in Jy and ν the central frequency in GHz. The resulting standard deviation of 0.103036 Jy is used to be the uncertainty as described above. The shown flux follows an expected decrease in frequency. The shown flux follows an expected decrease in frequency translating to a spectral index of -0.97 ± 0.28.

Measurement consistency with other observations

The detected flux by other observations given in NED[1] combined with these measurements shown in Figure 5.11 depict a very good agreement. The core flux measurements, seen as blue crosses, match to the high frequency measurements as one would expect because there the field of view is smaller, detecting rather the core regions. Additionally the steep spectrum regions - which is everything but the core - decrease in luminosity and therefore the core becomes more dominant while also not becoming brighter. Comparing the total flux for international station only and core station only barely any difference is visible regarding the surrounding scattering of other observations. Furthermore the slope of the LOFAR data seems to match the overall slope of the long wavelength observations. This leads to the conclusion that the total flux calibration described here yields excellent amplitude calibrations. The flux distribution within the morphology though has to be investigated further. A possibility could be to create images without international stations but only core and remote stations, offering a precise low resolution model to calibrate further the international core stations. In the presented data we cover this with an adequate uncertainty estimation provided by the scattering. The obtained results yield fluxes and spectral indexes well within the expectations.

[1] http://ned.ipac.caltech.edu/

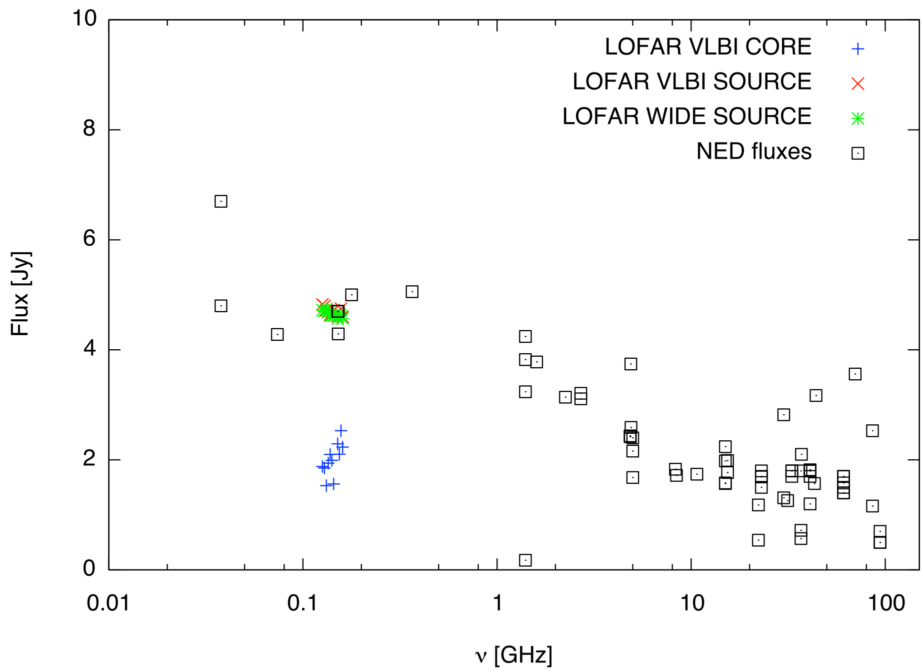

Figure 5.11.: Total radio flux of *S5 0836+710* measured by multiple telescopes. The measurements did not take place simultaneously but are rather a collection of all published measurements performed on this source. The black boxes are measurements obtained through **N**ASA/IPAC **E**xtragalactic **D**atabase (NED). The other marks are LOFAR HBA measurments with international stations of the unresolved core (blue plus), the total source flux (red cross) and with measurements with core stations of the total source flux (green asterisks) in eleven frequency bands.

5.3. Spectral properties

The obtained images can be used to create spectral maps between two images of certain bands or with another telescope e.g. the VLA measurement. However, the close central frequencies of the LOFAR images with respective high uncertainties create spectral maps with extreme values, exceeding the physical reasonable regime. Therefore LOFAR-LOFAR spectral maps have to be considered carefully and only in context with physically interpretable spectral maps. A possibility that could obtain interpretable LOFAR-LOFAR spectral maps is averaging at least three images at the high and low end of the frequency coverage and create a spectral map of those. This is currently not possible with present software and must be developed. Another way to handle that problem is to model fit each pixel over all images to a powerlaw and determine the spectral index in that region this way. Also for this approach no software is currently available. Therefore we create a spectral map of the highest ($\nu_{\text{central}} = 160\,\text{MHz}$) and lowest ($\nu_{\text{central}} = 126\,\text{MHz}$) frequency band (see Figure 5.13) to have the least impact of flux uncertainty on the index. See Figure 5.12 for a representative spectral map between the VLA and LOFAR at 160 MHz central frequency (find all spectral maps in Figure B.1a to B.6).

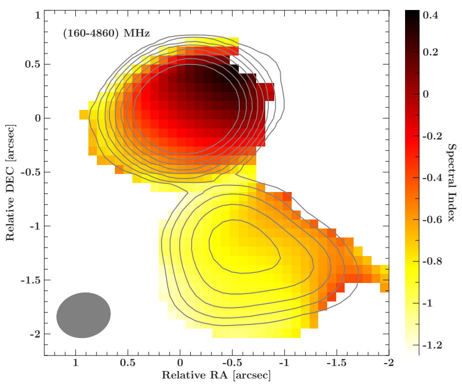

Figure 5.12.: Exemplary spectral map between the LOFAR HBA international stations' image with a mid frequency of 160 MHz and the VLA image with a mid frequency of 4.86 GHz. Pixel values below 3σ for LOFAR or VLA are shown white. The contour levels are added from the VLA image with −0.52, 0.52, 1.0, 2.1, 4.2, 8.3, 17, 33, 66, 133 mJy/beam. The beam size is $0.517'' \times 0.415''$ with a position angle of $-80.5°$. Find all spectral maps in the appendix B.

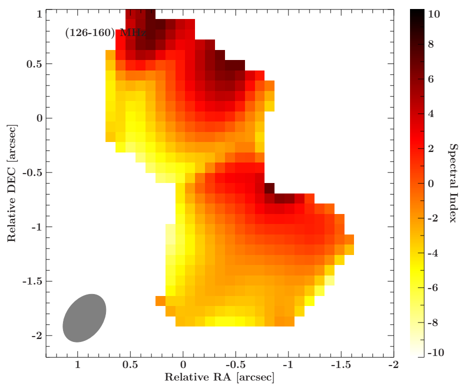

Figure 5.13.: Spectral map between the LOFAR HBA international stations' images with mid frequency of 126 MHz and 160 MHz. Pixel values below 3σ for any of the image are shown white. The beam size is $0.493'' \times 0.343''$ with a position angle of $-38.6°$.

As seen in Figure 5.12 and 5.13, the central component shows a rather flat spectrum as we expect by a boosted emission coming from a jet pointing in a small angle to our line of sight. In the north west of the core, a region with a spectral index of up to about 0.4 can be found in all images which is within the uncertainties still considered to be flat. The surrounding extended emission apart from that tends to have a steep spectrum with a spectral index around -0.5 down to -1.0 consistent with unbeamed emission regions. Likewise the component in the south west shows in general a steep spectrum with the spectral index around -1.0, as expected for a unbeamed emission region which can certainly be a lobe like structure from this point of view. It has to be mentioned though that in the north west part of this region the spectral index seems to tend to change to a flat spectrum. This tendency is visible in all images but can be either an influence coming from the VLA image or a boundary effect. Since these parts show lower emission regions as indicated by the VLA contours, they would also be affected relatively higher due to deviations caused by uncertainty. Both explanations can take place in parallel.

5.4. Parameter analysis

Assuming the south west component is a hot spot this object would be identified as a rotated FR II AGN after the unification model. Calculating the intrinsic luminosity using equation 2.3.1 with the mean flux of the source subtracted with the core flux we obtain:

$$L_{\text{ext}} = 1.721 \times 10^{28}\,\frac{\text{W}}{\text{Hz}} \tag{5.4.1}$$

$$\log(L_{\text{ext}}) = 28.4 \tag{5.4.2}$$

The luminosity and morphology show characteristics of a rotated FR II AGN with a hot spot where the luminosity is typical for that class.
As introduced in Burd (2017), the inclination angle and linear size can be estimated by observations of Parma et al. (1987) and Jeyakumar & Saikia (2000). Modeling the supposed hot spot in all images we use the averaged hot spot component parameters to calculate the projected opening angle as:

$$\zeta' = 12.8^\circ \tag{5.4.3}$$

Which leads with respect to the most probable ($\zeta_{\text{prop}} = 2.5^\circ$) and minimum ($\zeta_{\text{min}} = 1.4^\circ$) de-projected jet opening angle to the most probable (θ_{prop}) and minimum (θ_{min}) inclination angle of:

$$\theta_{\text{prop}} = 11.2^\circ \tag{5.4.4}$$
$$\theta_{\text{min}} = 6.24^\circ \tag{5.4.5}$$

Adopting a linear size of 8.08 $^{\text{pc}}/_{\text{mas}}$ a projected, Lorentz contracted jet size of 10.9 kpc is measured. Assuming the minimum inclination angle this yields a de-projected linear jet size of about 109 kpc. Respectively the most probable inclination angle results in a de-projected linear jet size of 61 kpc. Establishing an upper limit for the linear sizes of AGN from Lara et al. (2001), an upper limit for the supposed hot-spots Lorentz factor can be calculated as (using $s_{\text{prop}} = 1010$ kpc, $s_{\text{max}} = 3739$ kpc after Burd 2017):

Table 5.3.: Calculated Lorentz factors (a) and the resulting jet speeds in c (b) based on the maximal and most probable jet size from Lara et al. (2001) and the minimal and most probable inclination angle.

	θ_{min}	θ_{prop}
s_{prop}	16.5	9.3
s_{max}	61.3	34.3

(a) Lorentz factors

	θ_{min}	θ_{prop}
s_{prop}	0.97	0.94
s_{max}	0.99	0.99

(b) Jet speeds in c

Also these Lorentz factors can be used to calculate resulting jet speeds which are also shown in this table. These values provide only upper limits so far though it has to be considered that the statistical values were elaborated with redshifts for up to $z \approx 1$ therefore we can expect the true jet size to be smaller because there was less time for the presumable hot spot to reach out and evolve. This would lead to lower Lorentz factors and consecutively to lower jet speeds. Still, the calculated jet speeds are in agreement to be in the same order as high relativistic jets emerging from the core region (e.g. Krolik 1999). It actually is expected to slow down, depending on internal pressure instability and any matter in the crossection slowing down the jet. These cases also are in agreement with these values, since we regard those as upper limits.
The presumed hot spot sizes in these images show diameters of about 2.5 kpc. Regarding Jeyakumar & Saikia (2000) who analyzed larger FR II sources, they could show that tenth of kpc hot-spot sizes as major axes can be reached. Hence our dataset does not show any contradiction to a hot-spot scenario in this regard.

5.5. Discussion

The images, produced with the aforementioned pipeline are consistent within the analyzed LOFAR frequency bands. Furthermore in the context of a C-band VLA image and a EVN+MERLIN image at 1.6 GHz are consistent with respect to the morphology. The measured fluxes in the different regions show self consistent values throughout the full frequency range with well estimated uncertainties. The remaining fluctuations can be explained by the first approximate flux calibration for the international stations. This is currently estimated for all international stations and remote stations respectively time-independent. One could improve this to calculate station based correction factors instead, which have to remain time-independent.
Comparing the flux results with multiple other measurements obtained through NED we see a flat spectrum core and steep spectrum extended emission around the core and a steep spectrum component in the south west. The steepness in both cases with a spectral index of about -1 fits well for a unbeamed emission region as we expected. Hence, we can isolate the core flux from the extended flux with sufficient accuracy for a source having a redshift of about 2 from with a total flux of about 5 Jy. This capability was predicted by the proposals for *Blazar-Jet Kinetic Power from Low-Frequency Radio Observations* (PI:Trüstedt) in the observation cycles 3, 4 and 5. This pipeline prepares these data to a quality, demanded by these projects to be feasible.
The spatial spectral index distribution between the LOFAR bands and the C-band VLA image show the flat spectrum in the core region and the steep spectrum in the extended emission region. The spectral maps between the highest and lowest LOFAR frequency bands feature the same trends as in the LOFAR-VLA spectral maps but the values for the spectral indices are unphysical. This is the result of the frequency bands being to close, resulting with relatively high flux uncertainties per pixel in strong fluctuations in the spectral index values. Improving further the flux calibration will lead to better results. Also the general approach to create spectral maps should be changed. Due to the many spectral information, it is possible to model pixel wise a power law to calculate a spectral index. This should handle fluctuations much better than just picking two frequency bands for the calculation. Another way would be to average the upper half and lower half of the images to a wider frequency band and reduce the fluctuations that way.
The interpretation of the component in the south west holds several possibilities. The low resolution images by LOFAR and the VLA can interpret it as a hot spot. But the high resolution findings of Perucho et al. (2012b) basically wave this scenario with a EVN+MERLIN image.
The currently favored and presented scenario by Perucho et al. (2012b) is a disrupted jet due to KH instabilities. A current driven disruption is described to be unlikely due to the particle domination in jets rather than magnetic domination. In this scenario a disrupted remain of the jet travels out without any medium interaction until

it terminates in a shock with the IGM. This shock front would be sharp with resulting spectral gradients. These gradients would occur perpendicular to the shock front. To test this, at least two images at different frequencies with the resolution of at least the EVN+MERLIN image are needed. Additionally it is recommended not to go too high in frequency due to the steep spectrum of this region, which gets much fainter with increasing frequency. LOFAR does not provide these possibilities, neither does the VLA. A significant gradient can not be seen although the component in the south west seems to tend to show a flatter spectrum in the north west.

Another possibility could be a scenario where the south west component is a remain of an older lobe fed by the jet. A disruptive or interruptive event could have destroyed the jet, suppressing further supply of hot plasma. The measured expansion (de-projected of up to 109 kpc) is well within observed jet sizes. A sharp spectral gradient would not be expected in this scenario.

Due to our findings we can say that a hot spot scenario is unlikely, as well as a jet disruption, due to current driven instabilities. The data at this point favors either the disruption of the jet due to KH instabilities with a outflowing uncollimated material terminating in a shock with the IGM or a remain lobe from a previous jet that has been disrupted or interrupted.

6. Summary and Outlook

Evaluating the observational data, a consistent core flux of (1.998 ± 0.090) Jy matching to high resolution GHz measurements can be measured. Expecting a boosted emission in the unresolved core, the flat spectrum can be verified with the flux measurements in the LOFAR frequency bands and the VLA C-band data. The averaged total measured flux of about 4.6 Jy also matches to other flux measurements obtained through NED. Modeling the flux values of the extended emission around the core region, yields a spectral index of -1.07 ± 0.62, consistent with deboosted emission. Alike the spectral index of the component in the south west with a modeled spectral index of -0.97 ± 0.28. The spatial distribution of the spectral indices the spectral maps shows consistent structure and values with LOFAR-VLA maps. The spectral index map between the lowest and highest LOFAR frequency band shows familiar structure as seen in the others, but with unphysical values. These are created due to the relatively high flux uncertainties with respect to close frequency bands. Improvements with a higher SNR will yield improvements in this respect. Also it should be considered to create a procedure that fits a power law to each pixel position through all frequency bands, calculating a more robust spectral index map.

Following the steps from Burd (2017) on *S5 0836+710* in order to classify the source after the unification model. The intrinsic luminosity of 1.721×10^{28}W/Hz matches a rotated FR II AGN therefore the analysis was performed on the FR II sample. The obtained jet speeds for various cases match with Lorentz factors between 9.3 and 61.3 and therefore resulting jet speeds of 0.97 c to 0.99 c to a FR II scenario with a hot spot in the south west. Also the hot spot size of about 2.5 kpc is well within other observed hot spots. Solely the observation with EVN+MERLIN show that the morphology shows no signs of a hot spot. The proposed scenario by Perucho et al. (2012b) claims this to be KH instability triggered disruption of the jet, which interacts further out with the IGM. The LOFAR data does neither prove nor dismiss this scenario.

Showing also the robustness of the processing pipeline in this thesis, this provides a profound basis to analyze a bigger sample and create a significant statistic to address the questions related to the unification model (Urry & Padovani 1995). Also technical more demanding data like in the case of the proposal project *CMB-Quenching of High-z Blazars* (PI: Trüstedt) observed in the LOFAR cycle 4 can be analyzed with this procedure.

The resulting performance of the calibration pipeline, performed on the observation of *S5 0836+710*, is fully parallelized at this stage and scalable with processing cores and RAM up to the imaging part. Only few frequency bands (3 out of 14) had to be discarded due to the poor data, mainly because of issues that are too strong due to the bandwidth profile. The core and international stations could be fully calibrated in flux and phase delay. The remote stations were not flux calibrated because there was no need for it.

Appendices

A. Final high resolution images of *S5 0836+710*

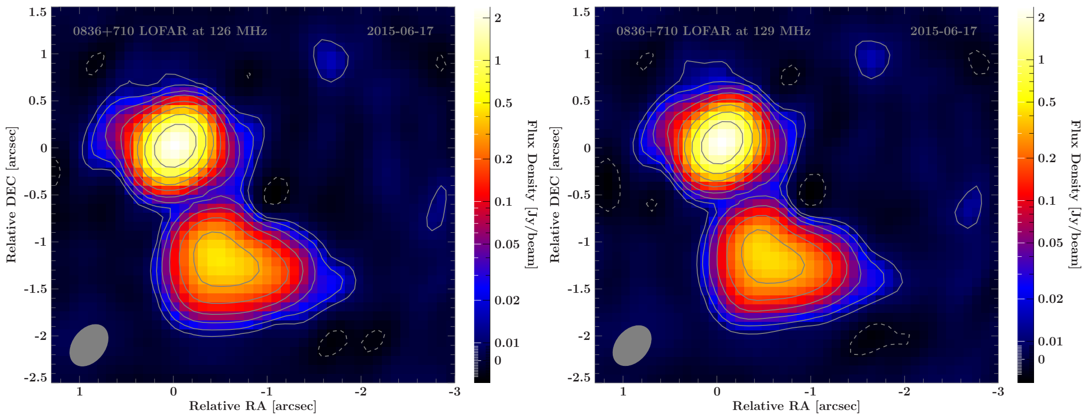

(a) **(b)**

Figure A.1.: LOFAR HBA measurement of *S5 0836+710* with international stations with a bandwidth of about 3 MHz and a central frequency of 126 MHz (a) and 129 MHz. The lowest contour level marks with a 3σ threshold. The contour levels are -0.031, 0.031, 0.061, 0.12, 0.24, 0.49, 0.98, 2.0, 3.9, 7.8 Jy/beam. The RMS is 0.0102 Jy/beam. The beam size is $0.493'' \times 0.343''$ with a position angle of $-38.6°$ (a) and $0.485'' \times 0.337''$ with a position angle of $-41.6°$ (b).

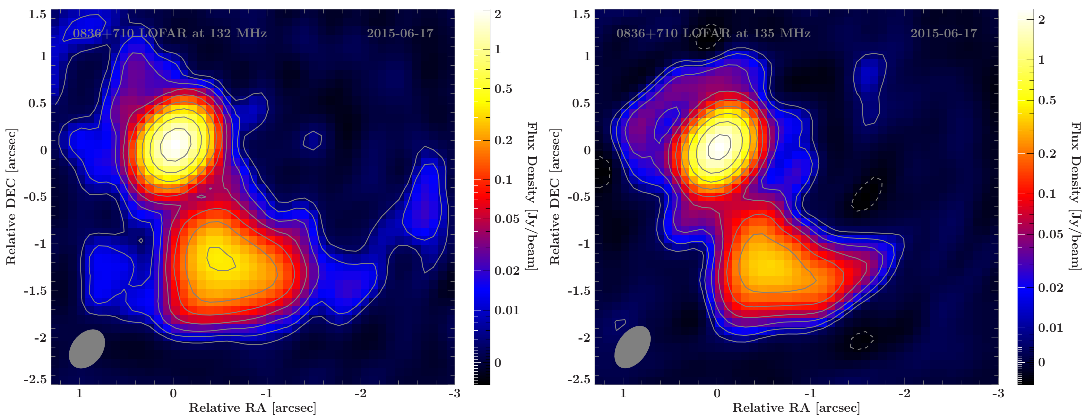

(a) **(b)**

Figure A.2.: LOFAR HBA measurement of *S5 0836+710* with international stations with a bandwidth of about 3 MHz and a central frequency of 132 MHz (a) and 135 MHz. The lowest contour level marks with a 3σ threshold. The contour levels are -0.031, 0.031, 0.061, 0.12, 0.24, 0.49, 0.98, 2.0, 3.9, 7.8 Jy/beam. The RMS is 0.0102 Jy/beam. The beam size is $0.459'' \times 0.321''$ with a position angle of $-38.7°$ (a) and $0.495'' \times 0.313''$ with a position angle of $-34.2°$ (b).

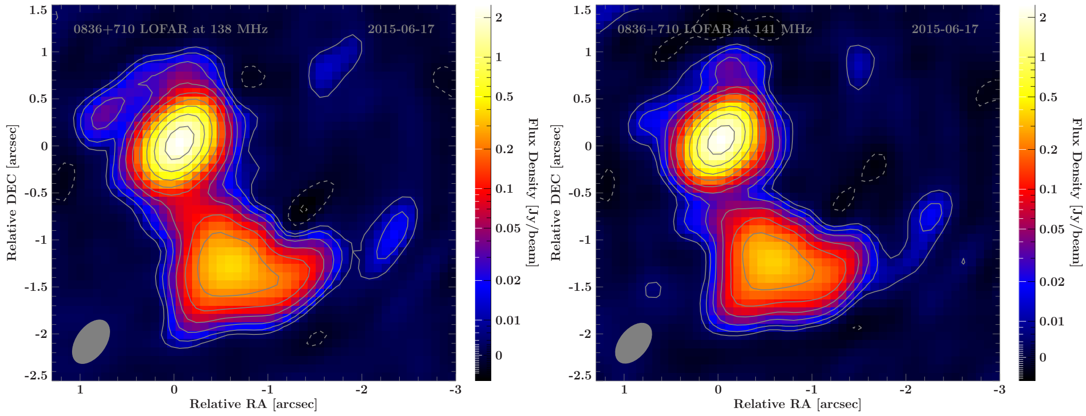

(a) (b)

Figure A.3.: LOFAR HBA measurement of *S5 0836+710* with international stations with a bandwidth of about 3 MHz and a central frequency of 138 MHz (a) and 141 MHz. The lowest contour level marks with a 3σ threshold. The contour levels are -0.031, 0.031, 0.061, 0.12, 0.24, 0.49, 0.98, 2.0, 3.9, 7.8 Jy/beam. The RMS is 0.0102 Jy/beam. The beam size is $0.526'' \times 0.312''$ with a position angle of $-35.7°$ (a) and $0.494'' \times 0.298''$ with a position angle of $-39.0°$ (b).

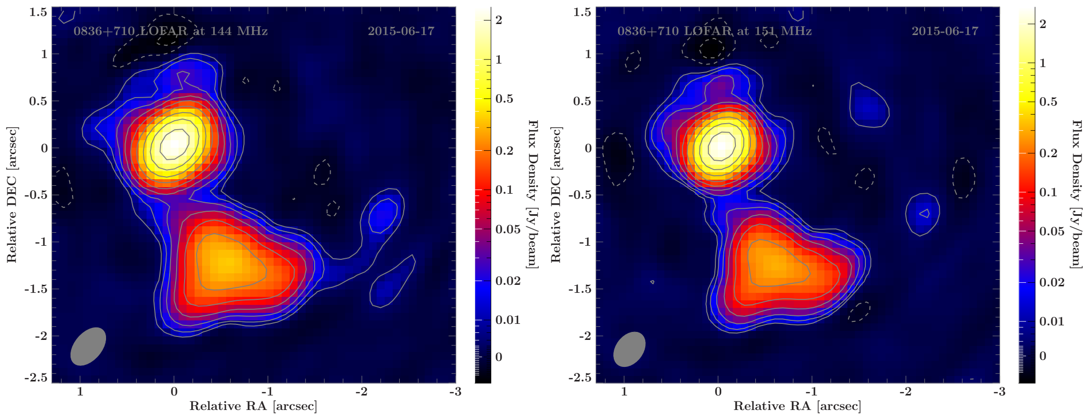

(a) (b)

Figure A.4.: LOFAR HBA measurement of *S5 0836+710* with international stations with a bandwidth of about 3 MHz and a central frequency of 144 MHz (a) and 151 MHz. The lowest contour level marks with a 3σ threshold. The contour levels are -0.031, 0.031, 0.061, 0.12, 0.24, 0.49, 0.98, 2.0, 3.9, 7.8 Jy/beam. The RMS is 0.0102 Jy/beam. The beam size is $0.468'' \times 0.287''$ with a position angle of $-40.3°$ (a) and $0.408'' \times 0.286''$ with a position angle of $-37.4°$ (b).

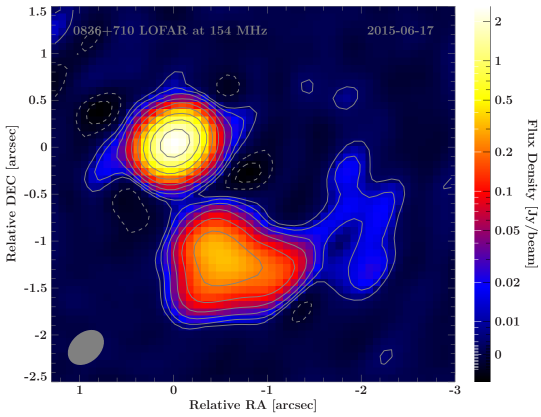

(a)

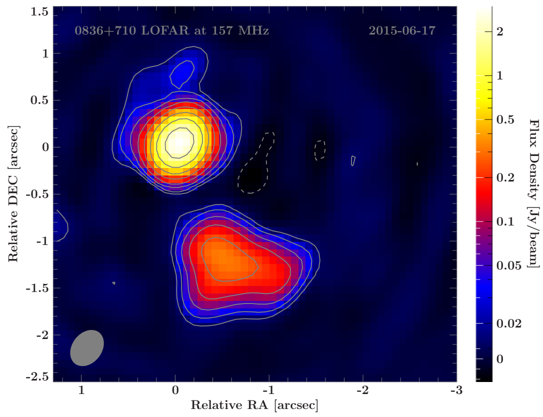

(b)

Figure A.5.: LOFAR HBA measurement of *S5 0836+710* with international stations with a bandwidth of about 3 MHz and a central frequency of 154 MHz (a) and 157 MHz. The lowest contour level marks with a 3σ threshold. The contour levels are -0.031, 0.031, 0.061, 0.12, 0.24, 0.49, 0.98, 2.0, 3.9, 7.8 Jy/beam. The RMS is 0.0102 Jy/beam. The beam size is $0.428'' \times 0.307''$ with a position angle of $-47.8°$ (a) and $0.414'' \times 0.308''$ with a position angle of $-38.2°$ (b).

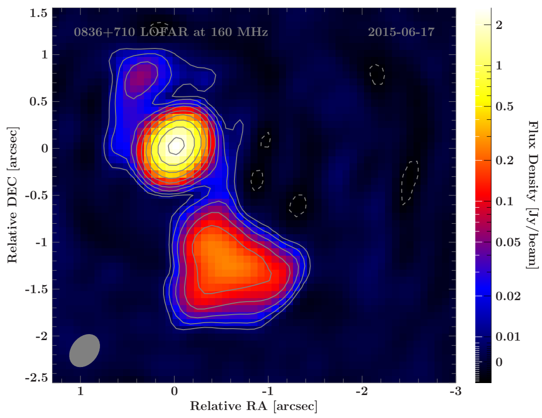

Figure A.6.: LOFAR HBA measurement of *S5 0836+710* with international stations with a bandwidth of about 3 MHz and a central frequency of 160 MHz. The lowest contour level marks with a 3σ threshold. The contour levels are -0.031, 0.031, 0.061, 0.12, 0.24, 0.49, 0.98, 2.0, 3.9, 7.8 Jy/beam. The RMS is 0.0102 Jy/beam. The beam size is $0.381'' \times 0.278''$ with a position angle of $-38.2°$.

B. Spectral maps of *S5 0836+710*

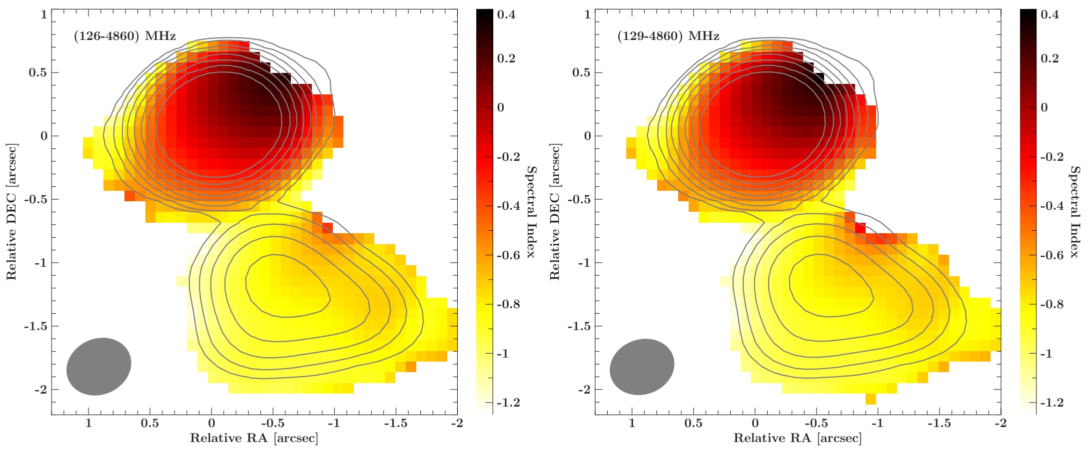

(a) **(b)**

Figure B.1.: Spectral map between the LOFAR HBA international stations' image with a mid frequency of 126 MHz (a), 129 MHz (b) and the VLA image with a mid frequency of 4.86 GHz. Pixel values below 3σ for LOFAR or VLA are shown white. The contour levels are added from the VLA image with −0.52, 0.52, 1.0, 2.1, 4.2, 8.3, 17, 33, 66, 133 $^{\mathrm{mJy}}/_{\mathrm{beam}}$. The beam size is $0.517'' \times 0.415''$ with a position angle of $-80.5°$.

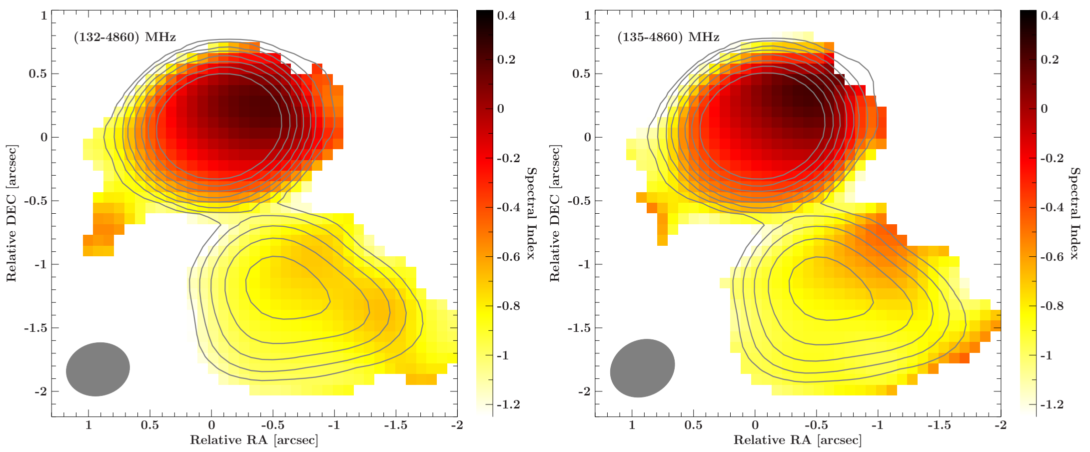

(a) **(b)**

Figure B.2.: Spectral map between the LOFAR HBA international stations' image with a mid frequency of 132 MHz (a), 135 MHz (b) and the VLA image with a mid frequency of 4.86 GHz. Pixel values below 3σ for LOFAR or VLA are shown white. The contour levels are added from the VLA image with −0.52, 0.52, 1.0, 2.1, 4.2, 8.3, 17, 33, 66, 133 $^{\mathrm{mJy}}/_{\mathrm{beam}}$. The beam size is $0.517'' \times 0.415''$ with a position angle of $-80.5°$.

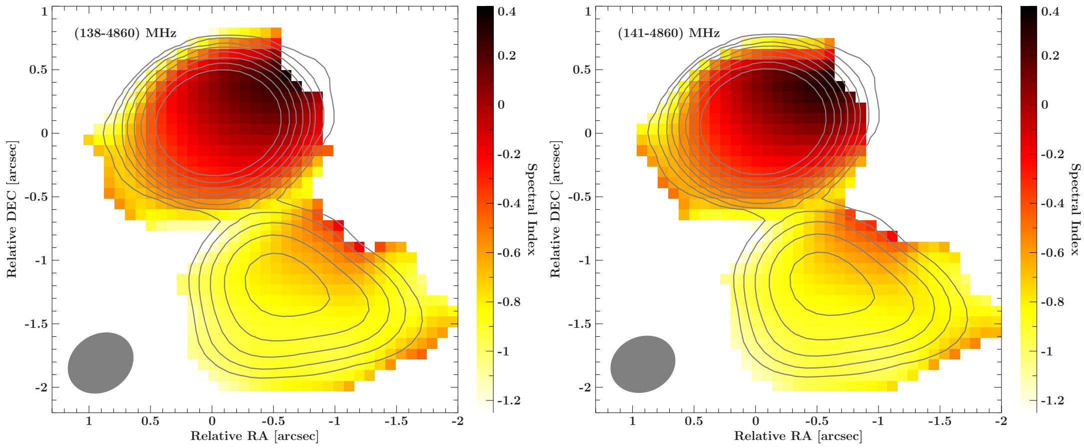

(a) **(b)**

Figure B.3.: Spectral map between the LOFAR HBA international stations' image with a mid frequency of 138 MHz (a), 141 MHz (b) and the VLA image with a mid frequency of 4.86 GHz. Pixel values below 3σ for LOFAR or VLA are shown white. The contour levels are added from the VLA image with -0.52, 0.52, 1.0, 2.1, 4.2, 8.3, 17, 33, 66, 133 $^{\mathrm{mJy}}/_{\mathrm{beam}}$. The beam size is $0.517'' \times 0.415''$ with a position angle of $-80.5°$.

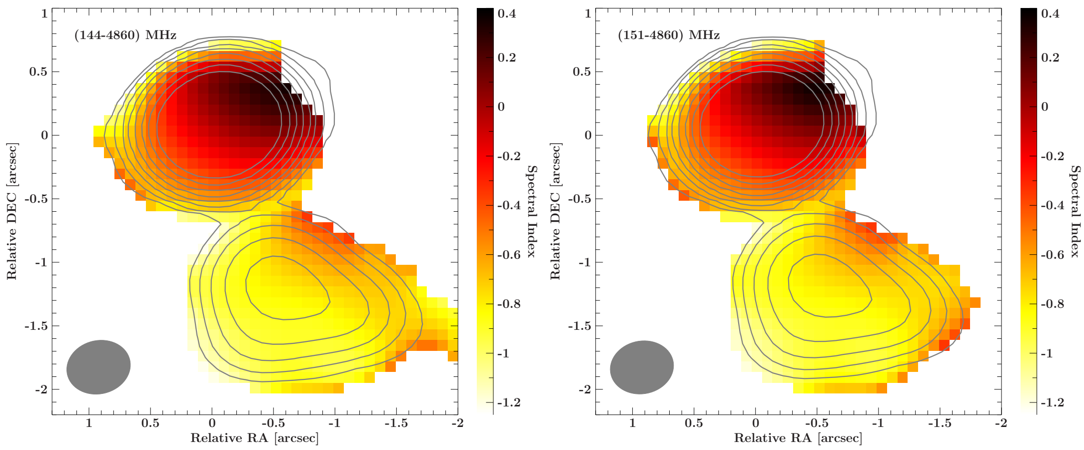

(a) **(b)**

Figure B.4.: Spectral map between the LOFAR HBA international stations' image with a mid frequency of 144 MHz (a), 151 MHz (b) and the VLA image with a mid frequency of 4.86 GHz. Pixel values below 3σ for LOFAR or VLA are shown white. The contour levels are added from the VLA image with -0.52, 0.52, 1.0, 2.1, 4.2, 8.3, 17, 33, 66, 133 $^{\mathrm{mJy}}/_{\mathrm{beam}}$. The beam size is $0.517'' \times 0.415''$ with a position angle of $-80.5°$.

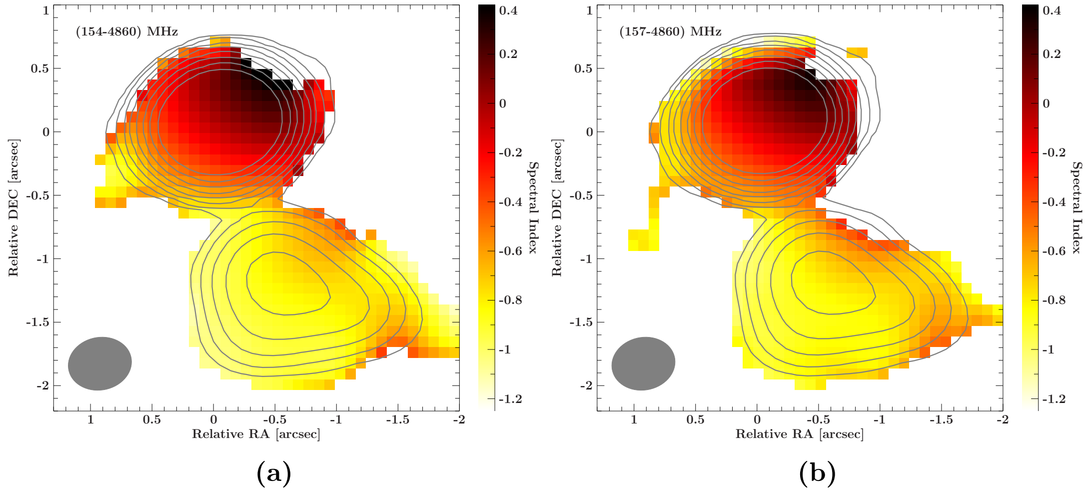

Figure B.5.: Spectral map between the LOFAR HBA international stations' image with a mid frequency of154 MHz (a), 157 MHz (b) and the VLA image with a mid frequency of 4.86 GHz. Pixel values below 3σ for LOFAR or VLA are shown white. The contour levels are added from the VLA image with −0.52, 0.52, 1.0, 2.1, 4.2, 8.3, 17, 33, 66, 133 mJy/beam. The beam size is $0.517'' \times 0.415''$ with a position angle of $-80.5°$.

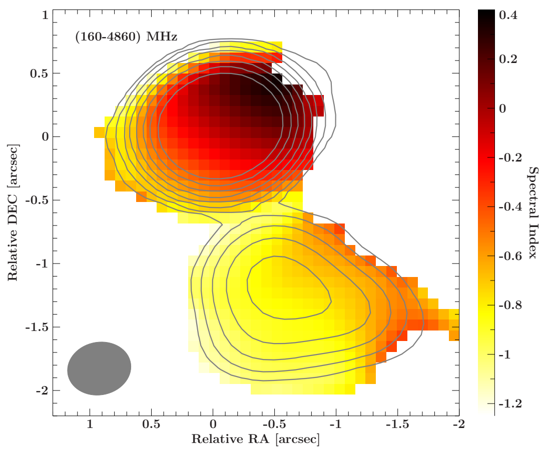

Figure B.6.: Spectral map between the LOFAR HBA international stations' image with a mid frequency of 160 MHz and the VLA image with a mid frequency of 4.86 GHz. Pixel values below 3σ for LOFAR or VLA are shown white. The contour levels are added from the VLA image with −0.52, 0.52, 1.0, 2.1, 4.2, 8.3, 17, 33, 66, 133 mJy/beam. The beam size is $0.517'' \times 0.415''$ with a position angle of $-80.5°$.

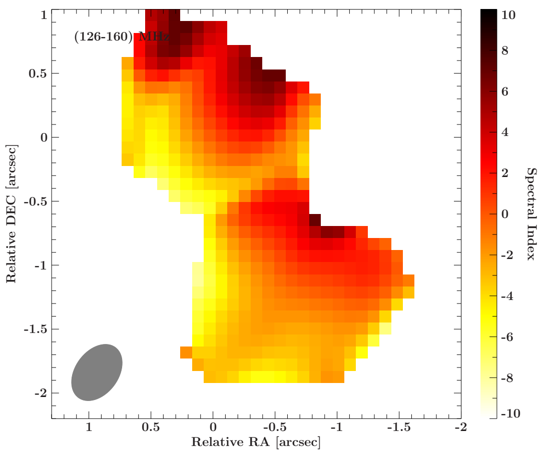

Figure B.7.: Spectral map between the LOFAR HBA international stations' images with mid frequency of 126 MHz and 160 MHz. Pixel values below 3σ for any of the image are shown white. The beam size is $0.493'' \times 0.343''$ with a position angle of $-38.6°$.

C. Pipeline scripts

Bash scripts

Listing C.1: Parallelized flux calibration for international and remote stations.

```
#!/bin/bash

ncores=12
nthreads=2

processes=$(($ncores * $nthreads))

intantmin=48
intantmax=56

notintmin=1
notintmax=47

refant=57

path="/scratch/DATA1/LC4/26/preampfix/0224+671/"
name="0224+671-BAND"

nextout="/scratch/DATA1/LC4/26/preampfix/224+671/lbfixed/"




array=($(ls ${path}${name}*))
#echo ${array[2]}
arr_len=${#array[@]}
#echo $arr_len

counter=0

for i in $(seq 0 ${processes} ${arr_len})
do
  for j in $(seq 0 ${processes})
  do
    if [$counter -lt $arr_len]
    then
```

```
    echo ${array[$((i+j))]}
    python correct_LB.py ${array[$((i+j))]} $intantmin $intantmax $notintmin $notintmax $refant $nextout $name$counter.FITS &
    fi
  counter=$((counter+1))
  sleep 1
  done
  wait

done
```

Listing C.2: Collective script for NDPPP steps.

```
#!/bin/bash

target_path="/scratch/DATA1/LC4/26/unpacked/"
target="L346078_SB"
work="/scratch/WORK/patchline/lhd01/"
work_tmp="${work}tmp/"
output_path="/scratch/DATA1/LC4/26/preampfix/"
output="0836+710-BAND"


rm -rf ${work_tmp}*
for i in $(seq 0 230)
do
NDPPP ${work}parsets/tiedstation.parset msin=${target_path}${target}$(printf '%03d' $i)_uv.dppp.MS msout=${work_tmp}${target}$(printf '%03d' $i)_uv.ts.MS
done

counter=0

for i in $(seq 2 16 227)
do
list="";
        for j in $(seq 0 14)
        do
        list="${list} ${work_tmp}${target}"$(printf "%03d" $((i+j)))"_uv.ts.MS,"
        done
list="${list} ${work_tmp}${target}"$(printf "%03d" $((i+15)))"_uv.ts.MS"
NDPPP ${work}parsets/datasets.parset msin="[$list]" msout="${work_tmp}${output}${counter}.MS"
taql "update ${work_tmp}${output}${counter}.MS set DATA = mscal.stokes(DATA,'circ')"
taql "update ${work_tmp}${output}${counter}.MS/POLARIZATION set CORR\_TYPE=[5,6,7,8]"
taql "update ${work_tmp}${output}${counter}.MS SET FLAG=T where isnan(UVW[0])"
```

```
ms2uvfits in="${work_tmp}${output}${counter}.MS" out="${output_path}${
    output}${counter}.FITS" writesyscal=False
counter=$((counter+1))
done
```

Parset files

Listing C.3: Parameter file to form superterp.

```
msin.baseline=
msin.blrange=[]
msin.corrtype=
msin.datacolumn=DATA
msin.forceautoweight=false
msin.missingdata=false
msin.nchan=nchan
msin.orderms=false
msin.sort=false
msin.startchan=0
msin.useflag=true
msout.overwrite=false
msout.tilenchan=8
msout.tilesize=1024
msout.vdsdir=A
msout.writefullresflag=true

steps=[filter1 ,stationadder , filter2 ]

filter2.baseline="!CS00[2-7]*&&*"
filter2.blrange=[]
filter2.corrtype=
filter2.nchan=0
filter2.startchan=0
filter2.type=filter
filter2.remove=true

filter1.baseline="!ST001*&&*"
filter1.blrange=[]
filter1.corrtype=
filter1.nchan=0
filter1.startchan=0
filter1.type=filter
filter1.remove=true


stationadder.autocorr=F
stationadder.average=true
stationadder.minpoints=1
```

```
stationadder.stations={ST001:"CS00[2-7]*"}
stationadder.sumauto=T
stationadder.type=stationadder
stationadder.useweights=True
```

Listing C.4: Parameter file to form bands of about 3 MHz.

```
msin.baseline="*"
msin.blrange=[]
msin.corrtype=
msin.datacolumn=DATA
msin.forceautoweight=FALSE
msin.missingdata=TRUE
msin.nchan=nchan
msin.orderms=FALSE
msin.sort=FALSE
msin.startchan=nchan/32
msin.useflag=TRUE
msout.overwrite=F
msout.tilenchan=0
msout.tilesize=1024
msout.vdsdir=A
msout.writefullresflag=T

steps=[]
```

Python scripts

Listing C.5: Correcting procedure for international and remote stations.

```
#!/usr/bin/python
import pyfits
import os
import numpy as np
import time
import sys

arglist= sys.argv
path=arglist[1]
intmin=int(arglist[2])
intmax=int(arglist[3])+1
nointmin=int(arglist[4])
nointmax=int(arglist[5])+1
refant=int(arglist[6])
newpath=arglist[7]
name = arglist[8]

```

```
def mongo_formel(arr1,arr2):
  arr3=[]
  for i in arr1:
    for j in arr2:
      arr3.append(i*256+j)
  return arr3

#path_data='list.txt'
#list_data=list(open(path_data,"r"))
#n_data=len(list_data)

t1 = time.time()

#path=list_data[z]
#path=path.rstrip()
ref_ant=[refant]
int_ant=range(intmin,intmax)
rs_ant=range(nointmin,nointmax)

hdufits=pyfits.open(path)
tabl=hdufits[0].data
head=hdufits[0].header
basel_2=mongo_formel(int_ant,int_ant)
basel_1=mongo_formel(rs_ant,int_ant)+mongo_formel(int_ant,ref_ant)
test1_array=[]
test2_array=[]
test3_array=[]
test4_array=[]
test5_array=[]
test6_array=[]
for i in range(len(tabl)):

  if tabl[i][5] not in basel_1 and tabl[i][5] not in basel_2:
    test1_array.append(np.median(np.abs(tabl[i][9][0][0][0][:,:,0])))
    test2_array.append(np.median(np.abs(tabl[i][9][0][0][0][:,:,1])))
  elif tabl[i][5] in basel_1:
    test3_array.append(np.median(np.abs(tabl[i][9][0][0][0][:,:,0])))
    test4_array.append(np.median(np.abs(tabl[i][9][0][0][0][:,:,1])))
  else:
    test5_array.append(np.median(np.abs(tabl[i][9][0][0][0][:,:,0])))
    test6_array.append(np.median(np.abs(tabl[i][9][0][0][0][:,:,1])))




print name,":"
print "________________________________________________"


median1_cor=np.median(test1_array)
```

```
median2_cor=np.median(test2_array)
print median1_cor,median2_cor
median_tru=np.median([median1_cor,median2_cor])

median1=np.median(test3_array)
median2=np.median(test4_array)
print median1,median2
median_fls=np.median([median1,median2]) *1.

median1=np.median(test5_array)
median2=np.median(test6_array)
print median1,median2
median_fls_2=np.median([median1,median2]) * 1.

print "_______________________________________________"

factor = median_tru/median_fls


for i in range(len(tabl)):
  if tabl[i][5] in basel_2:
    datacube=tabl[i][9][0][0][0]
    for j in range(len(datacube)):
      for k in range(len(datacube[j])):
        tabl[i][9][0][0][0][j][k][0]=tabl[i][9][0][0][0][j][k][0] * factor
        tabl[i][9][0][0][0][j][k][1]=tabl[i][9][0][0][0][j][k][1] * factor
  if tabl[i][5] in basel_1:
    datacube=tabl[i][9][0][0][0]
    for j in range(len(datacube)):
      for k in range(len(datacube[j])):
        tabl[i][9][0][0][0][j][k][0]=tabl[i][9][0][0][0][j][k][0] * factor
        tabl[i][9][0][0][0][j][k][1]=tabl[i][9][0][0][0][j][k][1] * factor

new_path=newpath + name
if os.path.exists(new_path):
  os.remove(new_path)
hdufits.writeto(new_path)
print '%s has been successfully modified and saved!' % (new_path)

t2=time.time()
ts_t = int(t2 - t1)
th = int(ts_t / 3600)
tm = int((ts_t - th * 3600) / 60)
ts = int(ts_t % 60)

print "The code has finished after %s h %s min %s s" % (th, tm, ts)
```

Listing C.6: ParselTongue procdure to perform phase calibration in AIPS and export MS files to FITS file format.

```
import os, sys
from AIPS import AIPS
from AIPSTask import AIPSTask as task
from AIPSData import AIPSUVData as UV
from Wizardry.AIPSData import AIPSUVData as WUV
from AIPSData import AIPSImage as IM
import time
import numpy as np
import matplotlib.pyplot as plt

# Enable these three lines and set dotv=1 in tasks if TV wanted to
    inspect things like cleaning.
#from AIPSTV import AIPSTV # Needed for TV
#tv = AIPSTV()
#tv.start()
nos=[1500,1501,1502,1503,1504,1505,1506,1507,1508,1509,1510,1511,
  1512,1513,1514]
bands=['BAND0','BAND1','BAND2','BAND3','BAND4','BAND5','BAND6',
  'BAND7','BAND8','BAND9','BAND10','BAND11','BAND12','BAND13','BAND14']




for i in range(len(nos)):
  whattodo = {'load_data': True,
         'index_data_1': True,
         'load_model': True,
         'index_data_m': True,
         'scale_data': False,
         'multi': False,
         'delete_tempfiles': False,
         'index_data_2': False,
         'clcor': False,
         'fixwt': True,
         'flag_bad':True,
         'fringe_INT':True,
         'fringe_RS':True,
         'export_afterAIPS': True,
         }

  ########## Initialize observation data ##########
  ALPHA = 0.0 # Spectral index
  AIPS.userno = nos[i]
  BAND = bands[i]
  clint = 0.5 # minutes
  remote_ants=range(1,48)
  int_ants=range(48,57)
  refant=57
```

```
    core_ant=[refant]
    NAME = '0836'
    MNAME= 'Model'

    PATHDATA = 'ADATA:0836+710-'+BAND+'.FITS'
    MPATHDATA= 'ADATA:band1.uvf'
    CLASS = 'UVDATA'
    PRECLASS = '1IF'
    WTCLASS = 'WTMOD'
    WTCLASS2 = 'WTMOD2'
    AMPCLASS = 'AMPSC'
    UVDECCLASS = 'UVDEC'
    UVAVG_class = 'UVAVG'
    AVSPC_class = 'AVSPC'
    FIXWT_class = 'FIXWT'
    MCLASS = 'MCL'
    CALIM = NAME + 'C'
    DISK = 2
    sorted_class = 'MSORT'
    logfile = 'log_'+NAME+'.log'
    target = 'BEAM_0'
    ##########^^^ END OF CONFIG VARIABLES ^^^##################
    tic = time.time()
    ########## Initialize Log file ##########
    try:
      os.system('mv ' + logfile + ' ' + logfile + '.old')
    except:
      pass
    AIPS.log = open(logfile, 'a')
    AIPS.log.write('whattodo = '+repr(whattodo)+'\n')

    ########## LOAD DATA ##########
    if whattodo['load_data']:
      fitld = task('fitld')
      fitld.datain = PATHDATA
      outdata = UV(NAME,CLASS, DISK, 1)
      fitld.outdata = outdata
      fitld.ncount = 1
      fitld.clint = clint
      if outdata.exists():
        print 'WARNING: Removing existing file '+outdata.name +'.' +
      outdata.klass
        outdata.zap()
        print '          File removed. Proceeding with FITLD...'
      fitld.go()

    if whattodo['index_data_1']:
      cloutver =1
      data = UV(NAME, CLASS, DISK, 1)
      # Remove all CL tables higher than version cloutver-1.
```

```
    for i in range(data.table_highver('CL'), cloutver-1, -1):
      data.zap_table('CL', i)
    data = UV(NAME, CLASS, DISK, 1)
    indxr = task('indxr')
    indxr.indata = data
    indxr.cparm[3]=clint
    indxr.go()


  if whattodo['load_model']:
    fitld = task('fitld')
    fitld.datain = MPATHDATA
    outdata = UV(MNAME,CLASS, DISK, 1)
    fitld.outdata = outdata
    fitld.ncount = 1
    fitld.clint = clint
    if outdata.exists():
      print 'WARNING: Removing existing file '+outdata.name +'.' +
   outdata.klass
      outdata.zap()
      print '         File removed. Proceeding with FITLD...'
    fitld.go()



  if whattodo['index_data_m']:
    cloutver =1
    data = UV(MNAME, CLASS, DISK, 1)
    # Remove all CL tables higher than version cloutver-1.
    for i in range(data.table_highver('CL'), cloutver-1, -1):
      data.zap_table('CL', i)
    data = UV(MNAME, CLASS, DISK, 1)
    indxr = task('indxr')
    indxr.indata = data
    indxr.cparm[3]=clint
    indxr.go()





  if whattodo['scale_data']:
    data = UV(NAME, CLASS, DISK, 1)
    outdata = UV(NAME, WTCLASS, DISK, 1)
    wtmod = task('wtmod')
    wtmod.indata = data
    wtmod.outdata = outdata
    wtmod.aparm[1] = 1e6 # Scaling to about 1.
    if outdata.exists():
```

```
        print 'WARNING: Removing existing file '+outdata.name +'.' + outdata.klass
        outdata.zap()
        print '           File removed. Proceeding with WTMOD...'
    wtmod.go()

    indxr = task('indxr')
    indxr.indata = outdata
    indxr.cparm[3]=clint
    indxr.go()

    data = UV(NAME, WTCLASS, DISK, 1)
    outdata = UV(NAME, AMPCLASS, DISK, 1)
    uvmod = task('uvmod')
    uvmod.indata = data
    uvmod.outdata = outdata
    uvmod.factor = 1e-6 # Scaling to about 1.
    uvmod.sour = [None, target]
    uvmod.flagver = 1
    if outdata.exists():
        print 'WARNING: Removing existing file '+outdata.name +'.' + outdata.klass
        outdata.zap()
        print '           File removed. Proceeding with UVMOD...'
    uvmod.go()


if whattodo['multi']:

    data = UV(NAME, AMPCLASS, DISK, 1)
    # We can use uvdec to decimate channels if we want, to get even numbers which can be split into more IFs in AIPS.
    #outdata = UV(NAME, UVDECCLASS, DISK, 1)
    #uvdec = task('uvdec')
    #uvdec.indata = data
    #uvdec.outdata = outdata
    #uvdec.bchan = 9
    #uvdec.echan = 968
    #uvdec.chinc = 1
    #uvdec.go()

    multi = task('multi')
    multi.indata =data
    #outdata = UV(NAME, MCLASS, 1, 1)
    outdata = UV(NAME, sorted_class, DISK, 1)
    multi.outdata = outdata
    if outdata.exists():
        print 'WARNING: Removing existing file '+outdata.name +'.' + outdata.klass
        outdata.zap()
```

```
      print '           File removed. Proceeding with UVMOD...'
    multi.go()

  if whattodo['delete_tempfiles']:
    print 'DELETING TEMPFILES'
    data = UV(NAME, CLASS, DISK, 1)
    if data.exists():
      data.zap()

    data = UV(NAME, PRECLASS, DISK, 1)
    if data.exists():
      data.zap()

    data = UV(NAME, WTCLASS, DISK, 1)
    if data.exists():
      data.zap()

    data = UV(NAME, AMPCLASS, DISK, 1)
    if data.exists():
      data.zap()

    data = UV(NAME,UVDECCLASS, DISK, 1)
    if data.exists():
      data.zap()

    data = UV(NAME, MCLASS, DISK, 1)
    if data.exists():
      data.zap()


########## INDEX DATA ##########
  if whattodo['index_data_2']:
    cloutver =1
    data = UV(NAME, sorted_class, DISK, 1)
    # Remove all CL tables higher than version cloutver-1.
    for i in range(data.table_highver('CL'), cloutver-1, -1):
      data.zap_table('CL', i)
    data = UV(NAME, sorted_class, DISK, 1)
    indxr = task('indxr')
    indxr.indata = data
    indxr.cparm[3]=clint
    indxr.go()

  if whattodo['clcor']:
    clcor = task('clcor')
    clcor.default()
    clcor.indata = UV(NAME, sorted_class, DISK, 1)
    clcor.antennas = [None, ] + int_ants
    clcor.opcode = 'GAIN'
    clcor.clcorprm[1] = 0.00005
```

```
    clcor.clcorprm[2] = 0
    clcor.gainuse= 2
    clcor.gainver= 1
    clcor.go()

  if whattodo['fixwt']:
    fixwt = task('fixwt')
    data = UV(NAME, CLASS, DISK, 1)
    #fixwt.indata = UV(NAME, sorted_class, DISK, 1)
    fixwt.indata=data
    fixoutdata = UV(NAME, FIXWT_class, DISK, 1)
    fixwt.outdata = fixoutdata
    if fixoutdata.exists():
      print 'WARNING: Removing existing file '+fixoutdata.name+'.' +
    fixoutdata.klass
      fixoutdata.zap()
      print '          File removed. Proceeding with FIXWT...'
    fixwt.solint = 1 #
    fixwt.go()
    indxr = task('indxr')
    indxr.indata = fixoutdata
    indxr.cparm[3]=clint
    indxr.go()

  if whattodo['flag_bad']:
    data = UV(NAME, FIXWT_class, DISK, 1)
    infgver = 0
    outfgver = 1
    # Remove all FG tables higher than infgver.
    for i in range(data.table_highver('FG'), infgver, -1):
     data.zap_table('FG', i)
    data = UV(NAME, FIXWT_class, DISK, 1)
    #Flag bad antenna
    uvflg = task('uvflg')
    uvflg.default()
    uvflg.indata = data
    uvflg.outfgver = outfgver
    uvflg.opcode = 'flag'
    uvflg.antenna = [None, ]
    #uvflg.timeran = [None, 0, 6, 8, 0, 0, 7, 30, 0]
    uvflg.go()

 ###### FRING FINDING ##########
  if whattodo['fringe_INT']:
    data = UV(NAME, FIXWT_class, DISK, 1)
    clinver = 1
    cloutver = 2
    snoutver = 1
    fgver = 1
    # Remove all SN tables higher than version snoutver-1.
```

```
    for i in range(data.table_highver('SN'), snoutver-1, -1):
      data.zap_table('SN', i)
    data = UV(NAME, FIXWT_class, DISK, 1)
    fring=task('fring')
    fring.indata = data
    fring.docalib = 1
    fring.gainuse = clinver
    fring.calsour = [None, target]
    fring.refant = refant
    fring.snver = snoutver
    fring.flagver = fgver
    fring.solint = 2
    fring.antennas = [None, 0]
    fring.cmod = 'COMP'
    mdata = UV(MNAME, CLASS, DISK, 1)
    fring.in2data = mdata
    # Setting dparms
    fring.dparm[2] = 5000 # ns delay window
    fring.dparm[3] = 90 # mHz, for speed
    fring.uvrange = [None, 60, 0]
    #fring.aparm[5]=1 # combine all IFs
    fring.antenna = [None, ] + int_ants + core_ant # only INT and core, with large delay win.
    #fring.timeran = [None, 0, 22, 0, 0, 0, 22, 30, 0]
    # NOTE: RR,LL should NOT be averaged since we are
    # correcting for the ionosphere. Once FRING is done,
    # we may average, form stokes I etc.
    fring.go()

    # CLIP solutions
    sninver = 1
    snoutver = 2
    data = UV(NAME, FIXWT_class, DISK, 1)
    # Remove all SN tables higher than version snoutver-1.
    for i in range(data.table_highver('SN'), snoutver-1, -1):
      data.zap_table('SN', i)
    data = UV(NAME, FIXWT_class, DISK, 1)
    snsmo = task('snsmo')
    snsmo.default()
    snsmo.indata = data
    snsmo.samptype = 'MWF'
    # ONLY CLIP, DO NOT SMOOTH
    # smoothing times
    snsmo.cparm[2] =  0 #phase
    snsmo.cparm[3] =  0.3 # rates
    snsmo.cparm[4] =  1.0# singleband delay
    snsmo.cparm[5] =  1.0 # multiband delay
    # Clip thresholds
    snsmo.cparm[7] =  360 # maxphas
    snsmo.cparm[8] =  10# max rates
```

```
    snsmo.cparm[9] =  100 # max single delay
    snsmo.cparm[10] =  100 # max multi delay
    snsmo.inver = sninver
    snsmo.outver = snoutver
    snsmo.smotype = 'VLBI' #
    snsmo.refant = refant
    snsmo.doblank = -1
    snsmo.go()
    # Apply SN-table
    data = UV(NAME, FIXWT_class, DISK, 1)
    # Remove all CL tables higher than version cloutver-1.
    for i in range(data.table_highver('CL'), cloutver-1, -1):
      data.zap_table('CL', i)
    data = UV(NAME, FIXWT_class, DISK, 1)
    # Make CL table
    clcal = task('clcal')
    clcal.default()
    clcal.indata = data
    clcal.snver = snoutver
    clcal.invers = snoutver
    clcal.calsour = [None, target] # Use sols from Ampcal
    clcal.sour = [None, ''] # Apply to all sources
    clcal.gainver = clinver
    clcal.gainuse = cloutver
    clcal.refant = refant
    clcal.go()

  if whattodo['fringe_RS']:
    data = UV(NAME, FIXWT_class, DISK, 1)
    clinver = 2
    cloutver = 3
    snoutver = 3
    fgver = 1
    # Remove all SN tables higher than version snoutver-1.
    for i in range(data.table_highver('SN'), snoutver-1, -1):
      data.zap_table('SN', i)
    data = UV(NAME, FIXWT_class, DISK, 1)
    fring=task('fring')
    fring.indata = data
    fring.docalib = 1
    fring.gainuse = clinver
    fring.calsour = [None, target]
    fring.refant = refant
    fring.snver = snoutver
    fring.flagver = fgver
    fring.solint = 2
    fring.antennas = [None, 0]
    # Setting dparms
    fring.dparm[2] = 3000 # ns delay window
    fring.dparm[3] = 60 # mHz, for speed
```

```
    fring.uvrange = [None, 20, 0]
    fring.cmod = 'COMP'
    fring.in2name = 'AD:b.mod'
    #fring.aparm[5]=1 # combine all IFs
    fring.dofit = [None,] + remote_ants
    #fring.timeran = [None, 0, 22, 0, 0, 0, 22, 30, 0]
    # NOTE: RR,LL should NOT be averaged since we are
    # correcting for the ionosphere. Once FRING is done,
    # we may average, form stokes I etc.
    fring.go()

    # CLIP solutions
    sninver = 3
    snoutver = 4
    data = UV(NAME, FIXWT_class, DISK, 1)
    # Remove all SN tables higher than version snoutver-1.
    for i in range(data.table_highver('SN'), snoutver-1, -1):
      data.zap_table('SN', i)
    data = UV(NAME, FIXWT_class, DISK, 1)
    snsmo = task('snsmo')
    snsmo.default()
    snsmo.indata = data
    snsmo.samptype = 'MWF'
    # ONLY CLIP, DO NOT SMOOTH
    # smoothing times
    snsmo.cparm[2] = 0 #phase
    snsmo.cparm[3] = 0.3 # rates
    snsmo.cparm[4] = 1.0# singleband delay
    snsmo.cparm[5] = 1.0 # multiband delay
    # Clip thresholds
    snsmo.cparm[7] = 360 # maxphas
    snsmo.cparm[8] = 40# max rates
    snsmo.cparm[9] = 2500 # max single delay
    snsmo.cparm[10] = 2500 # max multi delay
    snsmo.inver = sninver
    snsmo.outver = snoutver
    snsmo.smotype = 'VLBI' #
    snsmo.refant = refant
    snsmo.doblank = -1
    snsmo.go()
    # Apply SN-table
    data = UV(NAME, FIXWT_class, DISK, 1)
    # Remove all CL tables higher than version cloutver-1.
    for i in range(data.table_highver('CL'), cloutver-1, -1):
      data.zap_table('CL', i)
    data = UV(NAME, FIXWT_class, DISK, 1)
    # Make CL table
    clcal = task('clcal')
    clcal.default()
    clcal.indata = data
```

```
    clcal.snver = snoutver
    clcal.invers = snoutver
    clcal.calsour = [None, target] # Use sols from Ampcal
    clcal.sour = [None, ''] # Apply to all sources
    clcal.gainver = clinver
    clcal.gainuse = cloutver
    clcal.refant = refant
    clcal.go()

#### Export Fringe-Found-Data #####
if whattodo['export_afterAIPS']:
    clinver = cloutver
    data = UV(NAME, FIXWT_class, DISK, 1)
    split = task('split')
    split.default()
    split.indata = data
    split.source = [None, target]
    split.outclass = NAME
    split.docal = 1
    split.gainuse = clinver
    split.outdisk = DISK
    split.outseq = 1
    split.flagver = 0
    split.aparm[1] = 2
    outdata = UV(target, split.outclass, DISK, 1)
    if outdata.exists():
      print 'WARNING: Removing existing file '+outdata.name +'.' + outdata.klass
      outdata.zap()
      print '          File removed. Proceeding with SPLIT...'
    split.go()

    fittp = task('fittp')
    fittp.default()
    fittp.indata = outdata
    outname = NAME +'-'+BAND+ '_POSTAIPS.UVFITS'
    fittp.dataout = 'PWD:' + outname
    if os.path.exists(outname):
       os.remove(outname)
    fittp.go()
```

Bibliography

Acero, F., Ackermann, M., Ajello, M., et al. 2015, The Astrophysical Journal Supplement Series, 218, 23

Ade, P., Aghanim, N., Arnaud, M., et al. 2016, Astronomy & Astrophysics, 594, A13

Akyuz, A., Thompson, D., Donato, D., et al. 2012, arXiv preprint arXiv:1205.2238

Akyuz, A., Thompson, D., Donato, D., et al. 2013, Astronomy & Astrophysics, 556, A71

Antonucci, R. 1993, ARA&A, 31, 473

Antonucci, R. & Barvainis, R. 1990, The Astrophysical Journal, 363, L17

ASTRON. 2017, COBALT: correlator and beamforming application platform for the lofar telescope

Bass, M., Van Stryland, E. W., Williams, D. R., & Wolfe, W. L. 2001, Handbook of optics, Vol. 2 (McGraw-Hill New York)

Begeman, K., Belikov, A., Boxhoorn, D., et al. 2011, Future Generation Computer Systems, 27, 319

Blandford, R. D. & Payne, D. G. 1982, 199, 883

Blandford, R. D. & Znajek, R. L. 1977, 179, 433

Brentjens, M. 2016, 4th LOFAR data processing school

Burd, P. R. 2017, Master's thesis, Julius Maximilians University Wuerzburg, Germany

Burke, B. F. & Graham-Smith, F. 2010, An Introduction to Radio Astronomy (Cambridge University Press)

Cara, M. & Lister, M. L. 2008, ApJ, 674, 111

Caswell, J. L. & Crowther, J. H. 1969, MNRAS, 145, 181

Chang, C.-S. 2010

Chen, H. & Gentile, R. 2016, Commercial off-the-shelf journal

Condon, J. J. 1988, in Galactic and Extragalactic Radio Astronomy (Springer), 641–678

Cooper, N. J., Lister, M. L., & Kochanczyk, M. D. 2007, ApJS, 171, 376

Cornwell, T. & Perley, R. 1992, Astronomy and Astrophysics, 261, 353

Fanaroff, B. L. & Riley, J. M. 1974, MNRAS, 167, 31P

Greisen, E. W. 2003, Information Handling in Astronomy - Historical Vistas, 285, 109

Högbom, J. A. 1974, A&AS, 15, 417

Intema, H. 2007, in From Planets to Dark Energy: the Modern Radio Universe, 101

Intema, H., Jagannathan, P., Mooley, K., & Frail, D. 2016, Astronomy & Astrophysics

Intema, H. T., van der Tol, S., Cotton, W. D., et al. 2009, A&A, 501, 1185

Jackson, J. D. 1975, Electrodynamics (Wiley Online Library)

Jaeger, S. 2008, in Astronomical Data Analysis Software and Systems XVII, Vol. 394, 623

Jeyakumar, S. & Saikia, D. 2000, Monthly Notices of the Royal Astronomical Society, 311, 397

Kadler, M., Krauß, F., Mannheim, K., et al. 2016, Nat Phys, advance online publication, article

Kameno, S., Inoue, M., Wajima, K., Sawada-Satoh, S., & Shen, Z.-Q. 2003, PASA, 20, 213

Kappes, A. 2013, Amplitude Self-Calibration Corrections in TANAMI VLBI Experiments

Kellermann, K. I. & Pauliny-Toth, I. I. K. 1969, ApJ, 155, L71

Kellermann, K. I. & Thompson, A. R. 1985, Science, 229, 123

Kharb, P., Lister, M. L., & Cooper, N. J. 2010, ApJ, 710, 764

Krolik, J. H. 1999, Active galactic nuclei : from the central black hole to the galactic environment (Princeton University Press)

Kronberg, P. P. 1970, Journal of the Royal Astronomical Society of Canada, 64, 105

Kuehr, H., Pauliny-Toth, I. I. K., Witzel, A., & Schmidt, J. 1981, AJ, 86, 854

Lara, L., Cotton, W. D., Feretti, L., et al. 2001, A&A, 370, 409

Lara, L., Cotton, W. D., Feretti, L., et al. 1997, ApJ, 474, 179

Lister, M. L., Aller, M., Aller, H., et al. 2011, ApJ, 742, 27

Lister, M. L., Aller, M. F., Aller, H. D., et al. 2013, AJ, 146, 120

Lister, M. L., Cohen, M. H., Homan, D. C., et al. 2009, AJ, 138, 1874

Lister, M. L. & Homan, D. C. 2005, AJ, 130, 1389

Lobanov, A. P. 1998, A&A, 330, 79

Massaro, F., Giroletti, M., Paggi, A., et al. 2013, ApJS, 208, 15

Morabito, L. K., Deller, A. T., Röttgering, H., et al. 2016a, Monthly Notices of the Royal Astronomical Society, 461, 2676

Morabito, L. K. et al. 2016b, PhD thesis

Müller, C., Kadler, M., Ojha, R., et al. 2011, A&A, 530, L11

O'Dell, C. 1978, in New Instrumentation for Space Astronomy, 19–24

Offringa, A. R., de Bruyn, A. G., Biehl, M., et al. 2010, Monthly Notices of the Royal Astronomical Society, 405, 155

Osterbrock, D. E. & Ferland, G. J. 2006, Astrophysics of gaseous nebulae and active galactic nuclei (University science books)

Otterbein, K., Krichbaum, T., Kraus, A., et al. 1998, arXiv preprint astro-ph/9802316

Parma, P., Fanti, C., Fanti, R., Morganti, R., & De Ruiter, H. 1987, Astronomy and Astrophysics, 181, 244

Perley, R. A., Dreher, J. W., & Cowan, J. J. 1984, ApJ, 285, L35

Perucho, M., Kovalev, Y. Y., Lobanov, A. P., Hardee, P. E., & Agudo, I. 2012a, The Astrophysical Journal, 749, 55

Perucho, M. & Martí, J. 2007, Monthly Notices of the Royal Astronomical Society, 382, 526

Perucho, M., Martí, J. M., & Hanasz, M. 2005, Astronomy & Astrophysics, 443, 863

Perucho, M., Marti-Vidal, I., Lobanov, A. P., & Hardee, P. E. 2012b, Astronomy & Astrophysics, 545, A65

Peterson, B. M., Ferrarese, L., Gilbert, K., et al. 2004, The Astrophysical Journal, 613, 682

Readhead, A. C. S. & Wilkinson, P. N. 1978, ApJ, 223, 25

Sambruna, R. M., Donato, D., Tavecchio, F., et al. 2007, ApJ, 670, 74

Schilizzi, R. 1980

Schneider, P. 2008, Einführung in die extragalaktische Astronomie und Kosmologie (Springer Berlin)

Shakura, N. I. & Sunyaev, R. A. 1973, A&A, 24, 337

Shepherd, M. C. 1997, in Astronomical Society of the Pacific Conference Series, Vol. 125, Astronomical Data Analysis Software and Systems VI, ed. G. Hunt & H. Payne, 77

Stickel, M. & Kuehr, H. 1993, A&AS, 100, 395

Taylor, G. B., Carilli, C. L., & Perley, R. A., eds. 1999, Astronomical Society of the Pacific Conference Series, Vol. 180, Synthesis Imaging in Radio Astronomy II

Team, G. F. S., Gehrels, N., & Michelson, P. 1999, Astroparticle Physics, 11, 277

Thomasson, P. 1986, Quarterly Journal of the Royal Astronomical Society, 27, 413

Thompson, A. R., Clark, B., Wade, C., & Napier, P. J. 1980, The Astrophysical Journal Supplement Series, 44, 151

Thompson, A. R., Moran, J. M., & Swenson, Jr., G. W. 2001, Interferometry and Synthesis in Radio Astronomy, 2nd Edition (New York : Wiley)

Urry, C. M. & Padovani, P. 1995, PASP, 107, 803

Van Der Tol, S., Jeffs, B. D., & van der Veen, A.-J. 2007, IEEE Transactions on Signal Processing, 55, 4497

van Diepen, G. 2015, Astronomy and Computing, 12, 174

van Haarlem, M. P., Wise, M. W., Gunst, A. W., et al. 2013, A&A, 556, A2

Vestergaard, M. & Peterson, B. M. 2006, The Astrophysical Journal, 641, 689

Wells, D. C., Greisen, E. W., & Harten, R. H. 1981, A&AS, 44, 363

List of Figures

2.1. VLA observations of the FR-I radio galaxy 3C31 (a) at 1.4 GHz and the FR-II radio galaxy CygnusA (b) at 6 GHz. While 3C31 shows the typical bright jet terminating into plumes, CygnusA powers the highly collimated jet by the bright core in the center terminating into bright hot spots. These are feeding the surrounding lobes. Image from Lara et al. (1997) and Perley et al. (1984) with image courtesy of NRAO/AUI. 4

2.2. Schematic summary of the unification model based on Urry & Padovani (1995). The SMBH in the center is surrounded by the accretion disc and the dust torus. On the left the radio loud AGN are illustrated, likewise on the right the radio quiet AGN are illustrated. Different angles for the line of sight result in their respective object class as indicated with the arrows. Credit: NASA/CXC/M.Weiss; edited by Jonas Trüstedt. 7

2.3. The broad band SED of *S5 0836+710*. Credit: Chang (2010). 9

2.4. *Fermi*/LAT γ-ray light curve of *S5 0836+710* in the energy range between 100 MeV to 300 GeV with a weekly binning between August 2008 and April 2017. Multiple outburst periods on the order of weeks to months can be seen. Credit: M. Kreter. 10

2.5. EVN+MERLIN image of *0836+710* at 1.6 GHz. The contours are at 0.12, 0.15, 0.25, 0.33, 0.65, 1.2, 2.5, 5, 10, 20, 40, 80, and 99% of the image peak intensity (2.48 Jy/beam). The convolving beam is shown at the bottom-left corner (from Perucho et al. 2012b). 11

2.6. Radio map of the VLBA and EVN of the jet in *S5 0836+710* at 1.6 GHz (top) in 1997 (a) and 2008 (b) and 5 GHz (bottom) in 1997 (c) and 2003 (d). Isocontours range from 2 mJy/beam to 1.45 Jy/beam in the 1.6 GHz images and from 1.5 mJy/beam to 1.08Jy/beam in the 5 GHz ones. The beam property is indicated by the cross in the bottom left of each image with major and minor axes as well as the position angle. The red diamonds indicate the position of the ridge line (from Perucho et al. 2012a). 12

3.1. Scheme of a dish-like radio telescope with a diameter of D observing a target, indicated with the star that emits a coherent monochromatic EM wave with the wavelength λ. The collected signal interferes constructively in the focal point of the telescope, where the antenna would be placed. 14
3.2. The experimental APERTIF receiver on a mount for testing (left image). It consists of an 11×11-matrix of Vivaldi antennas. On the right image an observational result of the WSRT equipped with the APERTIF unit is shown. With the use of beam forming a much wider FOV can be achieved in comparison to a conventional antenna. Credit: NRAO/ASTRON. . . 16
3.3. Exemplary simulated directional radio response pattern, also called beam from Chen & Gentile (2016). The beam shows the highest sensitivity in the pointing direction, while still significantly smaller side lobes are visible. 17
3.4. Concept of common coordinate systems: Two antennas are connected by a baseline $\vec{b}_\lambda$. Monochromatic EM wave emitted by a source (grey), from which the brightness distribution is described with respect to the $(l, m.n)$-system (red) at the left reference antenna and with a geometric delay τ_g at the right antenna. The baselines of the array are described in the (u, v, w)-system (blue). Credit: Burd (2017). 18
3.5. Full (u, v)-coverage of the observation of *S5 0836+710* performed with the ILT. The wide range of baselines that the ILT offers can be seen here significantly. 20
3.6. Image of the superterp. It is part of the core of LOFAR located near Exloo, Netherlands. It is build up of six stations (six LBA and twelve HBA fields) that can be seen in the image. Credit: ASTRON/LOFAR . 21
3.7. International stations consist of a 70 m wide LBA array with 96 elements, a 56.5 m wide HBA array consisting of 96 antenna tiles and a total of 96 digital Receiver Units. Credit: ASTRON/LOFAR. 22
3.8. This map of Europe shows the location of all stations of the ILT. The Irish station in Birr is not yet constructed. The three polish stations are operational, but were not at the time of observation for the data handled in this thesis. Credit: ASTRON/LOFAR. 23
3.9. An Image of a LBA unit. The tube is holding on top the receiver unit attached to the four dipoles aligned that way to realist linear polarization measurements. Credit: ASTRON/LOFAR. 24
3.10. On the left the uncovered box of the HBA unit is shown. The triangular metals are the dipoles, measuring therefore in linear polarization. On the right the black casings in which the HBA of LOFAR are housed are shown as tile field. Credit: ASTRON/LOFAR. 25

3.11. Core stations consist of 48 HBAs and 96 LBAs and a total of 48 digital Receiver Units. The HBAs are arranged in two 24-element fields with a diameter of 30.8 m each, straddling an 87 m diameter LBA field. Remote stations consist of 48 HBAs arranged in a single 41 m diameter field and 96 LBAs arranged in a single 87 m diameter field and a total of 48 digital Receiver Units. Credit: ASTRON/LOFAR. 26

3.12. The modeled beam pattern for the HBA stations (top images) and respectively a cut in east direction (bottom images) presented by Brentjens (2016). The applied beam modeling shows tighter beams for stations that are further out due to the increasing size of the antenna fields. . . 27

4.1. Flowchart of the elaborated calibration routine that can be handled as a pipeline up to the hybrid imaging. The first steps are run on a dedicated calibration server located at the University of Wuerzburg. These steps are enclosed with a gray box. The following steps can be performed on any computer. The steps are color coded, indicating what software package is used at this point. 31

5.1. Image observed by the core stations only. On the left the whole FOV is shown with a diameter of about 8°. On the right a zoomed-in field of the central part is shown with the observation target *S5 0836+710* in the phase center. For both images the beam size is (186×155) arcsec with a position angle of $-36.0°$ and the contour levels are chosen to be at -50, 50, 100, 200, 500, 1000, 2000 Jy/beam with a noise RMS of 0.555 mJy/beam. 36

5.2. Stacked LOFAR image over the full calibrated frequency range (126 - 160 MHz) where the average (a) or median (b) values are calculated per pixel position and displayed in color scale. Both images show very a similar morphology and intensity distribution. Consequential there is a high consistency amongst the individual images. The lowest contour level marks with a 3σ threshold. The contour levels are -0.031, 0.031, 0.061, 0.12, 0.24, 0.49, 0.98, 2.0, 3.9, 7.8 Jy/beam. The RMS is 0.0102 Jy/beam. The beam size is $0.459'' \times 0.308''$ with a position angle of $-39.1°$. 37

5.3. Difference map between the mean and median stack image in Figure 5.2. The contour levels are chosen to be as presented in Figure 5.2 to allow easy comparability. 37

5.4. VLA observation of *S5 0836+710* in A configuration at 4.86 GHz central observation frequency. The lowest contour level marks with a 3σ threshold. The contour levels are -0.52, 0.52, 1.0, 2.1, 4.2, 8.3, 17, 33, 66, 133 mJy/beam. The RMS is 0.173 mJy/beam. The beam size is $0.517'' \times 0.415''$ with a position angle of $-80.5°$. 38

5.5. EVN+MERLIN observation of *S5 0836+710* at 1.6 GHz central observtaion frequency. The lowest contour level marks with a 3σ threshold. The contour levels are -1.2, 1.2, 2.4, 4.9, 9.8, 20, 39, 78, 156, 313, 625, 1251, 2501 mJy/beam. The RMS is 0.407 mJy/beam. The beam size is $0.084'' \times 0.068''$ with a position angle of 57°. Credit: Perucho et al. (2012a) availible at cdsarc.u-strasbg.fr (130.79.128.5) or via http://cdsarc.u-strasbg.fr/viz-bin/qcat?J/A+A/545/A65 39

5.6. Measured flux values in eleven bands of about 3 MHz bandwidth for the sources total flux observed by only LOFAR HBA core stations (blue cross), the calibrated total flux observed by the LOFAR HBA international stations (red box) and the flux of the unresolved core component seen by the LOFAR HBA international stations (green plus). Three bands in total were not evaluated due to insufficient data quality. One at the top end and low end of the frequencies each and one in between. . 41

5.7. The total source flux measured by the LOFAR HBA international stations for each final frequency band with a bandwidth of about 3 MHz. The values are modeled with a linear fit function (blue line) assuming to describe it sufficiently in the frequency range of about 50 MHz. The error bars are derived by the statistical scattering with respect to the fit, allowing to estimate the respective minimum and maximum slope (blue dashed lines). The model function is given in Equation 5.2.1. 42

5.8. The unresolved core component flux measured by the LOFAR HBA international stations for each final frequency band with a bandwidth of about 3 MHz. The values are modeled with a linear fit function (blue line) assuming to describe it sufficiently in the frequency range of about 50 MHz. The functions slope is set to the value 0, making the a priori assumption that the core flux has a flat spectrum. The error bars are derived by the statistical scattering with respect to the fit, allowing to estimate the respective minimum and maximum fitted flux (blue dashed lines). The model function is given in Equation 5.2.2. 43

5.9. The total extended flux around the unresolved core without the component in the south west, measured by the LOFAR HBA international stations for each final frequency band with a bandwidth of about 3 MHz. The values are modeled with a linear fit function (blue line) assuming to describe it sufficiently in the frequency range of about 50 MHz. The error bars are derived by the statistical scattering with respect to the fit, allowing to estimate the respective minimum and maximum slope (blue dashed lines). The model function is given in Equation 5.2.3. 44

5.10. The total flux of the component in the south west measured by the LOFAR HBA international stations for each final frequency band with a bandwidth of about 3 MHz. The values are modeled with a linear fit function (blue line) assuming to describe it sufficiently in the frequency range of about 50 MHz. The error bars are derived by the statistical scattering with respect to the fit, allowing to estimate the respective minimum and maximum slope (blue dashed lines). The model function is given in Equation 5.2.4. 46

5.11. Total radio flux of *S5 0836+710* measured by multiple telescopes. The measurements did not take place simultaneously but are rather a collection of all published measurements performed on this source. The black boxes are measurements obtained through NED. The other marks are LOFAR HBA measurments with international stations of the unresolved core (blue plus), the total source flux (red cross) and with measurements with core stations of the total source flux (green asterisks) in eleven frequency bands. 48

5.12. Exemplary spectral map between the LOFAR HBA international stations' image with a mid frequency of 160 MHz and the VLA image with a mid frequency of 4.86 GHz. Pixel values below 3σ for LOFAR or VLA are shown white. The contour levels are added from the VLA image with -0.52, 0.52, 1.0, 2.1, 4.2, 8.3, 17, 33, 66, 133 mJy/beam. The beam size is $0.517'' \times 0.415''$ with a position angle of $-80.5°$. Find all spectral maps in the appendix B. 49

5.13. Spectral map between the LOFAR HBA international stations' images with mid frequency of 126 MHz and 160 MHz. Pixel values below 3σ for any of the image are shown white. The beam size is $0.493'' \times 0.343''$ with a position angle of $-38.6°$. 49

A.1. LOFAR HBA measurement of *S5 0836+710* with international stations with a bandwidth of about 3 MHz and a central frequency of 126 MHz (a) and 129 MHz. The lowest contour level marks with a 3σ threshold. The contour levels are -0.031, 0.031, 0.061, 0.12, 0.24, 0.49, 0.98, 2.0, 3.9, 7.8 Jy/beam. The RMS is 0.0102 Jy/beam. The beam size is $0.493'' \times 0.343''$ with a position angle of $-38.6°$ (a) and $0.485'' \times 0.337''$ with a position angle of $-41.6°$ (b). 60

A.2. LOFAR HBA measurement of *S5 0836+710* with international stations with a bandwidth of about 3 MHz and a central frequency of 132 MHz (a) and 135 MHz. The lowest contour level marks with a 3σ threshold. The contour levels are −0.031, 0.031, 0.061, 0.12, 0.24, 0.49, 0.98, 2.0, 3.9, 7.8 Jy/beam. The RMS is 0.0102 Jy/beam. The beam size is $0.459'' \times 0.321''$ with a position angle of $-38.7°$ (a) and $0.495'' \times 0.313''$ with a position angle of $-34.2°$ (b). 60
A.3. LOFAR HBA measurement of *S5 0836+710* with international stations with a bandwidth of about 3 MHz and a central frequency of 138 MHz (a) and 141 MHz. The lowest contour level marks with a 3σ threshold. The contour levels are −0.031, 0.031, 0.061, 0.12, 0.24, 0.49, 0.98, 2.0, 3.9, 7.8 Jy/beam. The RMS is 0.0102 Jy/beam. The beam size is $0.526'' \times 0.312''$ with a position angle of $-35.7°$ (a) and $0.494'' \times 0.298''$ with a position angle of $-39.0°$ (b). 61
A.4. LOFAR HBA measurement of *S5 0836+710* with international stations with a bandwidth of about 3 MHz and a central frequency of 144 MHz (a) and 151 MHz. The lowest contour level marks with a 3σ threshold. The contour levels are −0.031, 0.031, 0.061, 0.12, 0.24, 0.49, 0.98, 2.0, 3.9, 7.8 Jy/beam. The RMS is 0.0102 Jy/beam. The beam size is $0.468'' \times 0.287''$ with a position angle of $-40.3°$ (a) and $0.408'' \times 0.286''$ with a position angle of $-37.4°$ (b). 61
A.5. LOFAR HBA measurement of *S5 0836+710* with international stations with a bandwidth of about 3 MHz and a central frequency of 154 MHz (a) and 157 MHz. The lowest contour level marks with a 3σ threshold. The contour levels are −0.031, 0.031, 0.061, 0.12, 0.24, 0.49, 0.98, 2.0, 3.9, 7.8 Jy/beam. The RMS is 0.0102 Jy/beam. The beam size is $0.428'' \times 0.307''$ with a position angle of $-47.8°$ (a) and $0.414'' \times 0.308''$ with a position angle of $-38.2°$ (b). 62
A.6. LOFAR HBA measurement of *S5 0836+710* with international stations with a bandwidth of about 3 MHz and a central frequency of 160 MHz. The lowest contour level marks with a 3σ threshold. The contour levels are −0.031, 0.031, 0.061, 0.12, 0.24, 0.49, 0.98, 2.0, 3.9, 7.8 Jy/beam. The RMS is 0.0102 Jy/beam. The beam size is $0.381'' \times 0.278''$ with a position angle of $-38.2°$. 62

B.1. Spectral map between the LOFAR HBA international stations' image with a mid frequency of 126 MHz (a), 129 MHz (b) and the VLA image with a mid frequency of 4.86 GHz. Pixel values below 3σ for LOFAR or VLA are shown white. The contour levels are added from the VLA image with −0.52, 0.52, 1.0, 2.1, 4.2, 8.3, 17, 33, 66, 133 mJy/beam. The beam size is $0.517'' \times 0.415''$ with a position angle of $-80.5°$. 64

B.2. Spectral map between the LOFAR HBA international stations' image with a mid frequency of 132 MHz (a), 135 MHz (b) and the VLA image with a mid frequency of 4.86 GHz. Pixel values below 3σ for LOFAR or VLA are shown white. The contour levels are added from the VLA image with -0.52, 0.52, 1.0, 2.1, 4.2, 8.3, 17, 33, 66, 133 $^{\mathrm{mJy}}/_{\mathrm{beam}}$. The beam size is $0.517'' \times 0.415''$ with a position angle of $-80.5°$. 64
B.3. Spectral map between the LOFAR HBA international stations' image with a mid frequency of 138 MHz (a), 141 MHz (b) and the VLA image with a mid frequency of 4.86 GHz. Pixel values below 3σ for LOFAR or VLA are shown white. The contour levels are added from the VLA image with -0.52, 0.52, 1.0, 2.1, 4.2, 8.3, 17, 33, 66, 133 $^{\mathrm{mJy}}/_{\mathrm{beam}}$. The beam size is $0.517'' \times 0.415''$ with a position angle of $-80.5°$. 65
B.4. Spectral map between the LOFAR HBA international stations' image with a mid frequency of 144 MHz (a), 151 MHz (b) and the VLA image with a mid frequency of 4.86 GHz. Pixel values below 3σ for LOFAR or VLA are shown white. The contour levels are added from the VLA image with -0.52, 0.52, 1.0, 2.1, 4.2, 8.3, 17, 33, 66, 133 $^{\mathrm{mJy}}/_{\mathrm{beam}}$. The beam size is $0.517'' \times 0.415''$ with a position angle of $-80.5°$. 65
B.5. Spectral map between the LOFAR HBA international stations' image with a mid frequency of154 MHz (a), 157 MHz (b) and the VLA image with a mid frequency of 4.86 GHz. Pixel values below 3σ for LOFAR or VLA are shown white. The contour levels are added from the VLA image with -0.52, 0.52, 1.0, 2.1, 4.2, 8.3, 17, 33, 66, 133 $^{\mathrm{mJy}}/_{\mathrm{beam}}$. The beam size is $0.517'' \times 0.415''$ with a position angle of $-80.5°$. 66
B.6. Spectral map between the LOFAR HBA international stations' image with a mid frequency of 160 MHz and the VLA image with a mid frequency of 4.86 GHz. Pixel values below 3σ for LOFAR or VLA are shown white. The contour levels are added from the VLA image with -0.52, 0.52, 1.0, 2.1, 4.2, 8.3, 17, 33, 66, 133 $^{\mathrm{mJy}}/_{\mathrm{beam}}$. The beam size is $0.517'' \times 0.415''$ with a position angle of $-80.5°$. 66
B.7. Spectral map between the LOFAR HBA international stations' images with mid frequency of 126 MHz and 160 MHz. Pixel values below 3σ for any of the image are shown white. The beam size is $0.493'' \times 0.343''$ with a position angle of $-38.6°$. 66

List of Tables

2.1. AGN classes with classification properties; Credit: Matthias Kadler with minor modifications. 6

3.1. Short list of the worlds largest steerable and non-steerable dished radio radio telescopes. Respectively their highest observation frequency and their diameter are given with an resulting approximate resolution after Equation 3.1.1. 15

5.1. Calibrated images of *S5 0836+710* with their measured properties . . . 35
5.2. Beam parameters for final images of *S5 0836+710* observed by LOFAR,VLA and EVN+MERLIN. 40
5.3. Calculated Lorentz factors (a) and the resulting jet speeds in c (b) based on the maximal and most probable jet size from Lara et al. (2001) and the minimal and most probable inclination angle. 51

Acronyms

AGN **A**ctive **G**alactic **N**uclei

AIPS **A**stronomical **I**mage **P**rocessing **S**ystem; Greisen 2003

APERTIF **APER**ture **T**ile **I**n **F**ocus

ASTRON **ASTR**onomisch **O**nderzoek in **N**ederland

BL Lac **BL Lac**erta

BLR **B**road **L**ine **R**egion

BLRG **B**road **L**ine **R**adio **G**alaxies

CASA **C**ommon **A**stronomy **S**oftware **A**pplication; Jaeger 2008

COBALT **CO**rrelator and **B**eamforming **A**pplication platform for the **L**ofar **T**elescope; ASTRON 2017

DIFMAP Caltech **DIF**ference **MAP**ping; Shepherd 1997

ECAP **E**rlangen **C**entre for **A**stroparticle **P**hysics

EM **E**lectro **M**agnetic

EVN **E**uropean **V**LBI **N**etwork; Schilizzi 1980

FITS **F**lexible **I**mage **T**ransport **S**ystem; Wells et al. 1981

FOV **F**ield **O**f **V**iew

FSRQ **F**lat **S**pectrum **R**adio **Q**uasar

FT **F**ourier **T**ransformation

GPS **G**lobal **P**ositioning **S**ystem

HBA **H**igh **B**and **A**ntenna

IC **I**nverse **C**ompton

IGM **I**nter **G**alactic **M**edium

ILT **I**nternational **L**OFAR **T**elescope

IPAC **I**mage **P**ublic **A**ccess **C**atalogue

ISIS **I**nteractive **S**pectral **I**nterpretation **S**ystem

KH **K**elvin-**H**elmholtz

LBA **L**ow **B**and **A**ntenna

LOFAR **LO**w-**F**requency **AR**ray; van Haarlem et al. 2013

LTA **L**ong **T**erm **A**rchive

MERLIN **M**ulti-**E**lement **R**adio **L**inked **I**nterferometer **N**etwork; Thomasson 1986

MIT **M**assachusetts **I**nstitute of **T**echnology

MOJAVE **M**onitoring **O**f **J**ets in **A**ctive galactic nuclei with **V**LBA **E**xperiments; Lister & Homan 2005

MS **M**easurment **S**et

NASA **N**ational **A**eronautics and **S**pace **A**dministration

NDPPP **N**ew **D**efault **P**re-**P**rocessing **P**ipeline

NED NASA/IPAC **E**xtragalactic **D**atabase

NLR **N**arrow **L**ine **R**egion

NLRG **N**arrow **L**ine **R**adio **G**alaxies

NRAO National Radio Astronomy Observatory

PVC **P**oly**V**inyl**C**hlorid

QSO **Q**uasi **S**tellar **O**bject

RAID5 **R**edundant **A**rray of **I**ndependent **D**isks-Level 5

RAM **R**andom-**A**ccess **M**emory

RFI **R**adio **F**requency **I**nterference

RMS **R**oot **M**ean **S**quare

SED **S**pectral **E**nergy **D**istribution

SI **S**ystème **I**nternational

SMBH **S**uper **M**assive **B**lack **H**ole

SNR **S**ignal to **N**oise **R**atio

TANAMI **T**racking **A**ctive Galactic **N**uclei with **A**ustral **M**illiarcsecond **I**nterferometry

TaQL Table **Q**uery **L**anguage; van Diepen 2015

VLA Karl G. Jansky **V**ery **L**arge **A**rray; Thompson et al. 1980

VLBA **V**ery **L**ong **B**aseline **A**rray; Kellermann & Thompson 1985

VLBI **V**ery **L**ong **B**aseline **I**nterferometry; Readhead & Wilkinson 1978

WSRT **W**esterbork **S**ynthesis **R**adio**T**elescope; Kronberg (1970)

Danksagung

An dieser Stelle möchte ich meine Dankbarkeit an folgende Personen/-gruppen ausdrücken, die maßgeblich zum Gelingen dieser Masterarbeit beigetragen haben:

Zu Beginn möchte ich meinen herzlichen Dank an Prof. Dr. Matthias Kadler richten. Die Bereitstellung dieses Projektes, die damit Verbundene Betreuung und vielseitige Unterstützung haben nicht nur dazu beigetragen, dass diese Arbeit zu einem erfolgreichen Abschluss führte, sondern auch meinen wissenschaftlichen Horizont und meine Fähigkeiten erweiterte. Zahlreiche spannende Diskussionen, richtungsweisende Ratschläge oder die Vermittlung mit Personen und anderen Arbeitsgruppen, die auf ihren Fachgebieten immer gute Diskussionsbeiträge liefern konnten sind nur einige Punkte die hier zu nennen wären.
Ferner möchte ich mich auch mit einem besonderen Dank an Prof. Dr. Karl Mannheim für sein großes Interesse an meinem Projekt und der damit verbundenen Unterstützung, sei es in interessanten Diskussionen oder der Bereitstellung der nötigen Hardware für das Gelingen dieser Arbeit richten. Dies setzt einen soliden Grundstein für weitere spannende Studien mit dem LOFAR Teleskop an diesem Lehrstuhl, welches ohne sein Mitwirken nicht möglich wäre.
Ein weiterer besonderer Dank geht an Dr. Jonas Trüstedt, welcher mir den Einstieg in das Projekt durch seine gestellten Beobachtungsanträge und der Einführung in die LOFAR Datenreduktion ermöglicht hat und somit die ersten Bausteine dieses Projekts mit mir gelegt hat.
Des weiteren möchte ich mich bei Paul Burd und Jonas Ringholz bedanken, die mit mir meine Daten zum cross-check verarbeitet haben und in diesem Rahmen gute Beiträge und Ideen aufgebracht haben, die auch zum gelingen dieser Arbeit beigetragen haben.
Einen großen kollektiven Dank richte ich an den gesamten Lehrstuhl für Astronomie. Die herzliche Atmosphäre, welche ich seit beginn meiner Bachelorarbeit erfahre, empfinde ich als sehr besonders und überaus positiv. Dies wirkt sich nicht nur auf einen starken Zusammenhalt und eine hohe Produktivität aus, sondern es macht auch einfach nur Spaß in diesem Umfeld an einem Projekt zu arbeiten.
Abschließend möchte ich meinen Eltern Waldemar und Alwina, sowie meinen Brüdern Eugen und Andreas danken, welche mich entlang meines Lebens und insbesondere meines gesamten Studiums nach ihren eigenen Möglichkeiten unterstützt und bestärkt haben diesen Weg einzuschlagen und daran festzuhalten. Wissens mich immer auf ihre Hilfe verlassen zu können ermöglichte es mir, mich mit meiner ganzen Motivation des

Studiums der Physik zu widmen. Für diese entgegengebrachte Liebe und Hingabe kann nicht genug danken.
I want to thank the long-baseline LOFAR and ASTRON group which is too big to be named personally. They have an incredible high competence to work on such demanding data and are happily sharing their knowledge and experience with anyone struggling with such data (this happens really, really often!). Their professional but also kind and familiar communication and interaction is not only beneficial to work efficiently, but also creates a comfortable social environment.
Finally I want to thank Jin Koda who is assistant professor at Stony Brook University, where I spent one year abroad. I was able to work during that time and beyond on interesting optical data. This project he offered taught me a lot about optical astronomy and how to work with such data. The various discussions we had, often inspired me or helped me on a specific topic to find a solution.
This research has made use of data from the MOJAVE database that is maintained by the MOJAVE team (Lister et al. 2009).
This research has made use of **I**nteractive **S**pectral **I**nterpretation **S**ystem (ISIS) functions provided by **E**rlangen **C**entre for **A**stroparticle **P**hysics (ECAP)/Remeis observatory and **M**assachusetts **I**nstitute of **T**echnology (MIT) (htt://www.sternwarte.uni-erlangen.de/isis/).
This research has made use of the **N**ational **A**eronautics and **S**pace **A**dministration (NASA)/**I**mage **P**ublic **A**ccess **C**atalogue (IPAC) Extragalactic Database (NED) which is operated by the Jet Propulsion Laboratory, California Institute of Technology, under contract with the National Aeronautics and Space Administration.

Declaration of authorship

I, Alexander Kappes, declare that this thesis titled, 'Long-wavelength radio observation of S5 0836+710 with the Low-Frequency Array (LOFAR)' and the work presented in it are my own. I confirm that:

- This work was done wholly or mainly while in candidature for a research degree at this University.
- Where any part of this thesis has previously been submitted for a degree or any other qualification at this University or any other institution, this has been clearly stated.
- Where I have consulted the published work of others, this is always clearly attributed.
- Where I have quoted from the work of others, the source is always given. With the exception of such quotations, this thesis is entirely my own work.
- I have acknowledged all main sources of help.
- Where the thesis is based on work done by myself jointly with others, I have made clear exactly what was done by others and what I have contributed myself.

Signed: ______________________________________

Date: ______________________________________